THESIS

COMBUSTION AND FLAME PROPAGATION CHARACTERISTICS OF DECOMPOSED AMMONIA FUEL MIXTURES IN A RAPID COMPRESSION MACHINE

Submitted by

Jack H. Bicksler

Department of Mechanical Engineering

In partial fulfillment of the requirements

For the Degree of Master of Science

Colorado State University

Fort Collins, Colorado

Summer 2026

Master's Committee:

Advisor: Bret Windom
Co-Advisor: Azer Yalin

Seonah Kim

Copyright by Jack H. Bicksler 2026

All Rights Reserved

ABSTRACT

COMBUSTION AND FLAME PROPAGATION CHARACTERISTICS OF DECOMPOSED AMMONIA FUEL MIXTURES IN A RAPID COMPRESSION MACHINE

Rising fuel demands and the need to address climate change have created an increasing need for carbon-free energy sources. Ammonia (NH_3) presents a promising alternative fuel solution, as it is readily available, functions as a dense hydrogen carrier, and has an existing global production/-transportation network. However, neat ammonia exhibits unfavorable combustion characteristics, including slow flame speeds and long ignition delay times. The decomposition (or cracking) of ammonia, a process that breaks ammonia into its components, hydrogen (H_2) and nitrogen (N_2) is known to improve the combustion characteristics, enhancing laminar flame speed, turbulent flame speed, and its utilization in both experimental devices and engines.

In this study, the first of their kind combustion and flame propagation characteristics of decomposed ammonia fuel blends were measured using a laser-ignited dual-piston rapid compression machine at engine-relevant condition. Experimental measurements of decomposed ammonia (0%, 10%, 20%, and 42.5%, ϕ=1) flame speeds were conducted across a range of elevated pressure/temperature conditions (20–30 bar, 760–850 K). Stoichiometric methane (CH_4) was also investigated as a comparative baseline to the 42.5% decomposition case provided by preliminary flame speed calculations. Stoichiometric fuel blends were ignited using a 1064 nm Nd:YAG laser producing spherically expanding flames. Complementing these experiments, 1-D and 3-D simulations were performed to evaluate eight current chemical kinetic mechanism against the collected dataset. Measured flame speeds revealed significant discrepancies in chemical kinetic mechanisms. High-speed schlieren imaging revealed the presence of hydrogen-inducted cellular instabilities at higher decomposition percentages and pressures. 3-D computational-fluid-dynamics (CFD) simulations of the RCM revealed that current mechanisms and numerical models struggle to model combustion

phasing and transport. Furthermore, diesel-ammonia dual-fuel ignition delay times were measured presenting a balance needed between the diffusion of hydrogen and the available oxidizer.

These results highlight the need for the development of mechanisms and simulation approaches at elevated/engine-relevant conditions for decomposed ammonia blends. This work provides a crucial dataset and a foundation for further high temperature/pressure flame speed measurements, accelerating the development of energy conversion devices capable of leveraging reformed ammonia mixtures as a carbon-free fuel.

ACKNOWLEDGEMENTS

Dr. Bret Windom, thank you for the opportunity you have given me to study combustion. Your help and insight has helped me grow into a confident researcher and contributor to the combustion community. Without your help and guidance, I would not be not be where I am today.

Dr. Azer Yalin and Dr. Seonah Kim, thank you for serving on my committee, I hope to continue to work with you both in the future.

Dr. Miguel Valles Castro, your expertise and guidance throughout my senior research project was much needed and helpful. Thank you for answering my questions and teaching me how to use the rapid compression machine. Andrew Zdanowicz, Colin Slunecka, and Dr. Siddhesh Bhoite, thank you for always being willing to help me if I was stuck on the RCM or just had a genuine question, no question every felt too stupid. Thank you.

Sam Preuss and Alayna Gilbert, thanks for being my desk buddies and be willing to listen to me complain. Zach Kinzler, Cyrus Johnston, and Manav Sharma, thanks for your support.

Mom and Dad, thanks for always being there for me and being my voices of reason and always being there for me. Without you I would be in a pretty tough position, thank you for everything.

Finally, thanks for all the friends I have made here at CSU and in Fort Collins. Without everyone's help I would not have been able to make it where I am now.

DEDICATION

I would like to dedicate this work to my parents. Thank you for all of your hard work and constant support my entire life.

TABLE OF CONTENTS

ABSTRACT ii
ACKNOWLEDGEMENTS iv
DEDICATION v
LIST OF TABLES viii
LIST OF FIGURES ix

Chapter 1 INTRODUCTION 1
1.1 Background and Motivation 1
1.1.1 Ammonia Decomposition 3
1.1.2 Ammonia in Engines 4
1.2 Gaps in literature 7
1.2.1 Low temperature/pressure flames 9
1.2.2 High temperature/pressure flames 11
1.2.3 Shock Tube Flames 12
1.2.4 RCM Flame Studies 12
1.3 Objectives of this work 16

Chapter 2 EXPERIMENTAL SETUP 18
2.1 Rapid Compression Machine 18
2.1.1 Piston Offsets 22
2.2 Ammonia Safety and Sealing 23
2.3 Mixing Tank Procedure 26
2.4 Hardware and Imaging 27
2.4.1 Laser Hardware 27
2.4.2 Droplet Generator Hardware 31

Chapter 3 EXPERIMENTAL METHODS 34
3.1 Top-Dead-Center Conditions Calculations 34
3.2 Decomposition Mixture Calculations 35
3.3 Ammonia-Diesel Equivalence Ratio Calculation 36
3.4 Testing Matrix 38
3.4.1 Flame Speed Mixtures 38
3.4.2 Diesel Droplet Ignition Mixtures 40
3.5 Flame Speed Measurements 41
3.6 Diesel Droplet Ignition Measurements 44
3.7 Apparent Heat Release Rate (AHRR) 46
3.8 Effective Lewis Number 47
3.9 Laminar Flame Thickness 49

Chapter 4 NUMERICAL/COMPUTATIONAL METHODS 51
4.1 1-Dimensional Simulations 51

4.1.1 Mechanisms Used . . . 52
4.2 Ammonia-Diesel Diffusion and Ignition Modeling . . . 55
4.3 3-Dimensional CONVERGE Simulations . . . 56
4.3.1 Numerical Model . . . 56
4.3.2 Physical Model . . . 57
4.3.3 Grid Control . . . 59
4.3.4 Preliminary Simulations for Spark Timing and Energy . . . 61
4.3.5 Crevice Burning and Flame Quenching . . . 64

Chapter 5 EXPERIMENTAL RESULTS . . . 68
5.1 Flame Speed Results . . . 68
5.1.1 Decomposition Effects . . . 69
5.1.2 Piston Offset Effects . . . 75
5.1.3 42.5% Decomposition vs Methane . . . 77
5.1.4 Pressure Effect . . . 83
5.1.5 Perfect Flame Comparison . . . 85
5.2 Diesel Ignition Delay Times . . . 87
5.2.1 Ignition Delay Time Measurements . . . 87
5.2.2 Droplet Flame Morphology . . . 92

Chapter 6 COMPUTATIONAL RESULTS . . . 96
6.1 Offset Effect on Bulk-Flow . . . 96
6.2 Offset Effect on Thermodynamic Conditions . . . 101
6.3 Mechanism Effect . . . 102
6.3.1 CFD Pressure . . . 103
6.3.2 CFD AHRR . . . 105
6.4 Offset Effect . . . 107
6.5 CFD Flame Morphology and Measurement . . . 108

Chapter 7 CONCLUSIONS AND FUTURE WORK . . . 113
7.1 Flame Speed Conclusions . . . 113
7.2 Diesel Ignition Conclusions . . . 114
7.3 Future Work . . . 116
7.3.1 Fractal Analysis . . . 116
7.3.2 Turbulent Flame Speed Characterization . . . 117

Bibliography . . . 119

Appendix A RCM OVERHAUL . . . 131

LIST OF TABLES

1.1 Volumetric energy densities and combustion properties of various fuels compared to NH_3. Laminar flame speeds (S_L) are at 298 K, 1 atm; Ignition delay times (IDT) are generalized for high-pressure/temperature engine conditions. 3
1.2 Comparison of relevant, elevated thermodynamic ammonia/hydrogen flame speed studies in literature. 9

2.1 Accuracy of different experimental devices used in the RCM. 22
2.2 Acute Exposure Guideline Levels (AEGLs) for anhydrous ammonia (NH_3) in ppm. . . 25
2.3 Physical properties and molecular sizes of gases commonly utilized in RCM experiments. 25

3.1 John Deere PowerTech PWL 4.5L Engine and Fuel Specifications. 36
3.2 Experimental test matrix for flame speed measurements with each species mole fraction. A 75%/25% Ar/N_2 inert ratio was used for each case. 39
3.3 Experimental test matrix for NH_3/Diesel and H_2/Diesel showing species mole fractions (X_i). Decomposed ammonia cases have 100% Ar dilution and are at $\phi = 0.5$, H_2 mixtures are all at a 90/10 Ar/N_2 dilution at $\phi = 0.4, 0.5$. 40

4.1 Ammonia-based chemical kinetic mechanisms evaluated in this study. The C3 mechanisms are taken directly from CONVERGE CFD software and the WUT mechanism is specialized for ammonia/diesel mixtures. 54
4.2 Adaptive Mesh Refinement (AMR) and Fixed Embedding (FE) timing map for 3-D CFD simulations. Cell size is based on the scale and initial grid size of the simulation. SGC represents the sub-grid criterion. 59

5.1 Averaged experimental conditions and standard deviations for TDC temperatures and measured flame speeds. Effective lewis number (Le_{eff}) and flame thickness (δ_l) were computed via Cantera using the NUIG mechanism. The flame thickness was calculated using the Full Width Half Maximum (FWHM) of the NH_2 radical concentration profile. 69
5.2 Comparison of experimental S_L with numerical predictions. Values in parentheses represent the percent error from the experimental points. 72
5.3 Mean deviation of simulated flames from the averaged value of all mechanisms. Each value represents the average percentage error of each mechanism from the mean of all mechanisms at all temperature points. 73
5.4 Time dependent radius second polynomial curves as seen in Figure 5.7. Accelerations of the 25 bar, $\sim$840 K cases of each mixture were extracted from the flame radius (d^2R/dt^2) by applying a second-order polynomial fit to the radius vs time data ($R(t) = at^2 + bt + c$). 80

6.1 Comparison of experimental, 3-D CFD, and 1-D simulation flame speeds. 110

LIST OF FIGURES

1.1 Comparison of gravimetric and volumetric densities of multiple fuels. 2
1.2 Cartoon of spark-ignited (SI) engine compared to a diesel-piloted dual-fuel compression engine. 5
1.3 Cartoon of droplet evaporation and the subsequent flame propagation as a result. 6
1.4 Example of a constant volume combustion chamber (CVCC) from University of Massachusetts Lowell. 10
1.5 End-view images in the flame propagation stage of different ammonia/hydrogen fuel mixtures seen in the single-piston flame study from Zhang et al. 14
1.6 Traces of hot wire anemometer and combustion experiments done in a single-piston RCM from Nolte et al. at Aachen University. 16

2.1 Temperature-pressure graphs of operating conditions of different experimental devices and combustion engines. 20
2.2 Picture of the rapid compression machine. 21
2.3 O-ring chemical compatibility chart of possible o-rings. 24
2.4 Images of rupture disc installed on the mixing tanks replacing previously used pressure relief valves. 26
2.5 Experimental setup of the rapid compression machine where solid lines represent piping (-) and dashed lines wiring (- -). a) Shows the overall lab setup with RCM connections to the DAQ system and computer, b) shows the chamber cross-section, and c) shows the schlieren and laser setup. 29
2.6 BNC wiring diagram of flame speed experiments. 30
2.7 Traces from RCM experiments for the pressure, piston location, laser energy, AHRR and location of flame measurement. 31
2.8 Schematic of the droplet generator originally designed by Siddhesh Bhoite. a) represents the solid model, b) the exploded view, and c) photograph of droplet generator. . . 32
2.9 Cross-section of the RCM chamber with the attached droplet generator designed by Siddhesh Bhoite. 32
2.10 BNC wiring diagram of droplet ignition experiments. 33

3.1 Laminar flame speed simulations of a range of decomposed ammonia mixtures compared to methane using the NUIG and C3 mechanisms. 38
3.2 Visualization of edge detection and the measurement process associated with determining the flame radius. 41
3.3 Example of measured time-dependent radius of a spherically propagating flame using MATLAB edge detection. The green or 'Raw Prop' line represents the raw radius, these values are than filtered (black line), removing points that have a sudden change in slope. These values are than fitted to a second-order polynomial (red line). This example is for a 20% decomposition at 840 K and 25 bar. 42

3.4 Example of stretch rate plot where the green dots represent the raw stretch values between each point, the blue represents the linear fit, and black represents the non-linear Kelley extrapolation method. This example is for a 20% decomposition at 840 K and 25 bar, the same example shown in Figure 3.3. 43
3.5 Process taken into measuring the droplet ignition delay time where a) represents the start of the video, b) shows the injection of the droplets, c) shows where the droplet may be at top-dead-center (where measurement begins), d) shows where the droplet trajectory between TDC and ignition, e) presents the droplet ignition point (end of measurement), and finally f) shows the flame morphology. 45
3.6 Example of a common pressure trace seen in droplet experiments. The mixture is a 40% decomposition with diesel ignition. The dotted lines signify the ignition delay time associated when the droplet ignites in the mixture. 45
3.7 Example of the apparent heat release rate (AHRR) calculated using the measured pressure trace. 47
3.8 Example of the flame thickness of a 20%D flame at 800 K and 25 bar using the FWHM method and the NH_2 radical. 50

4.1 Example of nitrogen pathways for a 20%D mixture at 800 k and 25 bar. Computed in Cantera using the NUIG mechanism. 53
4.2 Model of the whole RCM where a) shows the entire geometry and b) shows the model compressed at top-dead-center. 58
4.3 Model of the RCM chamber including the window cavities, not modeled in previous studies. 59
4.4 Visualization of fixed embedding regions used to refine the flame front in CFD simulations. The times, scales, and sizes shown are used for the 0%, 10%, and 20% decomposition cases. The 42.5% decomposition and methane cases used the "medium flame" and "large flame" at scales of 5 and 4. 60
4.5 Original spark energy and size compared to the final used in the study. The original spark had a spherical radius of 5 E-05 m and energy of 30 mJ where the final has a 0.0625 m radius and energy of 5 mJ. a) presents the flame morphology for each case where the blue square represents the original spark and black is the final spark, b) presents the maximum temperature, and c) presents the apparent heat release rate. This example is for a 10% decomposition case at the highest temperature conditions. . 62
4.6 Spark sweeping. Group 1 represents a fixed time-scaling of 24-24.25 ms and sweep of energy values and sizes. Group 2 represents a set size of 0.0625 mm and a range of timings. These simulations were conducted using the 10% decomposition mixture at the highest temperature condition. 63
4.7 Geometry representation of the process used to simulate "quenched" flames in CFD simulations. This image represents the piston where the light blue boundary is the piston face, gray is the side of the piston, red is the piston crevice, blue is the piston-sleeve interaction, and pink is the flow-through interface between the reacting volume and the non-reaction volume. 65

4.8 Visual comparison of the original simulations allowing for flame propagation into the piston crevice volumes to the flame quenching model. A temperature clip is located in the middle of the chamber where the left set of images represent the original model and the right represents the new model. 66
4.9 Thermodynamic trace comparison of the original combustion model with the simulated flame-wall quenching model. Both the C3 and Han mechanisms are compared to an experimental trace, using the 20% decomposition case. a) represents the pressure effect and b) represents the heat release rate effect. 67

5.1 Decomposition percentage sweep for each temperature case at 25 bar. 70
5.2 Temperature sweep of flame speeds of decomposed ammonia mixtures for 0%D, 10%D, and 20%D mixtures at 25 bar. Lines indicate 1-D simulation results with varying mechanisms as shown in Chapter 4. 71
5.3 Flame morphology of decomposed ammonia mixtures. All flames shown have offsets < 0.3 ms, are at the highest temperature condition (840 K), and 25 bar. 74
5.4 Measured flame speeds as a function of corresponding piston offset. The red dashed line signifies the 6 ms cutoff. The yellow exponential trend line highlights the repeatability maintained for offsets <6 ms ad the subsequent increase in flame speed. All flames are at pressures of 25 bar. 76
5.5 Example of a turbulent-inducted flame from high offsets. This shows the flame morphology of a flame at 840 K, 25 bar at 20%D at a 8.12 ms offset. The corrected flame measures at 157.07 cm/s. 77
5.6 Comparison of 42.5%D against the baseline CH_4 mixture, both are at 25 bar and ϕ=1. Lines indicate 1-D simulation results with varying mechanisms as shown in Chapter 4. 79
5.7 Measured flame radius as a function of time for each mixture at ∼840 K and 25 bar. Second-order polynomial fits from the flame measurement MATLAB code were used to calculate acceleration constants. Curves here represent flames that have offsets less than 0.2 ms. 80
5.8 Sensitivity analysis for the Han, C3, NUIG, and Glarborg mechanisms at 25 bar and 850 K. 82
5.9 Comparison of the flame morphologies of the 42.5%D against the baseline CH_4 mixture both at 25 bar. 83
5.10 Pressure sweep of 10%D mixture all at ∼835 K. Lines indicate 1-D simulation results with varying mechanisms as shown in Chapter 4. 84
5.11 Pressure sweep of 10%D mixture all at ∼835 K. Lines indicate 1-D simulation results with varying mechanisms as shown in Chapter 4. 85
5.12 Flame propagation images of a "model" flame compared to a "normal" RCM flame containing instabilities and lobes from laser ignition. 86
5.13 Process taken into measuring the droplet ignition delay time where a) represents the start of the video, b) shows the injection of the droplets, c) shows where the droplet may be at top-dead-center (where measurement begins), d) shows where the droplet trajectory between TDC and ignition, e) presents the droplet ignition point (end of measurement), and finally f) shows the flame morphology. 88
5.14 Droplet size sweep of ignition delay time measurements of ammonia-diesel droplets for 0%, 20%, and 40% at 20 bar and 880 K. 89

5.15 Droplet size sweep of ignition delay time measurements comparing hydrogen to decomposed ammonia mixtures. 90
5.16 Modeled spatial profiles of diffusion of the premixed fuel mixture (decomposed ammonia at ϕ=0.5) into pure diesel $nC_{12}H_{26}$. This was modeled using a counter flow diffusion flame as explained in Section 4.2. 91
5.17 Normalization of the ignition delay time (IDT) and equivalence ratio about the 0% decomposition IDT from Figure 5.16. The black vertical lines represent the location at which the relevant IDT of each mixture at a 100 μm droplet ignites as seen in Figure 5.14. For each mixture, the relative IDT and equivalence ratio calculated are listed: (%D = 0%, 20%, 40% | IDT = 15, 20, 10 ms | ϕ=1.147, 0.706, 0.888). 92
5.18 Flame propagation images of a "model" flame compared to a "normal" RCM flame containing instabilities and lobes from laser ignition. 93
5.19 Droplet flame morphology images for 0%, 20%, and 40% decomposition, showing initial droplet ignition and subsequent flame propagation. 95

6.1 Example of post-processing where a velocity probe is inserted into the middle of chamber, measuring the velocity magnitude at that node. The velocity probe is represented by the white circle in the middle. 97
6.2 Plots of the variation of the velocity in the middle of the chamber. This is located directly in the middle of the chamber using a probe to measured the magnitude of the velocity at this point. The dotted lines represent the time frame at which the flame is measured experimentally. 98
6.3 Velocity field within the combustion chamber, monitoring TDC, spark time, and subsequent flame measurement window. Plots above the flow field represent the velocity trace located at the white probe in the middle of the chamber. 99
6.4 Flame morphology of each simulated offset at 0, 3, and 6 ms offsets fo 20% decomposition mixtures. 100
6.5 Temperature variation based on range of offsets using the 20% decomposition mixtures at $T_i = 60°$C. The temperature plotted is the maximum temperature seen in the chamber. The maximum at each point is where the simulation hits TDC. 102
6.6 CFD pressure traces against experimental traces for all mixtures at ~840 K and 25 bar, comparing the Han and C3 mechanisms. 104
6.7 CFD apparent heat release (AHRR) traces against experimental traces for all mixtures at ~840 K and 25 bar, comparing the Han and C3 mechanisms. 0 ms represents the time at TDC. 106
6.8 Offset pressure traces of CFD simulations compared to experimental traces using the C3 mechanism at 20%D and the highest temperature case. The dotted lines represent the location at which the flame is measured in experiments. 107
6.9 Flame morphologies of Han and C3 mechanisms compared to experimental case at 10% decomposition, 25 bar, and 840 K. 109
6.10 Comparison of commonly used 1-D solvers with different transport models. In these simulations Cantera uses the multicomponent model, CONVERGE uses mixture-averaged, and Chemkin uses multicomponent as well. 0%, 10%, 20%, and 42.5% decomposition were all simulated across all software. 111

7.1 Fractal analysis and the image processing associated with flame feature extraction using MATLAB used by Chen et al. 116
7.2 Example of a 42.5% decomposition turbulent flame in the RCM at 25 bar, 750 K using turbulent inserts. 117

CHAPTER 1 – INTRODUCTION

1.1 Background and Motivation

Rising fuel demands and the need to address climate change have created an increasing need for carbon-free energy sources. Under the recent Paris Agreement, in 2015, between nations in the United Nations, an agreement was met to preserve the planet by substantially reducing global greenhouse gas emissions. The long-term goal is to keep the global average surface temperature increase to be kept below 2°C, but limited to 1.5°C [1, 2]. This escalating energy demand and need to mitigate greenhouse gas emissions has driven a large amount of research into sustainable, zero-carbon alternative energies.

While hydrogen (H_2) is an ideal fuel from an emissions standpoint, its low volumetric energy density, storage challenges, lack of transport infrastructure, and basic combustion chemistry limit its adoption when compared to traditional hydrocarbon fuels. At a standard storage pressure of 700 bar (25 °C), the volumetric energy density of compressed H_2 is approximately 5.6 MJ/L. In contrast, uncompressed liquid hydrocarbons like diesel and gasoline exhibit significantly higher volumetric energy densities of 35.8 MJ/L and 32.4 MJ/L, respectively, at ambient conditions (25 °C, 1 atm). This volumetric energy density difference limits the logistical and onboard storage volume required to obtain comparable ranges using hydrogen.

Ammonia (NH_3) has emerged as a viable alternative to common hydrocarbons and a practical hydrogen carrier due to its high volumetric energy density, established manufacturing, and existing transportation. In comparison to the previous listed fuels, ammonia is primarily stored at low temperatures (-33°C, 1.1-1.2 bar) or pressurized (25°C, 17 bar) where energy densities can reach 8.5 and 13.77 MJ/L, respectively. Ammonia's higher volumetric energy density makes it a more viable candidate than hydrogen for high-power energy conversion systems, particularly in deep-sea marine and heavy-duty transportation applications. A comparison of the volumetric and gravimetric energy densities of these alternative options alongside traditional fuels is provided in Figure 1.1.

Although ammonia has a lower energy density than conventional hydrocarbons, its main advantage as a renewable, carbon-free fuel shows in its storage requirements compared to hydrogen. To achieve realistic volumetric energy densities, hydrogen needs to be kept at extreme conditions - either compressed to 700 bar or a cryogenic liquid state at -253 °C. Conversely, anhydrous ammonia can be stored as a liquid under moderate pressures ($\approx$ 10 bar) at ambient temperature or refrigerated to -33 °C at atmospheric pressure.

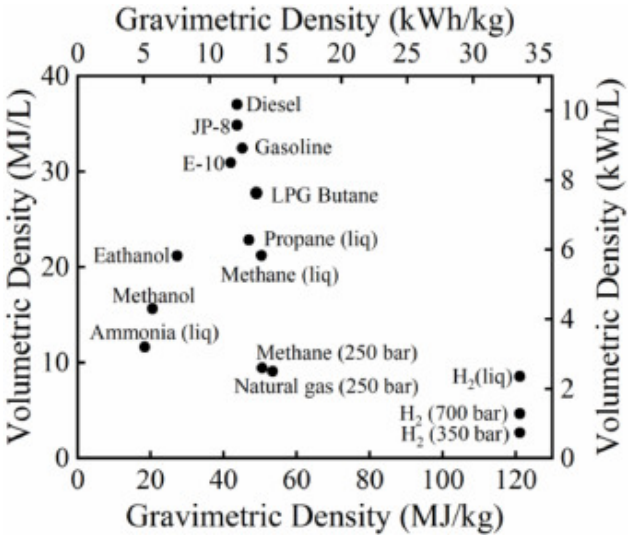

Figure 1.1: Comparison of gravimetric and volumetric densities of multiple fuels [3].

Despite these advantages for ammonia, neat ammonia presents constraints as a fuel. Ammonia exhibits low laminar flame speeds, narrow flammability limits, high autoignition resistance, high minimum ignition energies (MIE), long ignition delay times, and high NOx emissions when compared to traditional hydrocarbons and other renewable fuels, as presented in Table 1.1. These challenges hinder ammonia's application as an alternative fuel.

Ammonia combustion presents a challenge due to the production of nitrogen oxides (NOx), from the abundance of nitrogen in the fuel. Compared to conventional hydrocarbons, where NOx is generated from the nitrogen in air, ammonia combustion converts the nitrogen in the fuel and air through multiple species, including nitric oxide (NO), nitrogen dioxide (NO_2), and nitrous oxide (N_2O). This pathway through the fuel is difficult to mitigate, leading to increased emission lev-

Table 1.1: Volumetric energy densities and combustion properties of various fuels compared to NH_3. Laminar flame speeds (S_L) are at 298 K, 1 atm; Ignition delay times (IDT) are generalized for high-pressure/temperature engine conditions [4–7].

Fuel	Vol. Energy Density (MJ/L)	S_L (cm/s)	IDT (ms)	MIE (mJ)
Liquefied Ammonia (NH_3)	11.5	7.0	$\sim 500+$	680
Cooled Hydrogen (Liquid)	8.5	210.0	< 1.0	0.017
Compressed Hydrogen	5.6 (700 bar, 25°C)	210.0	< 1.0	0.017
Methane (CH_4)	22.2 (Liquid)	37.0	~ 15	0.28
Diesel	32.89	~ 40	1 – 5	0.23
Gasoline	30.93	~ 35	10 – 50	1.35

els higher than current regulatory standards for power generation and transport for hydrocarbons. By decomposing ammonia (which will be explained in the next section), hydrogen significantly increases the reactivity, subsequently raising the flame temperatures, increasing this thermal-NOx. As these nitrogen oxides are harmful to the environment it is necessary to limit them. Engineers can limit this using combustion strategies, like lean-premixed combustion to control the temperature, or rely on post-combustion exhaust-gas after treatment like selective catalytic reduction. Without these, elevated NOx levels remain a barrier to ammonias adoption.

1.1.1 Ammonia Decomposition

To adjust for these disadvantages in neat ammonia, fuel reforming, cracking, or decomposition can be used prior the to the combustion chamber. Thermal, catalytic, or plasma-assisted decomposition methods can be used to break a fraction of the ammonia into its constituent components (nitrogen and hydrogen using the global reaction equation (Equation 3.2).

$$\mathrm{NH_3} \longrightarrow \%\mathrm{D}(\frac{3}{2}\,\mathrm{H_2} + \frac{1}{2}\,\mathrm{N_2}) + (1 - \%\mathrm{D})\mathrm{NH_3} \tag{1.1}$$

By decomposing NH_3 into NH_3, H_2, and nitrogen (N_2), combustion characteristics are improved, drastically improving both laminar and turbulent flame speeds, and ignition delay times [8, 9]. This is due to the addition of highly reactive hydrogen accelerating radical chain-branching pathways, increasing the overall reactivity and flame temperature of the mixture.

Many methodologies for cracking ammonia have been evaluated in relevant literature from Asif et al. [10], providing a review detailing current plasma-based, electrochemical, thermal, and catalytic decomposition methods. Faingold et al. [11], for instance, demonstrated that plasma-assisted decomposition can effectively reform ammonia-air mixtures prior to induction, resulting in enhanced combustion efficiency. Furthermore, Choe et al. [12] observed that plasma-assisted combustion could be optimized to suppress NOx emissions, which remains an obstacle for high-scale ammonia use.

By using Equation 3.2, the fuel can be optimized to a certain decomposition fraction (%D) to give specific molar concentrations of NH_3, H_2, and N_2, based on the application. This variable decomposition ratio provides control that can be changed to satisfy different engine setups. For instance, a spark-ignited engine may require higher hydrogen concentrations (higher decomposition ratios) to ensure fast flames and prevent misfire under lean conditions. On the other hand, a dual-fuel compression-ignition engine utilizing a diesel pilot can operate at lower decomposition fractions, using the ignition of the pilot fuel to achieve total burning and reduce ammonia slip. Current thermal-catalytic cracking technologies are capable of achieving these 30-40% decomposition ranges at moderate temperatures and at the rates required for engine operation, as reviewed by Deka et al. [13].

1.1.2 Ammonia in Engines

Ammonia presents a promising carbon-free fuel with applications from spark-ignited (SI) engines, dual-fuel compression-ignition (CI) engines, and gas turbines. Research into fundamental combustion phenomena, specifically laminar flame speeds (S_L) and diesel droplet ignition, is critical for all these areas as it provides the baseline data required for kinetic modeling, needed for engine design.

Figure 1.2 illustrates the differences in ignition and combustion between a spark-ignited engine and a diesel-piloted dual-fuel compression engine. In a spark-ignited engine (Figure 1.2a), premixed fuel-oxidizer is introduced into the cylinder during the intake stroke. After the compression stroke, a spark plug introduces energy, producing a sustaining flame. The resulting flame front

propagates through the piston volume, where the rate of thermal expansion performs work on the piston to generate power.

On the other hand, the dual-fuel strategy shown in Figure 1.2b uses a high-pressure pilot injector to initiate combustion. In this setup, the ammonia-oxidizer mixture is compressed until it reaches conditions close to autoignition. Near top-dead-center (TDC), a small "pilot" amount of diesel is injected. These liquid droplets atomize and evaporate, forming a vapor boundary that auto ignites due to the high temperatures and pressures, as shown in Figure 1.3. This ignition source then triggers the propagation of the bulk ammonia flame.

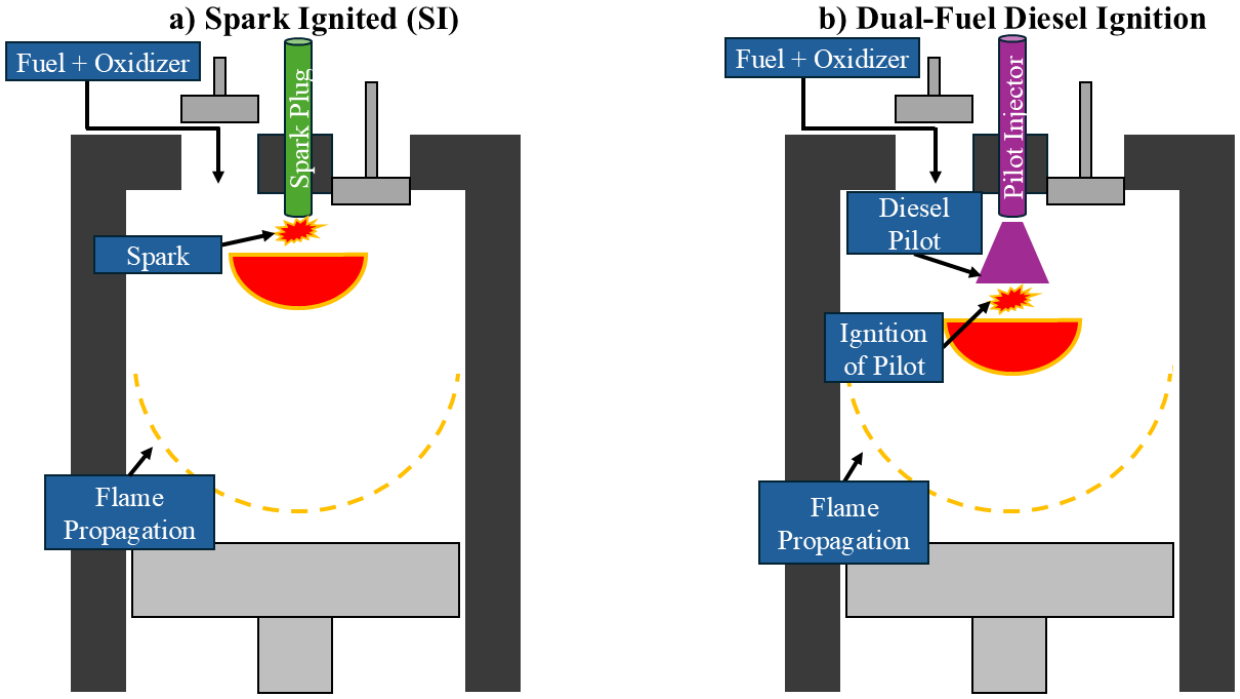

Figure 1.2: Cartoon of spark-ignited (SI) engine compared to a diesel-piloted dual-fuel compression engine.

Within SI engines, the laminar flame speed is one of the primary chemical kinetic properties providing insight onto the total mixture burning rate. Neat ammonia's low flame speed requires the addition of hydrogen via decomposition to accelerate the flame speed, as explained previously in Section 1.1.1. In dual-fuel engine configurations, while the compression and ignition of the diesel pilot is the initial ignition source, laminar flame speed is still an important parameter explaining the

subsequent flame propagation. The entire ammonia mixture must be consumed completely within the expansion stroke to avoid ammonia-slip and reduction in brake thermal efficiency. Understanding and predicting the flame speeds and ignition delays of these mixtures across simultaneous high-pressure and temperature conditions is necessary for designing engines transitioning to ammonia.

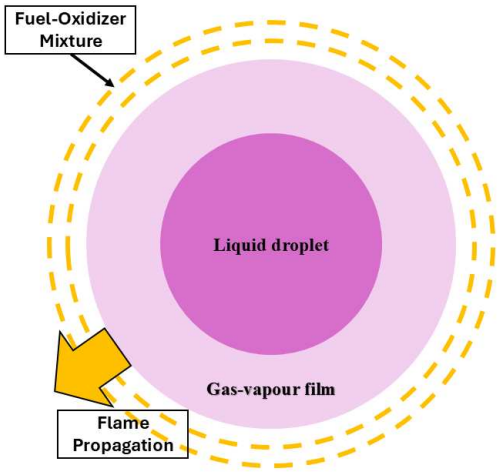

Figure 1.3: Cartoon of droplet evaporation and the subsequent flame propagation as a result.

Dual-fuel combustion utilizing ammonia and diesel pilot injection is an important research field aiming to phase out and recommission current hydrocarbon engines. Many research groups have evaluated this fuel pair to determine its viability in the large-scale marine engine sector and other applications [14–18].

To understand the limits of these ammonia dual-fuel configurations under engine conditions, small, controlled engine testing is necessary. Li et al. [18] used a 270-mm bore, maritime medium-speed single-cylinder engine under high loads to evaluate the ammonia energy ratio (AER), which quantifies the exact fraction of total fuel energy entering the cylinder that is supplied by ammonia. They demonstrated that stable combustion regimes were maintained at a AER of 86%. Emissions peaked at 35.2 g/kWh, with a simultaneous non-monotonic increase in nitric oxide (NOx) as a function of AER, stabilizing once the AER reached 70%. The authors concluded a deeper understanding of the coupling between flow fields and chemical kinetics are mandatory for future integration with computational fluid dynamics (CFD). Specifically, data is required to better under-

stand chemical kinetics and pollutant formation pathways, highlighting the necessity of validation chemical mechanisms for ammonia and ammonia/diesel dual-fuel combustion at these engine conditions.

Another study from Kishore et al. [16] used a four-stroke 83 mm bore at an engine speed of 1800 rpm to also evaluate the AER. Their findings highlighted the thermodynamics problems of using ammonia in smaller geometries. At an AER of 47%, the brake thermal efficiency (BTE) of the engine dropped to 23.3%, representing a 2.2% decrease in efficiency when compared to the baseline diesel operation. Furthermore, increasing the AER from 0–47% introduced changes in the heat release and combustion, significantly delaying the start of combustion and decreasing the combustion duration. Chemical simulations performed alongside the testing suggested a coupling with kinetics, indicating that there was higher consumptions of the hydrogen radical with increased ammonia.

While laboratory research continues to show chemical kinetic challenges, implementation in industry has been achieved. The German maritime company Wartsila designed and successfully demonstrated the first commercial-scale, four-stroke ammonia dual-fuel marine engine. Operating under a low-pressure Otto cycle - which is highly suitable for ammonia due to safety, efficiency, and potential reduction of green house gases - the engine demonstrated a 90% reduction in greenhouse gases at a AER of 95% [19, 20]. The company's testing showed that performance, torque curves, and power densities are similar to modern dual-fuel natural gas (LNG) engines.

These preliminary experimental and commercial dual-fuel ammonia/diesel studies provide insight into the chemical interactions occurring between the hydrocarbon diesel and nitrogen chemistry associated with the oxidation of ammonia. Understanding these pathways is essential for introducing ammonia as a zero-carbon fuel across the maritime fleet and other applications, necessitating basic chemical kinetic work at engine-relevant conditions.

1.2 Gaps in literature

Laminar flame speeds (S_L) are an integral basic chemical kinetic property needed to understand basic combustion chemistry and how fuels operate in an internal combustion engines and

power generation applications. Developing a fundamental understanding of the fuel chemistry at a wide range of temperatures and pressures is a prerequisite for building a comprehensive chemical kinetic mechanism used in the predictive design of next-generation combustion devices. A chemical kinetic mechanism is a collection of species and elementary reactions that describe the pathways a fuel or any molecule takes as it oxidizes under varying pressures and temperatures. To validate and tune these kinetic mechanisms, high-fidelity experimental data at both low and high temperature/pressure regimes is needed.

While an ideal and comprehensive mechanism would capture every possible elementary reactions and intermediate specie involved in the combustion process, practical modeling constraints require a compromise. When implementing these kinetic models into a multi-dimensional computational fluid dynamics (CFD) model to simulate combustion, large and detailed mechanisms introduce computing challenges. The large scale of solving ordinary and partial difference equations increases simulations run times and requires extensive computational resources. To mitigate this, mechanism reduction is necessary to eliminate non-critical reaction pathways through a coupling of experimental measurements and modeling. This approach ensures the chemistry to run efficiently in complex flow without sacrificing accuracy.

Validating these mechanisms relies heavily on experimental laminar flame speed measurements. However, gathering this data becoming challenging at engine-relevant conditions (elevated temperatures and temperatures) due to experimental constraints. Consequently, the majority of existing literature focuses on isolated thermodynamics regimes limited by testing hardware. Few data is available at these conditions, necessitating these measurements to ensure accurate mechanisms. Table 1.2 presents a list of all relevant flame speed measurements at these elevated thermodynamic conditions.

Table 1.2: Comparison of relevant, elevated thermodynamic ammonia/hydrogen flame speed studies in literature.

Study	ϕ	H_2% / %D	P [bar]	T [K]	Device
Figueroa-Labastida et al. (1) [21]	0.8–1.2	0–60	1	500–820	ST
Figueroa-Labastida et al. (2) [22]	0.75–1.25	0	1	295, 477–771	ST
Kanoshima et al. [23]	0.8–1.2	0	1–5	400–500	CVC
Mei et al. [8]	0.7–1.4	10–60%D	1–10	298	CVC
Zhang et al. [24]	1.0	0–100	30	750–986	SP-RCM
Nolte et al. [25]	0.6–1.3	50	4–9	571–618	SP-RCM
Shawnam et al. [26]	0.7–1.3	20–40	1	300–720	DC
Present Work	**1.0**	**0–42.5%D**	**20–30**	**760–850**	**DP-RCM**

ST: Shock tube; CVC: Constant volume chamber; SP-RCM: Single-piston RCM; DP-RCM: Dual-piston RCM; DC: Diverging channel.

1.2.1 Low temperature/pressure flames

For low- temperature/pressure regimes - defined as atmospheric conditions (298 K, 1 atm), up to moderate pressures (< 10 atm) and lower initial temperatures (< 473 K) - the majority of literature utilizes constant volume combustion chambers (CVCC, as seen in Figure 1.4) or heat flux burners. Because these experimental devices are relatively simple to build and optical access is straightforward, a vast amount of data exists for these conditions. Many of these studies overlap in their conditions, primarily varying the fuel mixture blend ratios and the chemical kinetic mechanisms under evaluation. Consequently, only the most relevant and representative studies to this work within this low-regime are reviewed [8, 27–48].

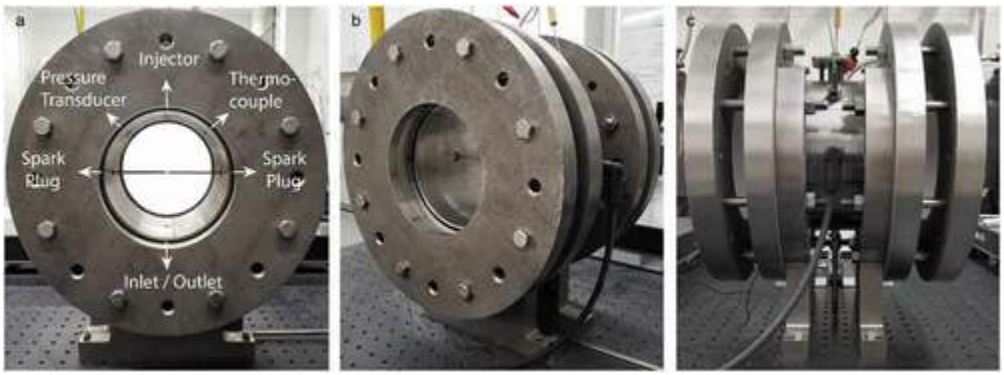

Figure 1.4: Example of a constant volume combustion chamber (CVCC) from University of Massachusetts Lowell [49].

Mei et al. [8] evaluated the effects ammonia decomposition had on laminar flame speeds at 298 K and up to 10 atm. More importantly, this remains to be one of a few low-temperature studies to achieve pressures up to 10 atm. Their testing matrix covered ammonia decomposition ratios from 10% to 80%, in increments of 10%, spanning a range of equivalence ratios (ϕ).

The group found that with an increase in decomposition percentage and decrease in pressure, the measured flame speed monotonically increased. Under slightly rich conditions ($\phi = 1.1$, 1 atm), a 40% decomposition ratio yielded an unstretched laminar flame speed of 38.1 cm/s, matching propagation rates similar to that of methane-air (CH_4) mixtures under the same conditions. Furthermore, as the decomposition ratio and pressure increased, fine, cellular instabilities were prominent in the flame front. Sensitivity analyses from the study showed that while current chemical kinetic mechanisms demonstrated reasonable agreement at matching the experimental laminar flame speed data, the propagation rate was highly constrained by the chain-terminating reaction $H + O_2 (^+M) \longleftrightarrow HO_2 (^+M)$.

Despite the use of CVCC's for measuring these lower-temperature and pressure flame speeds, the slow combustion of ammonia introduces errors in measurement due to flame buoyancy. Because the flame propagates slowly, the duration of burning time is long. This allows for natural buoyancy forces to act on the flame where the hot, burned, low density gas inside of the flame rises to the top of the chamber, relative to the cold, unburned gas. This rise affects the expanding flame

from an ideal, spherical to an egg-like shape, introducing errors during post-processing. To isolate and eliminate these buoyancy effects on the flame, Zitouni et al. [48] developed a drop-tower apparatus capable of measuring laminar flame speeds under micro-gravity conditions. By dropping the combustion chamber to remove gravity, the buoyant forces are suppressed providing an accurate laminar flame speed, free of buoyancy.

Another way to remove buoyancy errors in slowly propagating flames commonly seen in these types of studies is to use a flat-flame heat flux burner. Han et al [30] used this approach to evaluate the difference between decomposed ammonia laminar flame speeds to pure NH_3/H_2 without the extra nitrogen from the decomposition process. The group measured flames at atmospheric conditions with ranges of decomposition ratios of 0.025–0.5 across a wide equivalence ratio sweep ($\phi = 0.6 - 1.4$) and compared them to the corresponding NH_3/H_2 fuel ratio to what is seen in the decomposed mixtures. Fundamentally, in simulations and sensitivity analyses, they found that the decomposition does not alter the reaction sensitivities when compared to the identical NH_3/H_2 mixtures. Experimentally, measured flames appeared to have no difference between the corresponding mixtures. However, their work exposed current mechanism limitations. While the mechanisms that were used predicted flame behavior well for mixtures with low amounts of hydrogen, nearly all mechanisms diverged from the experimental data once the decomposition ratio exceeded 35%. This overprediction as a result from hydrogen highlights the need for more accurate transport and reaction mechanisms.

1.2.2 High temperature/pressure flames

To capture the chemical kinetics and transport phenomena under conditions that occur directly in an engine, experiments must be conducted in a well-defined experimental setup at simultaneous elevated pressure and temperatures. However, because simultaneous high pressure and temperature environments often involve fluid flow and a more intricate and expensive setup, this regime is highly limited in literature. The majority of these studies have been forced to either isolate high temperatures at low pressures, or high temperatures and moderate pressures.

1.2.3 Shock Tube Flames

A major milestone in obtaining laminar flame speeds of ammonia was first achieved by Figueroa et al. [22] across a range of high temperature, atmospheric conditions . Their first study established the first pure ammonia flames at initial temperatures ranging from 500–771 K. The group found that at higher temperatures, the Okafor [50] and Zhang [51] mechanisms were the most accurate at these higher conditions. Chemically, the fundamental chain-branching reaction: $H + O_2 \longleftrightarrow O + OH$ was the most influential on the overall laminar flame speed. This study was significantly novel, as it was the first of its kind to fill the gap in high-temperature kinetic validation.

Building directly onto their previous work, Figueroa et al. [21] investigated the effects hydrogen had on the laminar flame speeds in ammonia mixtures. This extended the previous temperatures up to 810 K, though remaining at atmospheric pressures due to constraints with the experimental test tube facility. They found that the addition of hydrogen drastically improved the structure of the flame, mitigating the non-idealities in the pure ammonia flame, mainly the presence of buoyant forces on the flame. This introduction of hydrogen significantly increased the flame speeds and subsequently made a more spherical, uniform flame. Furthermore, the measured laminar flame speeds showed that they increased monotonically as a function of the hydrogen ratio, similar to what is seen at low- temperature and pressure conditions. They also concluded that with the addition of hydrogen, nitrogen chemistry inherent to ammonia combustion plays a less significant role in the overall reaction.

1.2.4 RCM Flame Studies

To study the coupling of high temperature and pressures, laminar flame speed kinetic studies have moved to rapid compression machines, primarily single-pistons. Recently, two single-piston studies were conducted by Nolte et al. [25] and Zhang et al. [24] to evaluate the combustion behavior of ammonia and hydrogen mixtures at these conditions. Nolte et al. achieved pressures of 4 and 9 bar with temperatures ranging from 518-671 K, while Zhang et al. achieved a pressure of 30 bar and temperatures of 750-985 K.

Zhang et al. investigated the end-gas autoignition of NH_3/H_2 fuel mixtures in a single-piston RCM at temperatures ranging from 750–986 K at a pressure of 30 bar, one of the only studies having investigated ammonia flames at elevated temperature/pressure conditions. However, instead of reporting the fundamental unstretched, unburned laminar flame speeds necessary for fundamental mechanism validation, the group reported raw flame propagation rates. For hydrogen blending fractions ranging from 0% to 20% H_2, the group recorded that flame propagation rates remained under 600 cm/s. The flame fronts documented exhibited highly non-circular, lobed, and wrinkled morphologies (as seen in Figure 1.5), in contrast to the symmetric, smooth spherical flames needed in fundamental flame speed studies. Furthermore, because their experimental setup utilized chemiluminescent diagnostics rather than high-speed schlieren imaging, it was difficult to resolve the fine cellular instabilities that are likely present in these high-pressure, hydrogen containing flames.

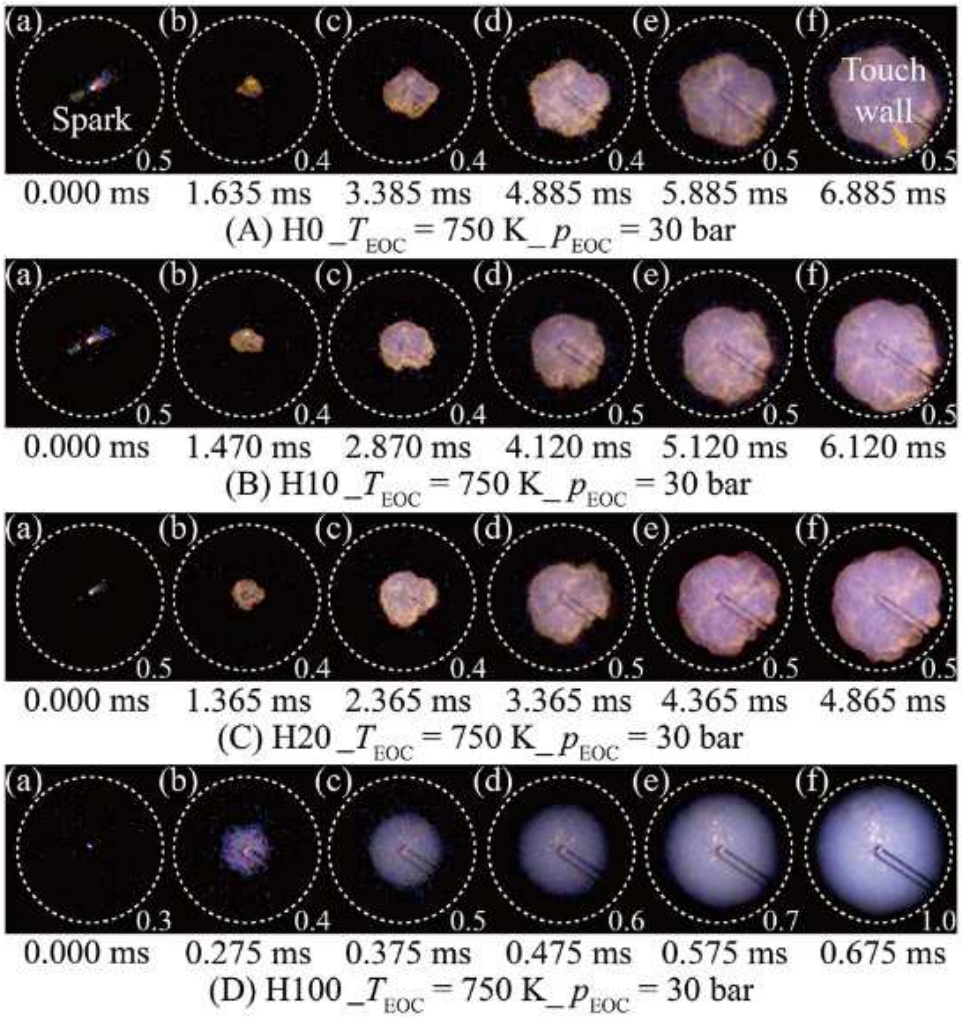

Figure 1.5: End-view images in the flame propagation stage of different ammonia/hydrogen fuel mixtures seen in the single-piston flame study from Zhang et al. [24].

While useful, this study focuses on quantifying end-gas autoignition of NH_3/H_2 mixtures at these elevated conditions. While they do report flame propagation rates, these are not corrected for stretch or reported as unburned flame speeds, essential for mechanism validation.

In the lower pressure RCM experiments from Nolte et al., laminar flame speeds were measured across varying equivalence ratios. Consistent with established literature, the maximum flame speeds for the ammonia mixtures occurred at slightly rich equivalence ratio ($\phi = 1.1$). Their data also demonstrated that the the addition of hydrogen (50%/50% NH_3/H_2) significantly increased the laminar flame speed by around 10 cm/s at 9 bar and 630 K.

To evaluate current chemical kinetic mechanisms, the group simulated flame speeds using three mechanisms from CONVERGE C3, NUIG, and KAUST. The mechanisms demonstrated close agreement with the experimental data with pure ammonia. However, the models had difficulty across all hydrogen-containing mixtures, where all mechanisms significantly overpredicted the experimental flame speeds with a discrepancy of 20 cm/s. This overprediction highlights the necessity for experimental data of NH_3/H_2 at high pressures and temperatures.

In addition to measuring laminar flame speeds, Nolte et al. [25] characterized the flow field to ensure the measurement of true laminar flame speeds, important for the validation of flame speeds found in a rapid compression machine. The influence of electrode-induced turbulence was investigated using a Constant Voltage Anemometry (CVA) system (Tao Systems Model 4–600). These experiments were conducted using pure nitrogen (N_2) at an end-of-combustion (EOC) pressure of 5 bar and a temperature of 685 K. The system monitors the heat dissipation of a hot wire probe, P_W, which is governed by the heat convection between the wire and the fluid $\Delta T_{W,f}$ is the temperature difference between the wire and the fluid.

Figure 1.6a illustrates the comparison between the dissipation ratio with electrodes (P_W) and the reference case without electrodes (P_{W0}), alongside the evolution of $\Delta T_{W,f}$. The data shows that during the initial stages of compression (starting at -28.5 ms), the dissipation ratio increases because the increase in flow velocity—and thus the convective heat transfer—outpaces the reduction in $\Delta T_{W,f}$ caused by rising fluid temperatures. Directly following EOC (0 ms), both cases exhibit high dissipation, but the presence of electrodes induces significant flow disturbances that cause the P_W/P_{W0} ratio to deviate sharply after 3.5 ms. This deviation is driven by the cooling effect of the electrodes and increased local vorticity. These disturbances gradually decay until approximately 76 ms after EOC, where the dissipation traces for both experimental conditions reach qualitative agreement. This 76 ms mark identifies the start of the "undisturbed time frame", representing the optimal ignition timing to ensure flame propagation occurs in a nearly stagnant, laminar flow field. This window remains viable until roughly 200 ms, after which the roll-up vortex from the piston crevice begins to influence the flow.

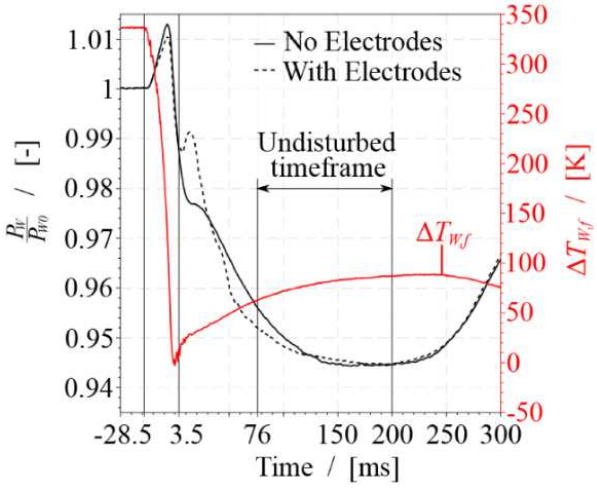

(a) Wire dissipation and temperature traces using a hot-wire anemometer comparing the difference between having electrodes and not having electrodes.

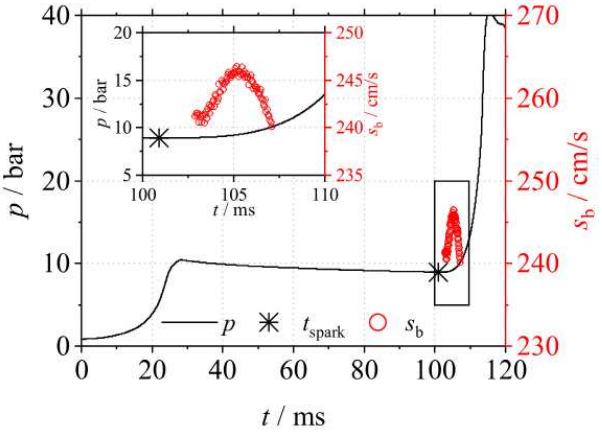

(b) Pressure trace and flame measurement location.

Figure 1.6: Traces of hot wire anemometer and combustion experiments done in a single-piston RCM from Nolte et al. [25] at Aachen University.

While single-piston RCM's generate valuable data, they are frequently limited by residual bulk-flow motion and substantial heat loss, necessitating long delays after TDC to reach a quiescent state required for flame speed measurements as seen in the work from Nolte et al. where they needed to wait around 70 ms until ignition based upon their anemometer work.

All the studies presented usher the need for a better understanding of hydrogen chemistry in hydrogen-rich ammonia blends. While these studies provide valuable insight into ammonia laminar flame speeds, all studies focus on lower thermodynamic conditions, not capturing the affects of high pressures and temperatures on flame propagation seen in real-world combustion.

1.3 Objectives of this work

The overarching objectives of this work is to advance the fundamental understanding of ammonia (NH_3) as a carbon-free, renewable alternative fuel capable of replacing conventional hydrocarbons in engine-relevant applications. To achieve this, this study acts as a part of a larger initiative, isolating and quantifying the flame propagation characteristics and diesel ignition delay times of decomposed ammonia mixtures at engine-relevant conditions. These experiments help to explain ammonia's applicability in spark-ignited (SI) and dual-fuel compression-ignition

(CI) internal combustion engines. To complete these experiments, a dual-piston rapid compression machine (RCM) equipped with a laser-ignition system and a diesel droplet generator - both developed in previous works at Colorado State University - was used to obtain stagnant, near quiescent thermodynamics environments. The research objectives are broken into two experimental and numerical projects.

The objectives for characterizing flame propagation characteristics are to understand the effects of ammonia decomposition on fundamental flame speed and flame morphology. This includes evaluating current chemical kinetic mechanisms and their ability to predict flame speeds at these elevated conditions through 1-D simulations in Cantera. In addition, assessing the predictive capabilities of current numerical frameworks and mechanisms in 3-D computational fluid dynamics (CFD) simulations using CONVERGE. Validating these models in the well-defined geometry of the RCM is necessary for application in large-engine simulations. If current mechanisms cannot accurately replicate combustion events in this simplified, quiescent environment, their reliability in large-scale engines with complex geometries hinders ammonia's use as a potential fuel.

The objectives for diesel-ammonia dual-fuel ignition aim to measure the ignition delay times of diesel droplets in a premixed decomposed ammonia mixture. An understanding of the underlying chemistry is important between hydrogen diffusion and oxygen availability, providing information on the rolls of these gases. Overall, understanding the delays of these mixtures gives insight into the feasibility of using decomposed ammonia blends in a dual-fuel configuration.

This thesis will cover the entire study including the experimental and numerical setup and their respective results. Chapter 2 covers the experimental setup including the rapid compression machine, hardware, and safety. Chapter 3 outlines the experimental methods and data-processing. Chapter 4 will outline the numerical framework for both 1-D and 3-D CFD simulations. Chapters 5 and 6 will cover the respective experimental and numerical results. Finally, Chapter 7 concludes the findings in this study and provides recommendations for future work.

CHAPTER 2 – EXPERIMENTAL SETUP

This chapter will cover the entire experimental and lab setup of the rapid compression machine; including the RCM itself and implications that come with it, ammonia safety and sealing, the mixing tanks and the procedure used, and finally the hardware and imaging for the the laser, schlieren, and droplet generator.

2.1 Rapid Compression Machine

As outlined in Chapter 1.2, existing laminar flame speed data for alternative fuels remains at atmospheric conditions, high temperatures - low pressures, or low temperatures - intermediate pressures. To contextualize the use of the CSU dual-piston RCM, it is necessary to evaluate the tradeoffs between this experimental setup and other conventional experimental devices used in flame speed experiments.

Atmospheric and low temperature - moderate pressure data sets are primarily obtained using a constant-volume combustion chambers or spherical bomb vessel which are enclosed, pressurized vessels containing a homogeneous fuel-oxidizer mixture. A central ignition source, usually electrodes, propagate a spherically expanding laminar flame outward. These devices are integral to combustion science since the stagnant environment isolates chemical kinetics and thermodynamics from bulk fluid motion. However, obtaining engine-relevant conditions in spherical bomb vessel is very difficult for many reasons. Achieving these high pressures requires a large amount of the fuel-oxidizer mixture, which is a safety hazard and not cost effective. In addition, elevating these initial temperatures requires a large amount of heating of the walls which can trigger premature autoignition at the walls.

High temperature - low pressure data sets are generated primarily using a shock tube by breaking a physical diaphragm separating a high-pressure 'driver' gas from the low-pressure 'drive' gas mixture (the fuel-oxidizer mixture). This expansion creates a shockwave that propagates and compresses, heating the fuel-oxidizer mixture almost instantaneously. Shock tube experiments are

perfect for obtaining temperatures greater than 1000 K and a range of pressures, however, have more difficulties obtaining lower temperature conditions below autoignition conditions. This is due to the pressure in the driver section, to achieve these lower temperatures, less driver gas is applied making the shock much weaker. This in return affects the testing zone, decreasing the timing zone of measurement due to fluid flow. To overcome this challenge, the group at Stanford University [21, 22] significantly increased the driven section and decreased the driver section, giving the group more unperturbed test time to capture the flame propagation.

To bridge the experimental gap between atmospheric conditions and high-temperature low-pressure conditions, rapid compression machines are used. The machines are categorized by single-piston (SP) and dual-piston (DP) setups. While both of these variations are capable of elevated temperatures and pressures, their fluid dynamics and heat loss greatly differ.

Rapid compression machines simulate a single stroke of an internal combustion engine, compressing the fuel-oxidizer mixture to achieve thermodynamic states at engine-relevant conditions that closely approximate adiabatic compression. In a standard test, the majority of the total pressure and temperature rise occurs within the final $\sim$5 ms before TDC. This rapid increase of pressure in such a short time is needed to minimize chemical reactions during the compression stroke [52].

SP RCM's introduce turbulence into the core of the combustion chamber as the compression of the single piston generates roll up vortices. DP RCM's on the other hand, utilize two symmetric pistons where the opposing configuration negates bulk-flow motion, generating a near-quiescent environment. Another problem with SP configurations is heat loss. SP's have a significant amount of heat transfer at the end-of-compression (EOC) as the gas compresses against a cold or heated end wall, where the heat in the gas dissipates to the walls. Due to the turbulence generated in the SP setup, a longer wait time between top-dead-center (TDC) and ignition is needed for the environment to become quiescent allowing for an undisturbed flame. This long wait time allows for more heat transfer, decreasing the initial temperature, generating uncertainty. However, in a DP setup, the hot gas is centrally located between the two symmetric, opposing pistons keeping

the gas hot, with the only heat loss occurring at the walls of the chamber. In addition, spark timing can be timed much earlier due to the quiescent environment.

Figure 2.1 presents a pressure-temperature diagram of the previously listed experimental devices compared to the motored engine region. RCM's are capable of reaching these engine-relevant, motored engines perfectly, while still allowing more work in the engine regime by increasing pressures.

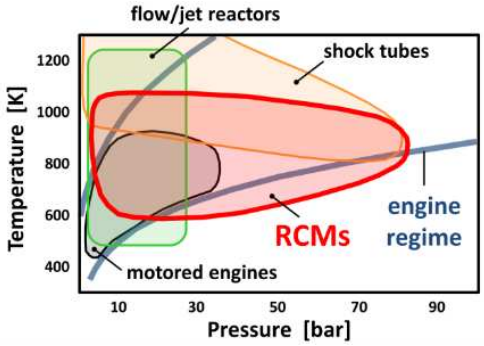

Figure 2.1: Temperature-pressure graphs of operating conditions of different experimental devices and combustion engines [53].

The Colorado State University (CSU) rapid compression machine (RCM) is a unique experimental device capable of achieving a wide range of low- to intermediate-temperatures (600-1200 K) and moderate- to high-pressures (5-80 bar). By rapidly compressing a fuel-oxidizer mixture, the machine decouples complex flow interactions from pure chemical kinetics. This capability makes it an ideal experimental device for isolating and characterizing fundamental chemical interactions under engine-relevant conditions. This dual-piston RCM was originally manufactured by Marine Technology, LTD in Galway, Ireland. This specific machine is capable of achieve compression ratios of 11.8:1, depending on the chamber configuration due to extra volume in window cavities and other plugs on RCM chambers. The chambers used in this study have a compression ratio of around 11.3:1. The full compression stroke can be completed in under 15 ms, however in this study it remains around 20 ms, while minimizing fluid dynamics with the compression stroke.

The RCM is comprised of two hydraulic/pneumatic drive cylinders facing opposite one another as seen in Figure 2.2. Compression is provided by high-pressure air stored in the bellows (located at the ends of the drive cylinders) where the air pressure can be changed directly on the control box. In this study, following previous studies, the air pressure was set to 200 psi allowing pistons to come from bottom-dead-center (BDC) to top-dead-center (TDC) within ∼20 ms. The piston/plunger configuration and timing of compression is controlled using hydraulic locks, keeping the pistons in the BDC position, which are released to initiate compression.

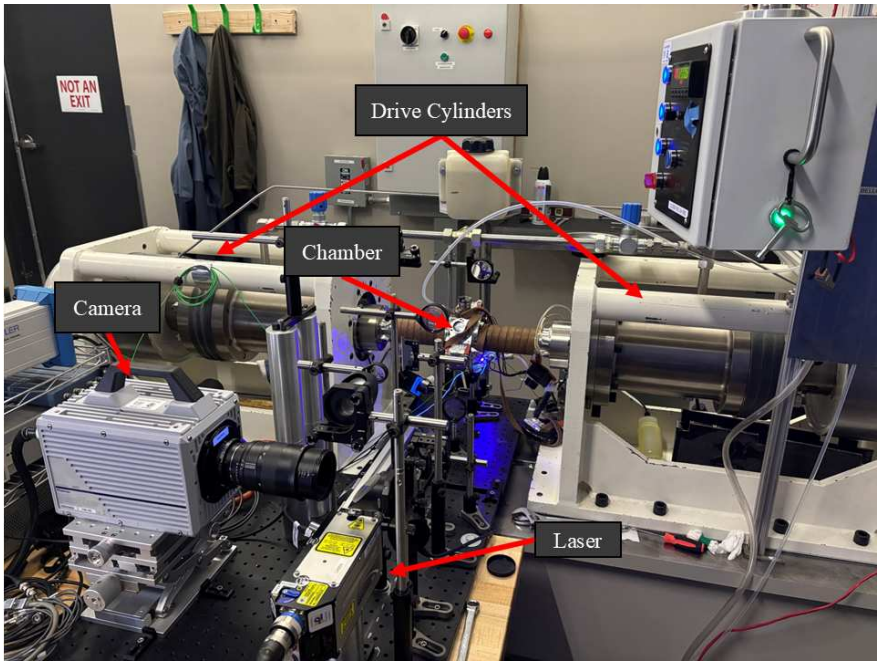

Figure 2.2: Picture of the rapid compression machine.

The RCM system inherently generates a higher amount of error, compounding from the mechanical system of the hydraulic and pneumatics (piston offset) through the data acquisition system to the error seen in pressure transducers and thermocouples and the flame measurement method. Given the nature and complexity of this propagating error, this thesis will cover a small part of the uncertainty associated with the thermodynamics conditions, bulk flow, and variance in the experimental data.

However, a comprehensive uncertainty analysis is an objective of future work. This must include the error for all experimental instrumentation and the variations associated with the visual schlieren flame measurement technique. To assist with this, the following uncertainties have been accounted for: uncertainties regarding filling and mixing which are detailed in Section 2.3, variance of the experimental results in Chapter 5, and the validation of thermodynamic conditions using CFD in Chapter 6. Quantifying the total error associated with the RCM is a necessary step for the validation of experiments and subsequent mechanism tuning. Below in Table 2.1 is the accuracy associated with pressure transducers and thermocouples within the RCM setup.

Table 2.1: Accuracy of different experimental devices used in the RCM.

Tool	Location	Measurement	Accuracy
MKS Transducer	Mixing Tank	Pressure	0.5%
Kistler 601CAA	Combustion Chamber	Pressure	0.3%
Omegadyne DPGM	Chamber Fill	Pressure	0.008%
Thermocouples	Chamber/Mixing Tank	Temperature	0.75%

2.1.1 Piston Offsets

A significant challenge inherent to the dual-piston RCM is the synchronization of the opposing pistons. As illustrated in Figure 2.7, piston offsets, defined as the difference in arrival time between the two opposing pistons at TDC, can significantly affect the flow field inducing flow across the chamber, influencing the flame surface area and measured propagation rate, as well as influencing the TDC thermodynamic states. To ensure a quiescent field during the measurement period during data analysis, the laser is fired 1 ms after TDC. Furthermore, cases where offsets exceeding 6 ms were omitted from data analysis as this threshold was found to correlate with significant increase in measured flame speed and visible signs of flame surface disturbance. This is further explained in Sections 2.4,5.1.26.4.

2.2 Ammonia Safety and Sealing

Anhydrous ammonia (NH_3) is a clear, colorless gas that is highly toxic and corrosive to tissue when concentrated. It is absorbed into the body through inhalation, ingestion, eye contact, and skin contact. Upon contact with water on/in the human body, ammonia reacts with water to form ammonium hydroxide (NH_4OH) a highly alkaline corrosive solution and a common chemical in household cleaners. In the context of this study, inhalation is the primary safety concern due to the risk of leaks from the RCM or in the gas manifold. To mitigate these potential risks and ensure a safe testing environment, a safety strategy was implemented, focusing on material chemical compatibility, NH_3 gas detection, personal protective equipment (PPE), and emergency safety plans.

Ammonia's chemical properties make it challenging to use with many existing and commonly used o-rings, fasteners, and valves, where it is mainly corrosive to brass and copper. Because of this, the entire gas manifold was retrofitted, replacing all brass parts with 316 stainless steel to ensure no leaks or contamination from corrosion.

Because the RCM and RCM chamber must hold very high pressures (up to 100 bar) and endure very high pressure spikes, o-rings within the combustion chamber and piston are critical. In the past, all projects used Viton as the primary material for sealing for all hydrocarbon and hydrogen-based testing due to its great thermal stability, overall function, and low cost. However, Viton is incompatible with ammonia, experiencing chemical degradation when exposed to NH_3. To resolve this, materials were reviewed using chemical compatibility charts to find potential alternatives to Viton with similar hardness ratings and sizes, but are resistant to NH_3 [54]. As seen in Figure 2.3, multiple materials were compared with all possible gases that are used in the RCM.

Possible O-Ring Materials	Argon	Nitrogen	Oxygen	Methane	Hydrogen	Ammonia
Kalrez	A	A	A	A	A	A
Butyl	B	A	D	D	A	A
Ethylene-Propylene (EPR)	A	A	A	D	A	A
Teflon (PTFE)	A	A	A	A	A	A
Neoprene	D	A	C	B	A	A
Viton	A	A	A	A	A	D
Buna-N	C	A	D	A	A	B
EPDM	A	A	A	D	A	A
FEP	A	A	A	A	A	A

A	Excellent
B	Good (Minor Effect)
C	Fair (Moderate Effect)
D	Severe Effect (not recommended for any use)

Figure 2.3: O-ring chemical compatibility chart of possible o-rings.

Ethylene propylene diene monomer (EPDM) was selected as the primary material for o-rings in ammonia testing. EPDM has great resistance to ammonia, it matches the shore hardness and elasticity to that of Viton and overall is cheaper than other alternatives like Kalrez. The only problem with EPDM is the fact that it is not compatible with methane, so for cases with methane, Viton should still be used.

However, when testing there was a problem identified with EPDM and the piston sealing o-rings. Because the piston o-rings are subject to friction against the piston sleeves, there is a possibility that these o-rings break apart. This was seen with EPDM and initial testing where at and before TDC, pieces of rubber were seen moving into the combustion chamber. As a result, Viton was continued as the primary o-ring for the piston seals as there was minimal chemical degradation.

To provide tracking of potential leaks in the system and protect lab personnel, the RCM facility was constantly monitored by two gas monitoring systems during testing. A portable electrochemical gas detector (Honeywell BW Solo) was kept on person or near potential leak points (chamber or mixing tank) during the entire filling and testing processes. Although the threshold to smell ammonia is as low as 1 ppm, the monitor is configured with a low-alarm threshold of 5 ppm. In addition to the portable sensors, a stationary Draeger Polytron 5200 gas sensor was installed at the roof, above the RCM, taking advantage of ammonia's low molecular weight relative to air. This

sensor was set to alarm at 25 ppm, following acute exposure guidelines from the CDC (Table 2.2). To complement these sensors, operators had full-face piece Honeywell North 5400 respirators with a Honeywell 75SCP100L cartridge filter on standby.

Table 2.2: Acute Exposure Guideline Levels (AEGLs) for anhydrous ammonia (NH_3) in ppm [55].

AEGL Level	10 min	30 min	60 min	4 hr	8 hr
AEGL 1 *(Discomfort, non-disabling)*	30	30	30	30	30
AEGL 2 *(Irreversible/serious effects or impaired ability to escape)*	220	220	160	110	110
AEGL 3 *(Life-threatening effects or death)*	2,700	1,600	1,100	550	390

Due to the small kinetic diameter of ammonia, the potential loss of mass during testing, and the danger of inhaling ammonia, perfect sealing is necessary for safety and exact fuel mixtures. To guarantee a perfect seal, leak-testing was executed weekly by pressurizing the RCM and gas manifold with pure hydrogen and leak testing all joints and possible leak points with a Riken Keiki SP-220 hydrogen gas sniffer. This is justified since hydrogen has the smallest kinetic diameter of the gases used (other than ammonia) and by ensuring there is no leaking for hydrogen guarantees that larger molecules do not leak, as seen in Table 2.3. Furthermore, hydrogen diffuses significantly faster than all other molecules than heavier gases due to its small molecular weight and is the first to be detected if there is a leak. Consequently, by validating that the system is fully sealed, with no leaks of hydrogen, it is assumed that ammonia and all other gases are contained without mass loss during testing.

Table 2.3: Physical properties and molecular sizes of gases commonly utilized in RCM experiments.

Species	H_2	NH_3	CH_4	N_2	O_2	Ar
Kinetic Size (pm)	289	260	380	364	346	340
Density at STP (kg/m^3)	0.0899	0.717	0.668	1.165	1.331	1.661
Molecular Weight (g/mol)	2.016	17.031	16.043	28.014	31.998	39.948

2.3 Mixing Tank Procedure

Gas mixtures that are tested in the RCM are first mixed in one of two mixing stainless-steel vessels, one being 5L and the other bring 20L [56] as shown in the schematic 2.5. For this study, the 5L tank was the only one used, cut from the original size by Miguel Valles Castro [57]. Each mixture tank is heated using heat wrap and insulated, allowing changes in initial temperature of the gas mixture. Previously used pressure relief valves were replaced with rupture discs, provided by Zook, compatible with all gases, set to a burst of pressure of 13.44 bar and temperature of $72^{\circ}F$ in case of detonation in the tank, as seen in Figure 2.4. Combusted gases are then evacuated through a blower to the outside of the building.

(a) Rupture disc

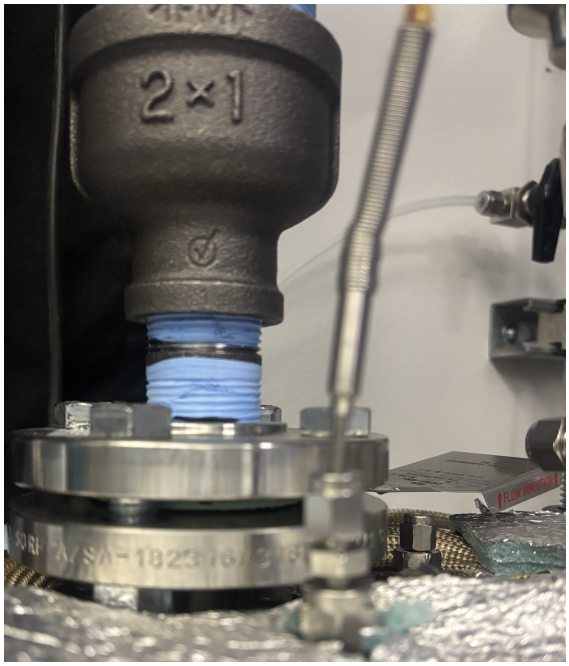

(b) Rupture disc installed and sandwiched between two flanges on the mixing tank.

Figure 2.4: Images of rupture disc installed on the mixing tanks replacing previously used pressure relief valves.

Prior to filling, the 5L mixture tank is evacuated using a Edwards E30 vacuum pump to achieve close to true vacuum. Remaining pressure that cannot be vacuumed is recorded and accounted for in the partial pressure calculations. Each tank is prepared using the partial pressure methods to a

final total pressure of 4 bar, using a MKS model 722B53TCD2FA. The pressure transducer/filling method achieved within ±5 mbar to the desired partial pressure setpoints resulting in an uncertainty in the equivalence ratio to be $<1.0\%$. The compressed gas temperature uncertainty is estimated by propagating the uncertainties in the initial temperature (±1 K), dynamic pressure (±1%), and mixture composition (±1%), resulting in an overall compressed temperature uncertainty of approximately ±7 K ($\approx 1\%$). Experimental TDC temperature exhibited a maximum standard deviation of 4.8 K within the 6 ms threshold (Table 5.1). This stability is supported by non-reacting 3-D simulations, which shows a 3 K variation between 0 and 6 ms offsets in the middle of the chamber as explained in Section 6.2.

The filling order is controlled where fuels are introduced to the tank first (NH_3 / H_2), followed by inert diluents (N_2 / Ar), and finally oxygen (O_2) to prevent detonation of the mixture during the filling process. Because the addition of these gases causes a temperature rise, a cooling period is needed after the introduction of each species. The tank is needed to return to the baseline temperature to ensure accurate pressure readings, reflecting correct molecular concentrations. Following the addition of the oxygen, the mixture is allowed to mix for a minimum of 4 hours, ensuring a homogeneous mixture prior to testing in the RCM. In these experiments ultra-high-purity (UHP300) gases are used and are purchased from Airgas.

2.4 Hardware and Imaging

2.4.1 Laser Hardware

Laser-ignition within the RCM was first designed and achieved by Dumitrache et al. [58]. Expanding on previous work from this work, the present system initiates ignition using a Quantel Q-switched Nd:YAG operating at a wavelength of 1064 nm in the single-shot configuration. To promote the development of a centrally locating, spherically expanding flame, the laser pulse energy is maintained just above the minimum ignition energy (MIE) of the mixture. The chamber used in this study was originally designed by Miguel Valles Castro [57].

The output energy of the laser is measured during every experiment utilizing a beam splitter, where it diverts 5% of the beam to an external energy meter, while the remaining 95% of the beam

is focused into the center of the combustion chamber. The resulting delivered laser pulse energy ranges from 30 to 40 mJ. This laser trigger signal is digitized using a 12-bit Picoscope 4424 data acquisition system sampling at 2 MHz. The large laser energy variation is due to the shot-to-shot variation inherent to the laser systems. Because the laser is driven by a global power setting rather than an exact energy output value, these shot-to-shot fluctuations are inevitable. These variations are recorded for every test to ensure repeatability.

It is important to note that the 30–40 mJ of pulse energy is not the total amount of energy deposited thermally into the mixture upon ignition. Accounting for a 1.24% energy loss across mirrors, lenses, and windows, and applying the thermodynamic scaling from Phuoc [59], only 7–8% of the laser energy is deposited thermally. The remaining fraction is dissipated via shockwave and radiative processes, yielding a deposition energy of 2–3 mJ. The beam path can be seen in Figure 2.5c.

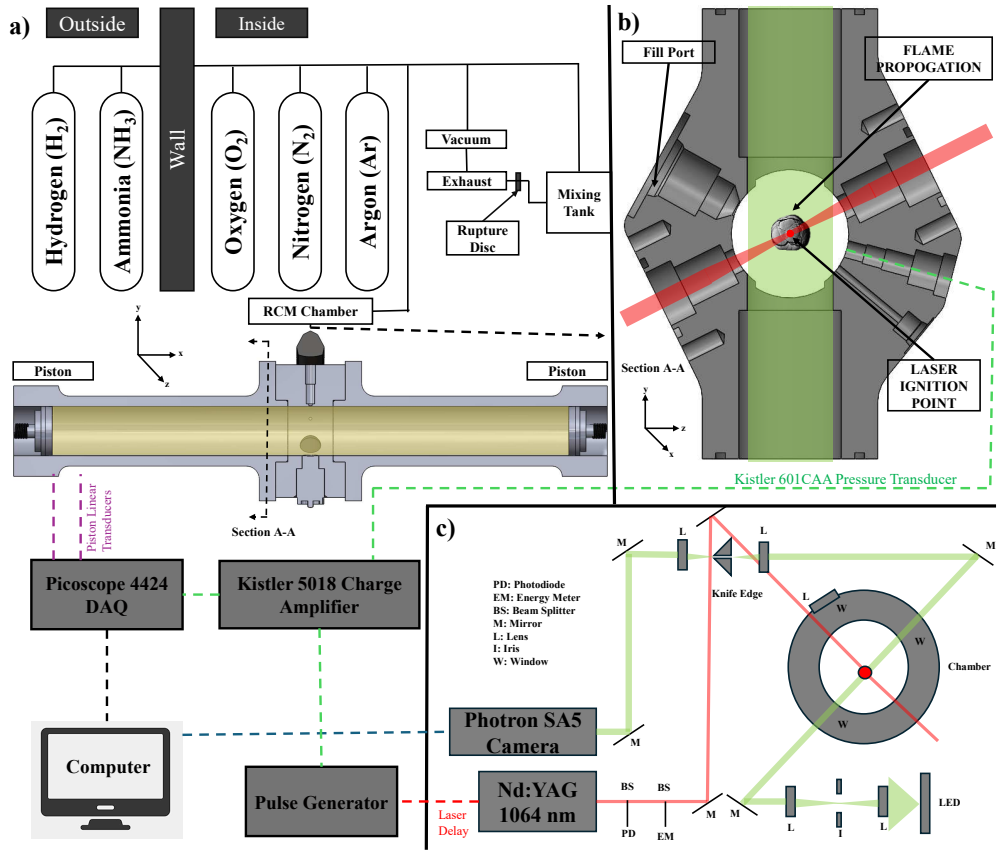

Figure 2.5: Experimental setup of the rapid compression machine where solid lines represent piping (-) and dashed lines wiring (- -). a) Shows the overall lab setup with RCM connections to the DAQ system and computer, b) shows the chamber cross-section, and c) shows the schlieren and laser setup.

Combustion inside of the chamber is visualized using a Z-type high-speed schlieren imaging configuration, detailed in Figure 2.5. This system passes collimated light from a LED source directly through the optical windows in the combustion chamber. As the flame front propagates, temperature and composition gradients create variation in the gas refractive index, deflecting the light rays. This light then passes through a vertical knife-edge, blocking unrefracted background light showing the variation and gradients in the camera. This allows for the tracking of combustion phenomena, cellular instabilities, and flame propagation speeds. The schlieren videos are recorded using a Photron SA5 high-speed camera operating at a frame rate of 50,000 frames per second (fps), ensuring a high temporal resolution needed for image processing.

Transient in-cylinder pressure traces are measured using a Kistler 601CAA piezoelectric transducer mounted directly to the combustion chamber, exposed to the gas. The generated signal is then transmitted to a Kistler 5018 charge amplifier. The range of the amplifier is set to 250 bar, a sensitivity point of -38.13 pC/bar, a time response of 10 s, and signal output voltage of 25 bar/V.

The voltage output from the charge amplifier is digitized by the Picoscope data acquisition system. The DAQ simultaneously records the laser photo diode pulse, the voltage to pressure, and the linear displacements tracking the position of the pistons. This dataset is compiled and post-processed using a custom MATLAB script developed by Andrew Zdanowicz [60]. All traces can be found in Figure 2.7.

To control the spark ignition timing, a pulse/delay generator is used to generate the laser trigger. The generator is continuously monitoring the voltage output from the pressure charge amplifier. Upon detecting a trigger threshold of 0.67 V (corresponding to an in-cylinder pressure of 16.5 bar), the generator executes a delay of 2.5 ms. This timing ensure that the laser fires and deposits energy approximately 1 ms after TDC, isolating the ignition event within a stagnant, quiescent environment. A BNC wiring diagram of this setup can be found in Figure 2.6.

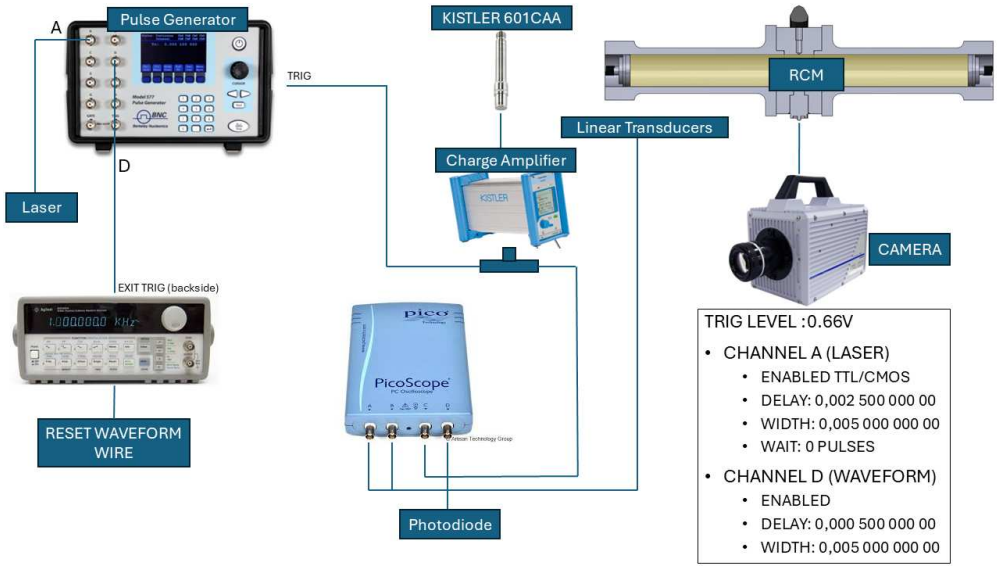

Figure 2.6: BNC wiring diagram of flame speed experiments.

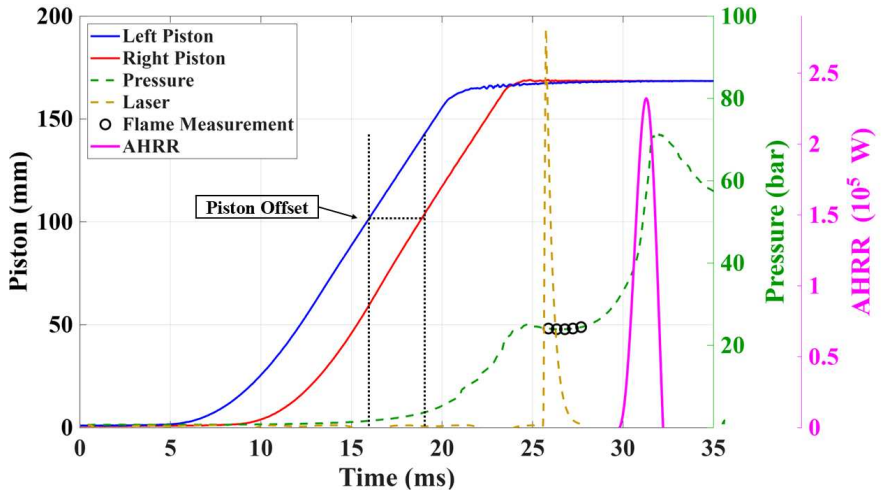

Figure 2.7: Traces from RCM experiments for the pressure, piston location, laser energy, AHRR and location of flame measurement.

Further information on the acquisition system in more detail can be found from Andrew Zdanowicz's thesis [60].

2.4.2 Droplet Generator Hardware

The droplet generator used in this study was originally designed by Siddhesh Bhoite, who first studied the ignition and combustion of hydrocarbon droplets in the RCM [61, 62]. This design utilizes a piezoelectric element (TDK PowerHap haptic actuator) to induce a pulse in the diesel liquid to push a droplet out of a glass blown nozzle. In this study, a 150 micron nozzle was used to push droplets out upon compression. The generator is comprised of the piezoelectric element, a fuel reservoir, fuel passage, cartridge heaters, and the nozzle. As shown in Figure 2.8, the generator has all of these elements, including a threaded element, allowing for fastening onto the RCM chamber.

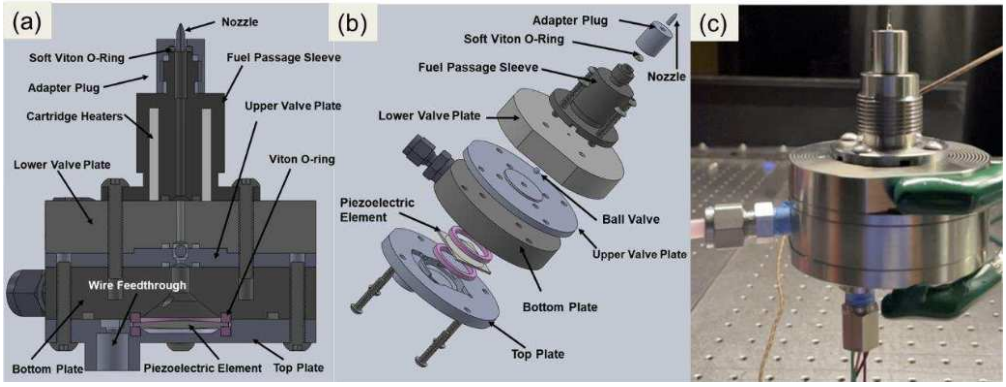

Figure 2.8: Schematic of the droplet generator originally designed by Siddhesh Bhoite. a) represents the solid model, b) the exploded view, and c) photograph of droplet generator. [61, 62]

When attached to the chamber (also designed by Siddhesh Bhoite), the nozzle sits at the bottom of the chamber, with a short amount sticking out, allowing for viewing from the schlieren set up as seen in Figure 2.9. Aside, the exact same schlieren setup used in flame speed measurements (Section 2.4.1) is used in droplet measurements. A BNC diagram of this setup is seen in Figure 2.10.

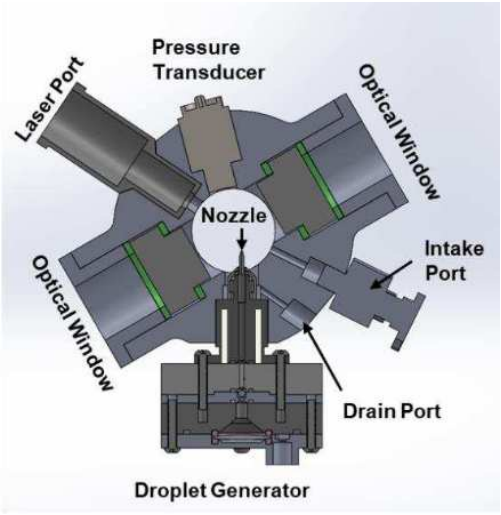

Figure 2.9: Cross-section of the RCM chamber with the attached droplet generator designed by Siddhesh Bhoite [61, 62].

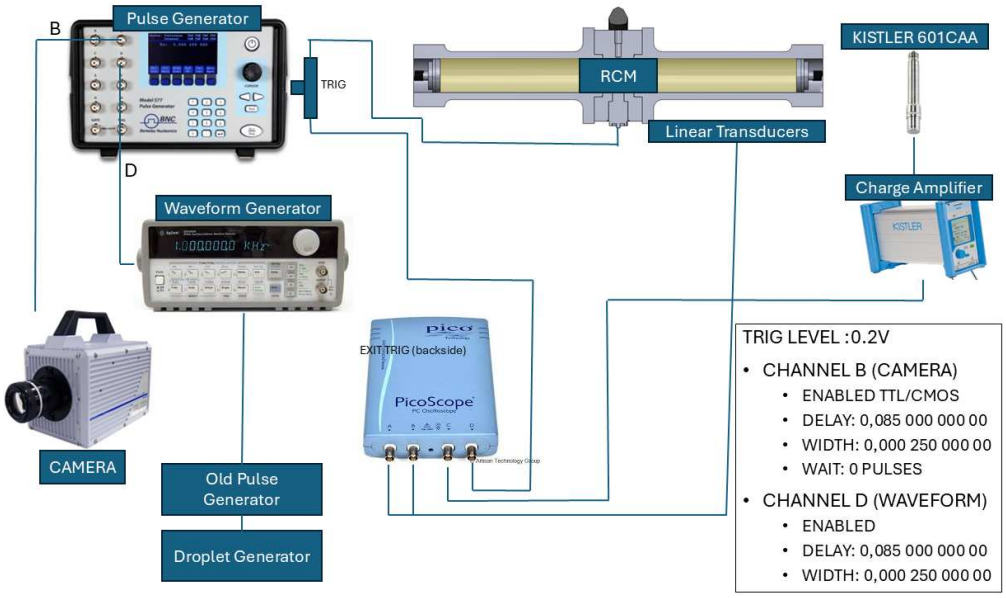

Figure 2.10: BNC wiring diagram of droplet ignition experiments.

More information of the droplet generator setup and data acquisition can be found in Siddhesh Bhoite's dissertation [61].

CHAPTER 3 – EXPERIMENTAL METHODS

This chapter will cover the several experimental methodologies, preliminary calculations, testing matrix, and post-processing employed for both flame speed and droplet ignition experiments.

3.1 Top-Dead-Center Conditions Calculations

Because each test case in the RCM occurs within milliseconds, directly measuring the gas temperature profiles using standard thermocouples is not possible. Consequently, the temperature at top-dead-center (T_{TDC}) must be determined from the measured pressure trace using an isentropic core assumption. Using this, the gas is modeled as an adiabatic process, where the temperature is calculated using Equation 3.1.

$$\frac{\mathrm{T_{TDC}}}{\mathrm{T}_i} = \frac{\mathrm{P_{TDC}}}{\mathrm{P_i}}^{\frac{\gamma-1}{\gamma}} \tag{3.1}$$

T_{TDC} and P_{TDC} represent the compressed temperature and pressure at the end of the compression, T_i and P_i represent the initial recorded temperature and pressure, and γ represents the specific heat capacity ratio of the bulk gas mixture.

Since γ changes with pressure and temperature throughout the compression stroke a constant γ cannot be used. To account for this, the initial pressure/temperature and TDC pressure allow the solution of the TDC temperature assuming frozen chemistry via adiabatic compression in Gaseq [63]. From this, the averaged gamma of both states are used to calculate the TDC temperature for the given mixture.

At elevated pressures, real-gas effects can deviate from the idealized behavior as explained in the previous paragraph, affecting the validity of the isentropic assumption. To evaluate this uncertainty, the compressibility factor (Z) was calculated for the fuel matrix at the highest thermodynamic states of the experimental matrix (T=850 K and 30 bar). For the most non-ideal case - neat ammonia, constituting 21% of the mixture at 0% decomposition - the compressibility factor is approximately 0.990. Given that the bulk of the gas mixture is composed of stable, diatomic

and monoatomic gases (N_2 and Ar), the global compressibility factor is within 1% of unity. Consequently, the ideal gas assumption remains valid and appropriate for the thermodynamic temperatures presented.

It is important to note that the compressed temperature is calculated using the adiabatic core assumption and calculated using isentropic compression, relating the temperature to actual measured pressure during the compression stroke and at TDC. By using the measured dynamic pressure, non-ideal effects like piston blowby and heat transfer, inherent to RCM experiments, are in fact accounted for.

3.2 Decomposition Mixture Calculations

To complete tests, the exact molar fractions of the fuel mixture (NH_3 / H_2 / N_2 / O_2) must be derived using stoichiometry. The global decomposition reactions of a single ammonia atom is a function of the decomposition fraction (%D) according to Equation 3.2.

$$\mathrm{NH_3} \longrightarrow \%\mathrm{D}(\frac{3}{2}\,\mathrm{bH_2} + \frac{1}{2}\,\mathrm{cN_2}) + (1 - \%\mathrm{D})\mathrm{aNH_3} \tag{3.2}$$

Using this, the "fuel" blend is defined as the combination of the uncracked ammonia and cracked nitrogen (N_2) and hydrogen (H_2). Components a, b, and c are the mole fraction concentrations of each of these species. To determine the quantity of oxidizer and nitrogen from air required to achieve a certain equivalence ratio (ϕ), the global combustion reaction assuming complete combustion with ideal products (H_2O/N_2), using Equations 3.3 and 3.4.

$$(\mathrm{aNH_3} + \mathrm{bH_2} + \mathrm{cN_2}) + \mathrm{d}(\mathrm{O_2} + 3.76\,\mathrm{N_2}) \longrightarrow \mathrm{eN_2} + \mathrm{fH_2O} \tag{3.3}$$

$$f = \frac{3a + 2b}{2}, \quad d = \frac{f}{2\phi}, \quad e = \frac{a + 2c}{2} + 3.76d \tag{3.4}$$

By completing balances across the species, the final reaction coefficients (mainly d) can be solved for. This derivation provides the calculation needed for exact partial pressures required

during the filling of the mixing tank, as explained in Section 2.3. It is important to note that in real-world decomposition, radicals and intermediates such as NH_2 or NH - to name a few - are highly reactive and are usually created as a part of the process. Therefore, the fuel used in this study is a perfect case point for fundamental kinetic modeling.

3.3 Ammonia-Diesel Equivalence Ratio Calculation

To ensure that the RCM droplet ignition experiments match real-world dual-fuel compression-ignited operation, the fuel ratio was determined based on the specifications of a heavy-duty John Deere PowerTech PWL 4.5L engine, planned to run with on-board catalytic ammonia reforming. The relevant operating specifications can be found in Table 3.1.

Table 3.1: John Deere PowerTech PWL 4.5L Engine and Fuel Specifications.

Operating Conditions				
T_{in} (°C)	P_{in} (kPa)	$\dot{m}_{air}$ (kg/hr)	$\dot{V}_{air}$ (m^3/min)	A/F Ratio
25	99	7.3	500	29.9:1
Fuel and Mixture Properties				
Component	Energy Fraction	LHV (MJ/kg)	Density (kg/m^3)	
Ammonia (NH_3)	0.95	18.6	0.681	
Diesel	0.05	42.5	850	
Air	–	–	1.157	

According the specification sheet under standard load conditions, the engine uses a baseline intake air mass flow rate ($\dot{m}_{air}$) of 500 kg/hr at an air-to-fuel ratio (A/F) of 29.9:1. For pure diesel operation, this is a baseline fuel mass flow of 16.722 kg/hr ($\dot{m}_{baseline,fuel}$). The total energy input rate ($\dot{Q}$) required by the engine is then calculated by scaling the baseline fuel mass flow with the lower heating value (LHV) of the diesel fuel, which comes out to be 710 MJ/hr, by using Equation 3.5.

$$\dot{Q}_{min,fuel} = \dot{m}_{fuel} * LHV_{diesel} \tag{3.5}$$

Using previous experimental ammonia/diesel work [14, 19], a 95%/5% ammonia to diesel energy ratio is implemented. The energy rate for both ammonia and diesel is calculated using this ratio and the minimum $\dot{Q}_{min}$ calculated earlier using Equation 3.6. Than by using the LHV of ammonia, the mass flow rate of ammonia can be solved using Equation 3.5.

$$\dot{Q}_{\mathrm{NH_3}} = 0.95\ \dot{Q}_{min,fuel} \quad \dot{Q}_{\mathrm{diesel}} = 0.05\ \dot{Q}_{min,fuel} \tag{3.6}$$

Because dual-fuel engine setups intake the gaseous fuel through the intake manifold, the incoming gas is mixed with the portion of air drawn into the cylinders. To determine the final in-cylinder equivalence ratio, the mass flow rates must be converted into their respective volumetric flow rates ($\dot{V}$) using the ideal gas equation to solve for the relative density of the air and fuel mixture at the inlet conditions ($T_{in} = 25°C$ and $P_{in} = 99kPa$). At these initial states the densities of both ammonia and air are $\rho_{air} = 1.157\ kg/m^3$ and $\rho_{NH3} = 0.681\ kg/m^3$.

Now the baseline total intake volumetric flow can be solved using the baseline air mass flow and the calculated density of air, using Equation 3.7 gives a total volumetric flow of $432.15\ m^3/kg$. Similarly using the mass flow of ammonia and density of ammonia, the volumetric flow comes to be $53.38\ m^3/kg$. Now, by subtracting the total, baseline volumetric flow from the calculated flow of ammonia, the actual volumetric flow of air comes out to be $378.775\ m^3/kg$.

$$\dot{V} = \frac{\dot{m}}{\rho} \tag{3.7}$$

Consequently, the operating reactant A/F ratios of the gaseous in-cylinder mixture without diesel is 7.096 based on the volumetric rates. To translate this A/F ratio to the equivalence ratio needed for RCM testing, the global A/F ratio of pure ammonia is needed. For complete combustion of neat ammonia in air, the A/F ratio is 3.57. Using Equation 3.8, the equivalence ratio is ~ 0.5, based on molar value. Consequently, all dual-fuel diesel droplet ignition experiments conducted in the RCM were maintained at an equivalence ratio of 0.5, no matter the decomposition fraction.

$$\phi = \frac{(A/F)_{stoich}}{(A/F)_r} \tag{3.8}$$

3.4 Testing Matrix

3.4.1 Flame Speed Mixtures

To understand the impact increased concentrations of H_2 and N_2 have on flame speeds and the chemical kinetics, four different decomposition percentages were chosen: 0, 10, 20, and 42.5%. All mixtures were evaluated at a stoichiometric equivalence ratio ($\phi = 1.0$). The 42.5% decomposition case was determined through preliminary Cantera simulations, which indicated that this decomposition percentage is required to obtain flame speeds comparable to that of a baseline methane (CH_4) at identical thermodynamic conditions, as seen in Figure 3.1.

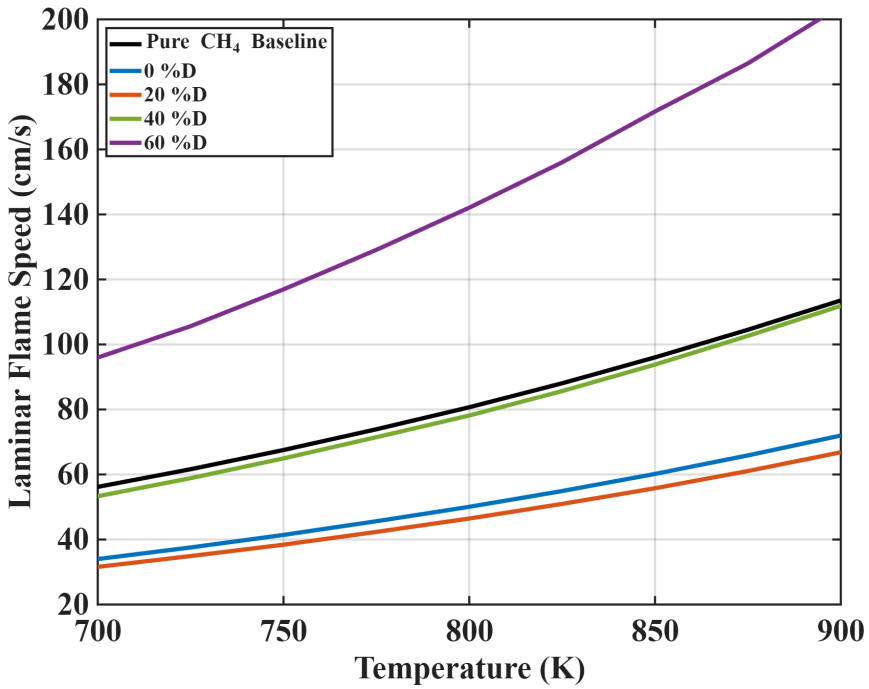

Figure 3.1: Laminar flame speed simulations of a range of decomposed ammonia mixtures compared to methane using the NUIG [64] and C3 [65] mechanisms.

Utilizing the previous derivation in Section 3.2, the molar fractions for each mixture were solved. The resulting concentrations are seen in Table 3.2. In addition, all inert diluent ratios were

kept at a ratio of 75%/25% Ar/N_2 in order to raise the compressed temperature, needed to reach >750 K.

Table 3.2: Experimental test matrix for flame speed measurements with each species mole fraction. A 75%/25% Ar/N_2 inert ratio was used for each case.

Mixture	NH_3	H_2	$N_{2decomp}$	O_2	N_{2air}	Ar	CH_4
0% D	0.2188	0.0000	0.0000	0.1641	0.1543	0.4628	–
10% D	0.1927	0.0321	0.0107	0.1606	0.1510	0.4529	–
20% D	0.1677	0.0629	0.0210	0.1572	0.1478	0.4434	–
42.5% D	0.1151	0.1276	0.0425	0.1502	0.1411	0.4234	–
CH_4 Baseline	–	–	–	0.1900	0.1787	0.5362	0.0950

To simulate engine-relevant conditions while targeting gaps in literature, compressed pressures of 20, 25, and 30 bar and temperatures ranging from 760–850 K were chosen. Because of the changing concentrations of H_2, N_2, and Ar across the range of decomposition percentage the initial temperature and pressure needed to be adjusted case-by-case to yield the same compressed conditions. For 0, 10, and 20% decomposition cases initial temperatures of 25, 40, and 60°C were used for TDC temperatures of 760, 800, and 840 K, respectively. For the 42.5%D cases, an initial temperature of 35 and 50°C and 25 and 35°C for CH_4 were used to obtain the final two TDC temperatures similar to the lower decomposition percentages. Initial pressures for all mixtures were at 1 bar, with it decreasing to 0.9 bar for the methane cases.

The 42.5% decomposition mixture was chosen as a comparator to methane as illustrated by the Cantera 1-D simulation in Figure 3.1. Initial simulation sweeps found that at a 40% decomposition gave similar ammonia flame speeds to the baseline methane data. However, when simulating smaller decomposition increments, 42.5% decomposition provided the most optimal match the the methane standard.

By testing this decomposition percentage with pure methane in the RCM, transport and cellular instabilities of hydrogen-rich ammonia blends show deviation from the traditional hydrocarbons at identical thermodynamic properties.

3.4.2 Diesel Droplet Ignition Mixtures

Similar to the approach for the fundamental flame speed matrix, three ammonia decomposition percentages were chosen to investigate the ignition chemistry of a liquid diesel droplet. Leveraging off the derivation of the equivalence ratio $\phi = 0.5$ calculated in Section 3.3, and the decomposition derivation in Section 3.2, ammonia decomposition percentages of 0%, 20%, and 40% were selected. These specific values were chosen as these are expected from the on-board reformer on the John Deere engine. Certified XU grade #2 ultra low sulfur diesel was used in testing, the same diesel used in the John Deere engine.

To expand on the dataset and chemical kinetics, comparative tests were executed with pure hydrogen at equivalence ratios of $\phi = 0.4$ and $\phi = 0.5$. All mixtures and corresponding mole fractions are organized in Table 3.3. To obtain the high temperatures, a 100% Ar dilution was used for ammonia mixtures, whereas a 90/10 Ar/N_2 was used for hydrogen tests.

Table 3.3: Experimental test matrix for NH_3/Diesel and H_2/Diesel showing species mole fractions (X_i). Decomposed ammonia cases have 100% Ar dilution and are at $\phi = 0.5$, H_2 mixtures are all at a 90/10 Ar/N_2 dilution at $\phi = 0.4, 0.5$.

Mixture	NH_3	H_2	$N_{2\text{decomp}}$	O_2	$N_{2\text{air}}$	Ar	CH_4
0% D	0.1229	0.0000	0.0000	0.1843	0	0.6929	–
20% D	0.0959	0.0360	0.0120	0.1799	0	0.6763	–
40% D	0.0703	0.0703	0.0234	0.1756	0	0.6604	–
H_2 $\phi = 0.4$	0	0.1438	0	0.1798	0.0676	0.6087	–
H_2 $\phi = 0.5$	0	0.1736	0	0.1736	0.0653	0.5876	–

When evaluating the ignition behavior across the fuel configurations, the variation in oxygen concentration must be taken into account. Because the chemical interactions that initiate droplet ignition are governed by the radicals generated between the vaporized liquid diesel and oxidizer, the available oxygen is expected to represent the main driver for the ignition delay time.

3.5 Flame Speed Measurements

Experimental measurements of flame speeds are generally completed using two methods: constant-pressure or constant-volume. In this study, a constant-volume approach is employed as the RCM pistons remain locked at TDC following the compression stroke and the volume remains constant during flame propagation.

The temporal flame propagation is characterized using an in-house MATLAB image processing code developed by Andrew Zdanowicz [60]. This script applies edge-detection to follow the flame front in the high-speed schlieren images, tracking the instantaneous, time-dependent flame radius (r_f). The initial window size is used as the baseline, measuring the radius, in pixels, from the area of the circle which is used as the baseline. From there, the code uses filtering and edge detection to find the flame surface, converting that area to a subsequent radius, as apparent in Figure 3.2, giving the instantaneous, time-dependent flame radius.

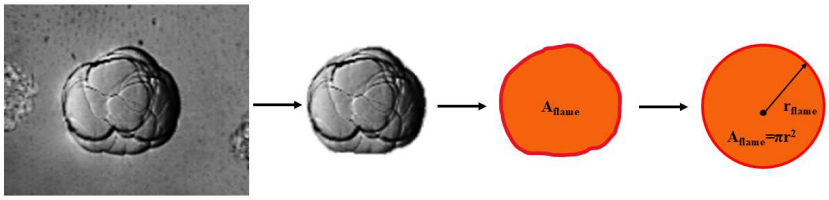

Figure 3.2: Visualization of edge detection and the measurement process associated with determining the flame radius.

During image post-processing, the measured flame radius can have rapid changes due to edge-detection, leading to sharp spikes in the radius calculation. As the flame speed is derived from the first derivative of the radius, these sharp increases and decreases present errors in the flame speed calculation. To mitigate this sensitivity, the original raw propagation rate is filtered, removing the points where large spikes are seen. After, the filtered points are fit to a second-order polynomial. An example of this time-dependent flame radius is illustrated in Figure 3.3.

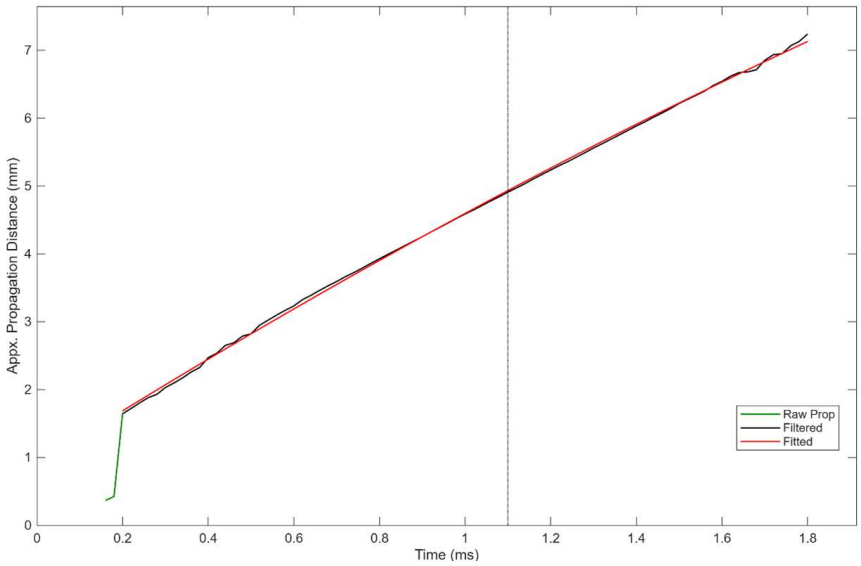

Figure 3.3: Example of measured time-dependent radius of a spherically propagating flame using MATLAB edge detection. The green or 'Raw Prop' line represents the raw radius, these values are than filtered (black line), removing points that have a sudden change in slope. These values are than fitted to a second-order polynomial (red line). This example is for a 20% decomposition at 840 K and 25 bar.

To isolate the chemical propagation from ignition artifacts apparent in the initial flame kernel, data collection begins 0.2 ms post-laser spark. This delay allows for the kernel to expand to a point where the flame turns from a spark-dominated plasma flame to a self-sustaining and chemically driven flame front. To ensure the validity of the laminar assumption, measurements are terminated at the onset of significant pressure rise at the piston walls. As the flame front approaches the borders of the volume, wall heat transfer and interaction with the cold boundary layer distorts the flame front, making it unrepresentative of fundamental fuel reactivity. The flame measurement location regarding the pressure trace is illustrated in Figure 2.7.

A propagating spherical flame in an RCM is fundamentally different from the 1-D flat flame defined in theoretical chemistry. Because the spherical flame is curved and the flow field is diverging outward, the flame is subject to "stretch." Stretch can either accelerate or decelerate the flame depending on the mixture's Lewis number and flame front thickness. To find the fundamental property of the fuel mixture, stretch must be accounted for by extrapolating the measured burned gas speed (S_b) to a state of "zero-stretch" flame (S_b^0). In this study, the zero-stretch burned flame

speed is determined using the non-linear Kelley extrapolation method [66]. As shown in Equation 3.9, this equation accounts for the non-linear effects of curvature and strain on the flame front.

$$S_b = S_b^0 + cr_f + 2L_b \ln(r_f) - 4\frac{L_b^2}{r_f} - \frac{8}{3}\frac{L_b^3}{r_f} \tag{3.9}$$

Where L_b represents the Markstein length, which characterizes the flame's sensitivity to stretch and c represents a coefficient. An example of this method and subsequent plot can be seen in Figure 3.4.

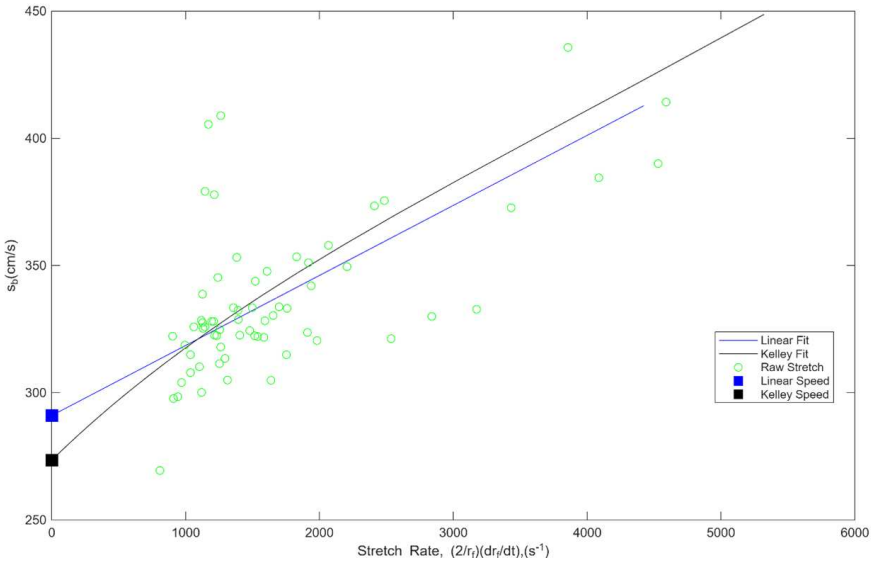

Figure 3.4: Example of stretch rate plot where the green dots represent the raw stretch values between each point, the blue represents the linear fit, and black represents the non-linear Kelley extrapolation method. This example is for a 20% decomposition at 840 K and 25 bar, the same example shown in Figure 3.3.

While the Kelley method yields the speed at which the burned gases expand (S_b^0), the standard value in combustion science is the unburned laminar flame speed (S_u or S_L). This is the speed at which the unburned reactant mixture is consumed by the flame front. For a stationary flame, such as that produced by a Bunsen burner, the unburned gas velocity exactly matches the laminar flame speed, resulting in a stable flame. In this propagating spherical system, the expansion of the hot, lower-density burned gases pushes the flame front outward at a much higher velocity than the rate of consumption. To return to the fundamental unstretched laminar flame speeds, correction of the

zero-stretch burned speed is done using the burned-to-unburned density ratio (ρ_b/ρ_u) as shown in Equation 3.10.

$$S_b^0 = S_b \left(\frac{\rho_b}{\rho_u} \right) \tag{3.10}$$

The density ratios for each mixture were computed via calculations in Cantera [67] using the NUIG chemical kinetic mechanism [64].

3.6 Diesel Droplet Ignition Measurements

Ignition delay time is defined as the time it takes a fuel mixture to ignite, where the time frame is from top-dead-center (TDC) to the highest rate of pressure rise when ignition occurs. This is the classical term of ignition delay time, but in droplet ignition, the time frame, instead of relying on the pressure trace, relies on the high-speed schlieren imaging. The droplet ignition time is measured from TDC to the exact point where the droplet begins to ignite and propagate the flame. If the droplet that ignites comes out after TDC, this is the starting point for measurement. This process is illustrated in Figure 3.5, highlighting the key locations within diesel droplet measurements.

To determine the size of the droplet, it is measured using the ImageJ software [68]. The diameter of the window is measured using the line and measure functions in ImageJ. Using the actual diameter of the window (26.67 mm or 26670 μm), a scaling factor is calculated, giving a μm/pixel value. Based on the pixel area of the droplet after it exits the nozzle, the diameter of the droplet can be measured. The average diameter of the windows is 300 pixels, giving a scaling factor of $\sim$88 μm/pixel, used to calculate the diameter of the droplet.

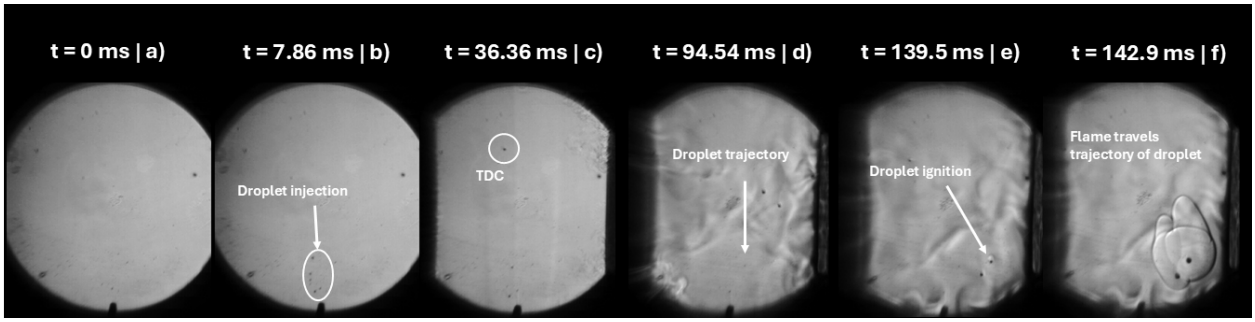

Figure 3.5: Process taken into measuring the droplet ignition delay time where a) represents the start of the video, b) shows the injection of the droplets, c) shows where the droplet may be at top-dead-center (where measurement begins), d) shows where the droplet trajectory between TDC and ignition, e) presents the droplet ignition point (end of measurement), and finally f) shows the flame morphology.

Figure 3.6 presents a common pressure trace seen in droplet ignition experiments. Similar to what is seen in flame speed measurements (Section 3.5) the pressure and piston locations are measured as a function of time. The yellow line represents the voltage associated with the piezoelectric element where the droplet is fired into the chamber. The dotted lines represent the ignition delay time of the droplet in this specific experiment. As explained previously, measurement begins at TDC, or the time at which the droplet leaves the nozzle, till the time at which the droplet ignites.

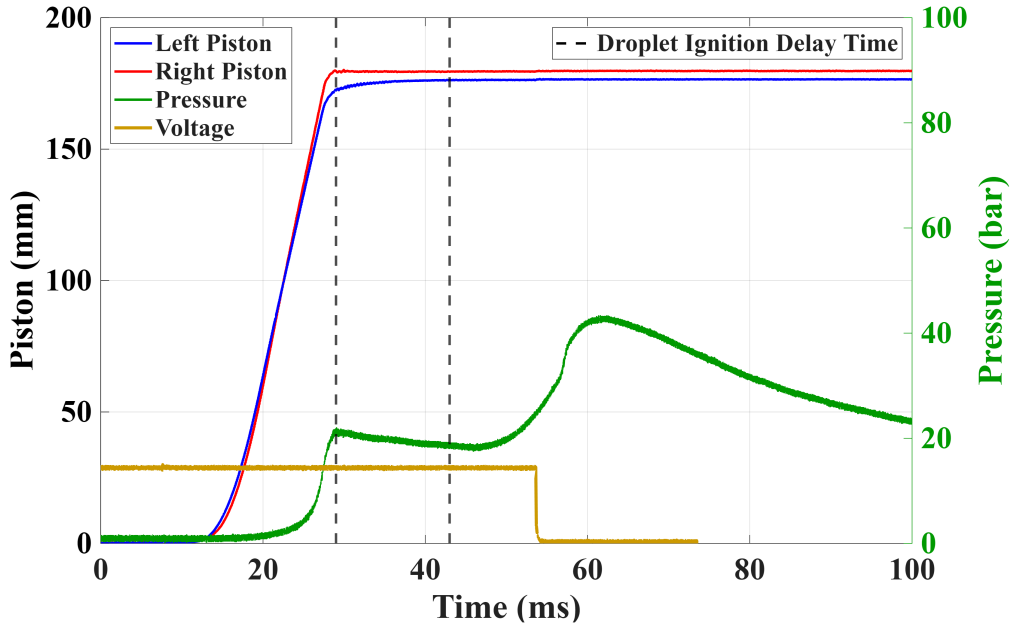

Figure 3.6: Example of a common pressure trace seen in droplet experiments. The mixture is a 40% decomposition with diesel ignition. The dotted lines signify the ignition delay time associated when the droplet ignites in the mixture.

3.7 Apparent Heat Release Rate (AHRR)

The heat release rate describes the rate at which chemical energy is converted into thermal energy, providing a description of the rate of combustion. In the RCM, the heat release rate determines how fast the pressure in the system rises, directly dictating the work done on the piston and chamber. Because this phenomenon cannot be directly measured due to the individual elementary reactions occurring in the flame zone, the apparent heat release rate (AHRR) must be back-calculated. This is solved by evaluating the experimental pressure trace.

Following TDC and subsequent flame propagation, the RCM is treated as a constant-volume reactor, allowing the AHRR to be calculated using Equation 3.11 where *V* represents the volume at TDC and *dP/dt* represents the time derivative of pressure.

$$AHRR_{CV} = \frac{1}{\gamma - 1} V \frac{dP}{dt} \tag{3.11}$$

Since it is difficult to measure the volume at TDC manually - such as using water or oil to fill the chamber and measure the amount of liquid - the volume was determined using the direct geometry of the chamber at TDC from 3-D CONVERGE ($V = 3.16 * 10^{-5}\ m^3$).

Prior to computing the pressure gradient, the voltage signal from the pressure transducer must be passed through. Due to electrical noise, vibrations, and acoustics in the chamber, the raw pressure traces exhibit small inflections. If not passed through, the calculated AHRR curve will exhibit oscillations which could be misidentified as different combustion events, such as pre-ignition or autoignition. For this reason, a low-pass fast Fourier transform with a 700 Hz cutoff is applied to smooth the pressure trace before calculation.

Because the gas temperature rises rapidly from the flame, the specific heat ratio (γ) must be determined at each time step, rather than a single value. The bulk gas temperature is first computed through the smoothed pressure trace using the ideal gas equation. This temperature is then used to calculate the the mixture specific heat ($c_{p,mix}$), based on the mole fractions of the given mix-

ture. The individual specific for each species are computed using the NASA 5-polynomials [69], allowing the mixture specific heat ratio to be computer at each time step using Equation 3.12.

$$\gamma = \frac{c_{p,mix}}{c_{p,mix} - R_{univ}} \tag{3.12}$$

An example profile of the evaluation of the AHRR with its corresponding pressure trace can be seen in Figure 3.7. The maximum AHRR aligns with the inflection point of the pressure trace, following the trend seen in Equation 3.11. Minor peaks and dips before and after the location of primary heat release are artifacts of the piezoelectric transducer. Even with the integration of the fast Fourier transform, pressure jumps are still apparent.

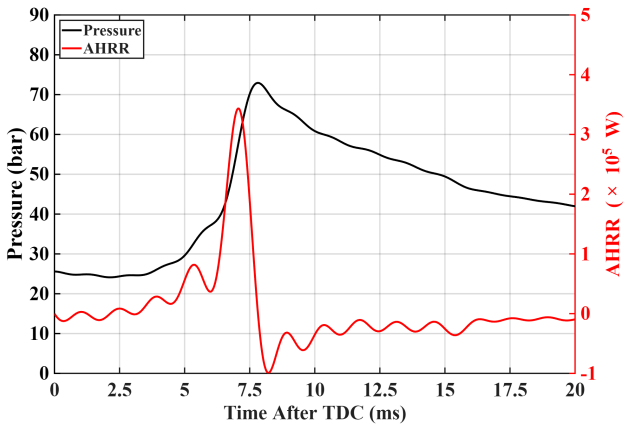

Figure 3.7: Example of the apparent heat release rate (AHRR) calculated using the measured pressure trace.

3.8 Effective Lewis Number

The Lewis Number is a dimensionless parameter, representing the ratio of thermal diffusivity (α) to mass diffusivity (D) which characterizes the thermal boundary layer to the species boundary layer within fluid flow (Equation 3.13). In combustion and flames, it relates the thermal diffusivity of the mixture to the mass diffusivity of the deficient reactant (the species that is not in excess based on stoichiometry).

This parameter dictates how flames behave under stretch, turbulence, and curvature. Premixed flames with a $Le > 1$ are thermodiffusively stable where perturbations in the flame front are damp-

ened by the thermal output. Whereas, flames with a $Le < 1$ are thermodiffusively unstable, meaning the mass diffusion is faster than the output of thermal energy. This energy imbalance wrinkles the flame front, generating cellular instabilities that expand the surface area and accelerates the velocity.

$$Le = \frac{\alpha}{D} \tag{3.13}$$

Neat ammonia is generally considered a thermodiffusively neutral fuel with a Lewis number close to unity, where as hydrogen exhibits a Lewis number of around 0.3. Because of its small molecular mass and kinetic diameter, hydrogen possesses a large mass diffusion coefficient (D) relative to other species. Because of this, the elevated mass transport gives a lower Lewis number than unity, introducing cellular instabilities.

In theoretical analysis of the Lewis number, the reactants in the mixture are assumed to be scarce compared to the inert, allowing species transport to be modeled by standard binary diffusion using Fick's law for binary mixtures. However, in this study because of the amount of fuel and oxidizer species within the non-ideal binary blend of nitrogen or argon, the diffusivity coefficient of the global mixture must be evaluated for each individual reactant all diffusing into the inert gases.

To do this, the thermal diffusivity (α) of the N_2/Ar mixture is calculated based on the thermal conductivity, density, and specific heat at the given TDC temperatures and pressures as shown in Equation 3.14. To obtain the binary diffusion constants, for each reactant the averaged diffusion constant is found using Equation 3.15 where r represents the reactant and X represent the relative mole fraction of the N_2/Ar mixture. In this study the reactants are (r); NH_3, H_2, O_2.

$$\alpha = \frac{\lambda}{\rho c_p} \tag{3.14}$$

$$D_{r,(Ar/N2)} = \frac{X_{Ar} D_{r,Ar} + X_{N2} D_{r,N2}}{X_{inert,tot}} \tag{3.15}$$

Because this flame front involves the diffusion of multiple fuels and oxidizer molecules, the global reaction zone cannot be characterized by a single individual species. Instead, the global transport needs to be characterized by the effective Lewis number (Le_{eff}), comprised of two Lewis numbers. One representing the excess reactant (Le_E) and the other representing the deficient reactant (Le_D). Following the formula created by Addobbo et al. [70], the effective Lewis number can be solved using Equation 3.16.

$$Le_{eff} = 1 + \frac{(Le_E - 1) + (Le_D - 1)A}{1 + A} \tag{3.16}$$

Here, A represents the mixtures strength, scaling the Zeldovich number (Ze), $A = 1 + Ze(\phi - 1)$. If the mixture is rich ($\phi > 1$). the oxidizer is deficient and $\phi = 1$. If the mixture is lean ($\phi < 1$), the fuel is deficient and $\phi = 1/\phi$. At stoichiometric conditions ($\phi = 1$) than A is equal to 1. The Zeldovich number characterizes the activation energy of the reaction front where recent work from Attili et al. [71] simplified the Zeldovich number to $Ze = 4(T_b - T_u)/(T_b - T_0)$. Where T_u and T_b represent the the unburned and burned temperature of the gas and T_0 represents the cross-over temperature. The cross-over temperature represents the point where maximum heat release in the flame is achieved. Using this derivation, the effective Lewis number can be solved with the help of Cantera.

3.9 Laminar Flame Thickness

The laminar flame thickness (δ_L) describes the characteristic length of a premixed combustion flame, representing the spatial distance where chemical and thermodynamic reactions occur. Depending on the pressure, temperature, and fuel reactivity, the flame thickness can span from microns up to $\sim$1 mm.

In conventional hydrocarbon flames the thickness of the reaction zone is primarily measured using the CH radical. However, since ammonia/hydrogen chemistry does not contain carbon, the NH_2 radical is used to track and determine the reaction zone thickness of the flames, following work from Almarzooq et al. [72].

To determine the thickness from 1-D flame speed calculations, the Full Width Half Maximum (FWHM) method is applied to the NH_2 mass fraction. As shown in Figure 3.8, the FWHM method shows the small step at which the NH_2 radical is apparent in the flame front. It then measures the distance between the two points at each side of the peak where the concentration is exactly 50% of the maximum value.

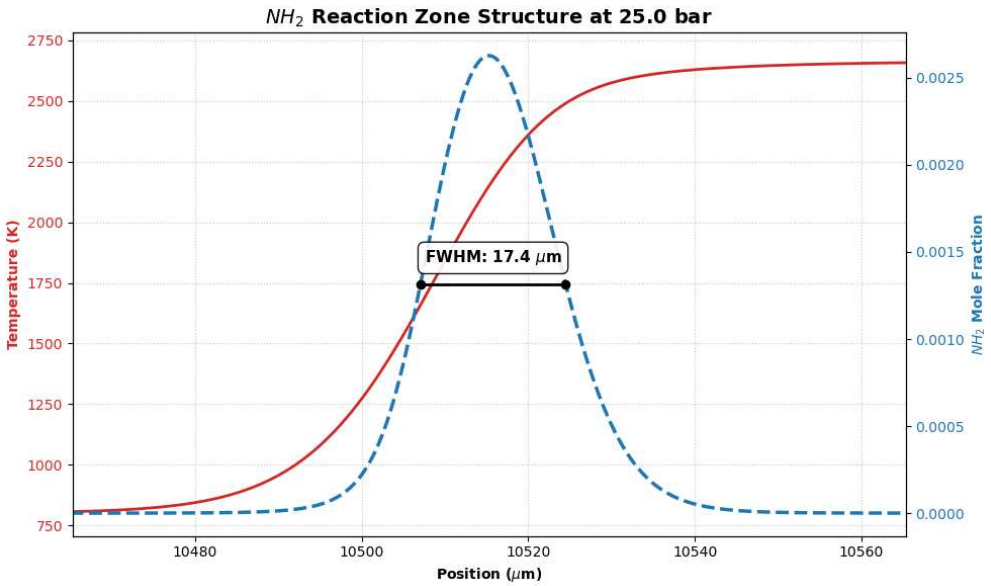

Figure 3.8: Example of the flame thickness of a 20%D flame at 800 K and 25 bar using the FWHM method and the NH_2 radical.

CHAPTER 4 – NUMERICAL/COMPUTATIONAL METHODS

This chapter will cover the entire numerical setup including 1-D and 3-D CFD simulations.

4.1 1-Dimensional Simulations

The fundamental laminar flame speed is an integral fundamental parameter in combustion science, defined as the velocity at which a steady, one-dimensional, adiabatic flame front propagates into an unreacted, quiescent reactant mixture. To establish benchmarks for comparison against the experimental dataset, 1-D planar flame simulations were executed using Cantera.

All simulations were performed using Cantera's FreeFlame model [67]. To resolve the species and temperature gradients within the reaction zone, grid refinement was used. The slope and curve parameters were both set to a threshold of 0.01, paired with a grid refinement ratio of 3. Setting the slope and curve parameters to these values ensures that the locations at which the temperature or species mass fraction experiences large changes is refined. This refinement is necessary for capturing the boundaries of these thin ammonia/hydrogen flames. The resulting values had highly resolved meshes ranging from 900 to 1,200 grid points, where solution time ranges from 3–10 minutes.

In 1-D combustion modeling, accurately modeling species transport is necessary, particularly when using fuel blends with smaller species like hydrogen. With current numerical models, there are three governing ways to model species mass diffusion being single-species transport, mixture-averaged transport, and finally multicomponent transport.

Single-species diffusion, the simplest approach, assumes that the mass diffusion coefficient (D_i) of species i scales across the entire mixture at a constant rate, regardless of other species present. This model is typically facilitated with a constant Lewis number.

Mixture-averaged is the standard and most commonly used transport model in multi-dimensional engine CFD models to optimize the computational speed without affecting accuracy. This method calculates a diffusion coefficient for species i into the remaining mixture, by considering its binary

interactions with all other individual species, j. Subsequently, all the diffusion coefficients are averaged into a single value treating the mixture as a single averaged medium.

Finally, multicomponent diffusion is the most accurate representation of molecular transport amongst the three, but also the most computationally expensive. Instead of averaging the species of i into j, it takes every i against j, and in turn gives a specific diffusion coefficient. Due to this, multicomponent transport is best for high pressure environments and mixtures containing light species like H_2 and He. Given that hydrogen diffusion primarily dictates the propagation speed of the decomposed ammonia blends, the multicomponent transport was implemented in all 1-D Cantera simulations.

To complement multicomponent diffusion, the Soret effect was added to the framework to model the diffusion of hydrogen. The Soret effect is where a high temperature gradient drives a concentration gradient in the specie, regardless of the gradient already existing. Within a propagating flame, the gas experiences high temperature gradients where different molecules react differently based on their molecular weight and other factors. Light and highly diffusive molecules like hydrogen, are driven by these thermal diffusion from the cold areas to the high-temperature reaction zone. In traditional hydrocarbon chemistry, the Soret effect is frequently omitted or negligible because these heavier molecules are insensitive to the effects of the thermal gradients. However, for mixtures containing hydrogen, ignoring this effect can lead to error in calculated flame speeds.

Consequently, to ensure fidelity amongst all simulations and to capture all transport, both multicomponent and the Soret effect were used.

4.1.1 Mechanisms Used

Chemical kinetic mechanisms provide a description of the pathways a chemical species takes throughout the combustion process. Rather than relying on single-step global reactions, these mechanisms rely on hundreds of elementary reactions that are classified into: chain-initiation, -branching, -propagating, and -terminating reactions.

Chain-initiation reactions are where a stable molecule undergoes an endothermic reaction, breaking into highly reactive radicals. Chain-branching reactions occur from a collision between

a radical and a reactant molecule, yielding a net increase in radical population. Chain-propagating reactions are where radicals react with a stable species to form new radicals, with a one-to-one exchange. Finally, chain-terminating reactions are where radicals collide with a third-body to re-combine into a stable specie, acting as a sink, decelerating the consumption rate [73].

These reactions interact with one another, governing whether an intermediate specie is created or destroyed at certain conditions. All individual chemical kinetic mechanism are different, varying in their species, elementary reactions, rate coefficients, and overall scale. In order to visualize this, a representative nitrogen-species reaction path diagram for a 20% decomposition ammonia flame at 800 K and 25 bar is shown in Figure 4.1, showing the pathways of the conversion of ammonia to nitrogen.

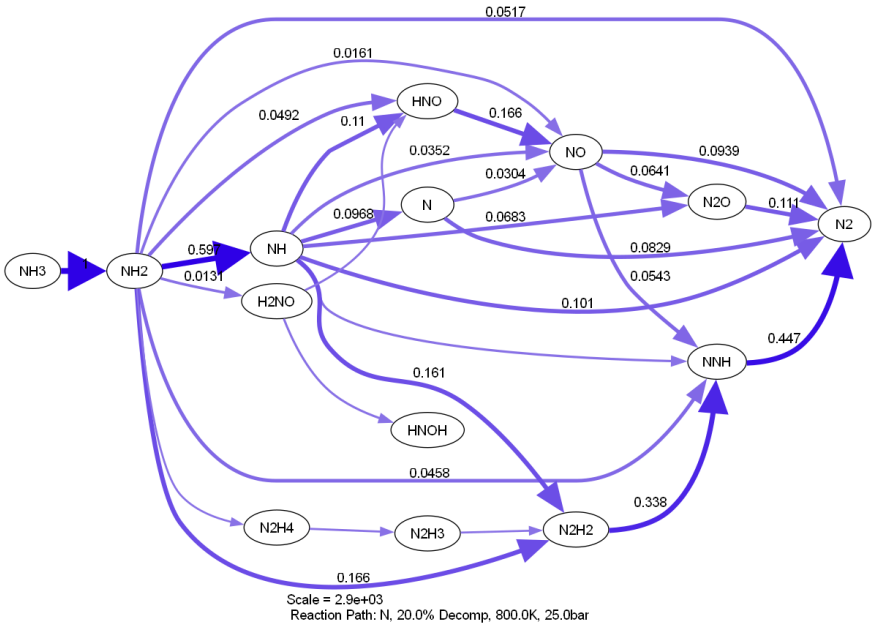

Figure 4.1: Example of nitrogen pathways for a 20%D mixture at 800 k and 25 bar. Computed in Cantera using the NUIG mechanism [64].

The development of mechanisms relies on experimental datasets to fine-tune rate coefficients and thermodynamic properties. The elevated, engine-relevant flame speed data generated in this work provides a critical validation dataset for kineticists to capture the chemistry at these elevated pressure/temperature conditions.

To evaluate the current state of laminar flame speed mechanisms, eight commonly used and accurate flame mechanisms were selected for evaluation of their predictability at these unseen conditions. This selection was based off of recent chemical kinetic work from Girhe et al. [74] and Szanthoffer et al. [75], targeting highly performing mechanisms that were optimized for laminar flame speeds. The mechanisms chosen and tested are compiled in Table 4.1.

Table 4.1: Ammonia-based chemical kinetic mechanisms evaluated in this study. The C3 mechanisms are taken directly from CONVERGE CFD software and the WUT mechanism is specialized for ammonia/diesel mixtures.

Mechanism	Year	Species	Reactions	Reference
NUIG	2024	39	306	[64]
KAUST	2023	32	243	[76]
Glarborg	2023	34	228	[77]
ELTE	2024	32	141	[78]
Mei	2021	25	239	[8]
Han	2024	32	171	[79]
Stagni	2023	31	205	[80]
C3-NH_3	2022	34	242	[65]
C3-CH_4	2022	60	428	[65]
WUT-NH_3 / $nC_{12}H_{26}$	2023	176	2841	[81]

The NUIG, KAUST, Glarborg, ELTE, Mei, Han, and Stagni were the highest rated across the two studies from Girhe et al. and Szanthoffer et al. as they were chosen for this study. The C3 mechanism, a standard in industry and the base mechanism for CFD modeling made and used in CONVERGE was used as a comparison case to existing laminar flame speed mechanisms. Finally, the WUT-2023 mechanism is made specifically for ammonia/diesel chemistry and was only used for the ignition delay and diffusion modeling of ammonia/diesel.

4.2 Ammonia-Diesel Diffusion and Ignition Modeling

Modeling the diffusion of species between a vaporized liquid droplet and premixed ammonia gaseous mixture often necessitates usage of the droplet evaporation theory model. While previous research from Siddhesh Bhoite [61, 82] utilized 3-D droplet evaporation within CONVERGE to measure the ignition delay time, these simulations are computationally expensive and do not directly measure the diffusion between the mixture and diesel. To understand the interactions between the premixed gas mixture and vaporized diesel, the transport and subsequent diffusion was modeled using Cantera 1-D simulations.

It is assumed that the ignition of diesel/premixed fuel is located at stoichiometric conditions where the diffusing diesel vapor and premixed fuel reach an equivalence ratio of 1 ($\phi = 1$). To analyze this reaction area, Cantera's steady-state counter flow diffusion flame was employed, utilizing the WUT-2023 mechanism.

To isolate reacting chemistry from transport, the chemical reactions in the mechanism input files were removed. This was modeled where the premixed fuel oxidizer mixture comes from the right boundary and the diesel vapor comes from the left boundary ($nC_{12}H_{26}$ Vapor <-> NH_3 Mixture).

To ensure a stable and stagnant flow, momentum conservation was applied to each gaseous boundary. An initial mass flow rate of 0.02 kg/s was used for both streams, scaled by the density of each mixture at the conditions seen in experiments (880 K and 20 bar). This ensured that diffusion and mixing was not affected by velocity. The resulting mole fractions and subsequent equivalence ratio were extracted as a function of their spatial location.

Following experimental data, the same thermodynamic properties were used (880 K and 20 bar) and exact initial mole fractions of the premixed fuel/oxidizer mixture, being 0%, 20%, and 40% decomposition at an equivalence ratio of 0.5. The ignition delay time of each spatial point was then measured using 0-D simulations in Cantera using a relative tolerance of 1e-6 and absolute tolerance of 1e-15, measured using the OH radical. Assuming an ample amount of oxygen in the mixture, each of the delay times were calculated.

4.3 3-Dimensional CONVERGE Simulations

Reacting computational fluid dynamics (CFD) models are integral to modern engine design, providing observations and predictions into combustion physics and thermodynamics that are inaccessible via instrumentation or visualization in an engine. The RCM acts as an ideal validation baseline for these numerical tools. Because of its simple geometry and well-known fluid dynamics, it provides an accurate and relevant environment for chemical kinetic mechanism evaluation and tuning.

If a mechanism cannot accurately predict the ignition, flame propagation, and thermodynamics of this controlled, stagnant, and well-understood environment of the RCM, it cannot reliably be used for high-turbulence and unique geometries, as seen in internal combustion engines. These inaccuracies related to predictive modeling of engines could hinder the transition to ammonia-powered systems. This section will cover the design of the physical RCM model as well as the motives and decisions made in the final model.

The computational model was designed using the CONVERGE CFD software version 4.1.2 [83], with data visualization and post-processing done using Ansys EnSight [84]. This model builds upon the previous baseline RCM model from Siddhesh Bhoite [82] and refined by Andrew Zdanowicz [60], using these previous models as a foundation, introducing modifications to geometry and the numerical setup.

4.3.1 Numerical Model

Simulations were run as fully transient, time-based, hydrodynamic solutions of the compressible Navier-Stokes equations. The fluid flow simulations were solved using the Reynolds-Averaged Navier-Stokes (RANS) approach, applying the Renormalization Group (RNG) k-ϵ turbulence model. This turbulence model was selected for its balance between capturing the correct flow field and structure while minimizing computational cost, making it an industry standard for large-engine development. Combustion was simulated using the SAGE Detailed Chemistry Solver.

A primary constraint with modeling combustion in 3-D is the increase in computational cost with the size of the chemical kinetic mechanism. While the full CONVERGE C3 base mechanism contains 16,575 reactions and 3,768 species [65], using this mechanism is unnecessary and too computationally expensive for these 3-D simulations. As a result, chemical kineticists often reduce mechanisms to the bare minimum of needed reactions to balance accuracy and computational resources. Many hydrocarbon mechanisms contain hundreds of species and reactions, however, optimized ammonia mechanisms provide a great alternative for new fuels as they are relatively small.

In this study, two mechanisms were implemented to assess the current numerical framework, RCM geometry, and the mechanisms as a whole. The C3-NH_3 [65] mechanism is comprised of 242 reactions and 34 species, which is specifically optimized for CFD simulations where computational speed is necessary. The second mechanism from Han-2024 [79] is comprised of 171 reactions and 32 species, which is specifically designed for accurate fundamental laminar flame speeds. By comparing these two mechanisms, the current simulations provide a perfect baseline and benchmark between the "CFD-optimized" mechanism and "accurate laminar flame speed" mechanism, quantifying accuracy and computational resources.

4.3.2 Physical Model

Previous simulation setups from Zdanowicz [60] employed a symmetric domain utilizing a 1/8th and 1/4th section domains, which were subsequently mirrored in post-processing. This setup was shown to minimize computational expense and modeling effort. However, for simulations conducted in this study the whole RCM was simulated, as window cavities are accounted for, significantly affecting the compression ratio and flow field, as in previous setups the chamber was treated as a perfect cylinder.

Accurate representations of the volumetric compression ratio and trapped mass are necessary to ensure an accurate computational model. While the design specifications for the RCM is 11.6:1, the actual compression ratio changes due to overhauls, chamber configurations, and fastening. For example, upon rebuild the piston/shaft seals could cause the pistons to extend slightly further, or

less, than previous installations. The seating and torque of chamber fasteners can also affect the compression ratio. Because methods for measuring volume, such as fluid displacement with oil or water are difficult, produce high error, and risk contamination potential, the compression ratio for this model is determined via the CFD model, assuming perfect and correct geometry.

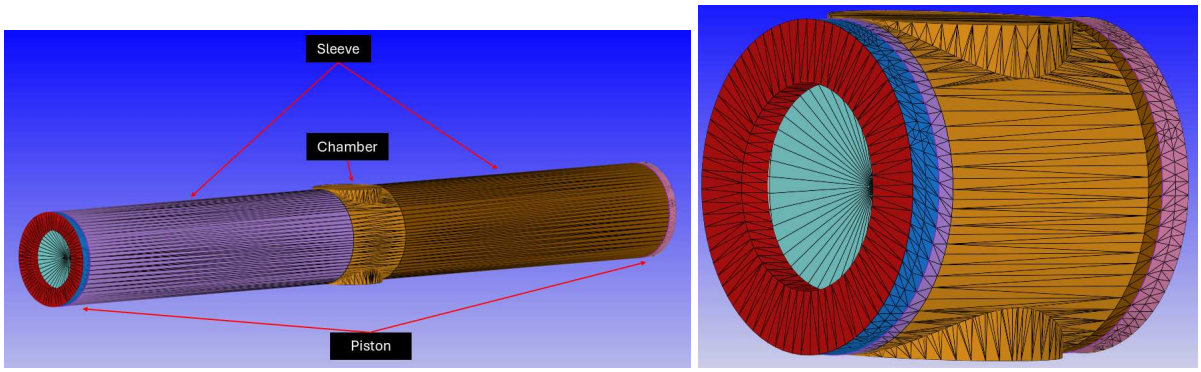

(a) **(b)**

Figure 4.2: Model of the whole RCM where a) shows the entire geometry and b) shows the model compressed at top-dead-center.

As highlighted in Figure 4.2, the model contains the entire chamber, pistons, and sleeves. It also includes the significant dead volume introduced from the optical window cavities. It is known that the dead volumes within the pressure transducer and laser ports likely affect this as well, however, these are much smaller, likely not affecting flow. These will affect the compression ratio, but not affect the flow disturbances as much as the optical window volume. These cavities are the primary source of flow disturbances in the combustion chamber. As the pistons move towards TDC, a portion of the gas is forced into these volumes, generating eddies that may persist into the ignition and flame propagation period.

Quantifying these flows is necessary as failing to model them could lead to an overprediction in the pressure rise and distribution of energy in the reaction zone during flame propagation. Figure 4.3 compares the CFD models window cavities to the actual RCM chamber's dead volume, illustrating the necessity. By including these cavities, the current model gives more insight onto flow

in the chamber and a better representation of the thermodynamics when compared to experimental results.

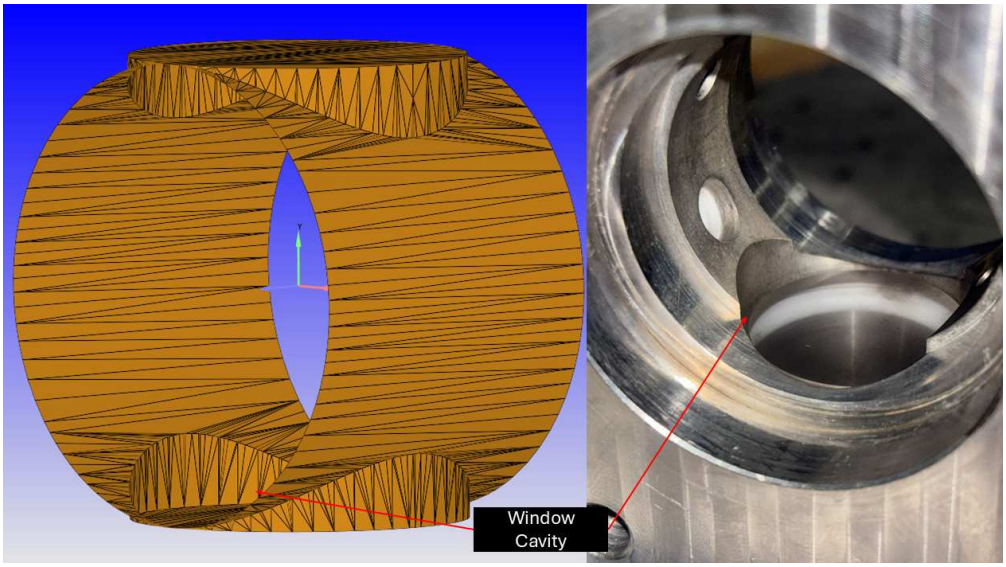

Figure 4.3: Model of the RCM chamber including the window cavities, not modeled in previous studies.

4.3.3 Grid Control

In high-fidelity CFD simulations, computational expense is linked to grid control and the resolution of the mesh. Balancing high-fidelity with computational cost is a challenge to flow and combustion modeling. To balance this, in this work the current simulations use a base grid size of 2 mm supplemented with a combination of Fixed Embedding (FE) and Adaptive Mesh Refinement (AMR). Table 4.2 presents a timing map and parameters implemented to optimize the mesh.

Table 4.2: Adaptive Mesh Refinement (AMR) and Fixed Embedding (FE) timing map for 3-D CFD simulations. Cell size is based on the scale and initial grid size of the simulation. SGC represents the sub-grid criterion.

Location	Embedding Type	Scale	Cell Size (mm)	Time Frame (ms)
Piston Faces	FE	2	0.5	Permanent
Piston Sides	FE	2	0.5	Permanent
Sleeves	FE	2	0.5	Permanent
Initial Kernel (Small Flame)	FE	5	0.0625	22-23
Start of Flame (Medium Flame)	FE	4	0.125	23-24
End of Flame (Large Flame)	FE	3	0.25	24-30
All Cells	AMR - Temperature	3	0.25 (SGC=2.5K)	Permanent
All Cells	AMR - Velocity	3	0.25 (SGC=0.1m/s)	Permanent

Fixed embedding (FE) was applied to regions where the flow field was expected to interact with the boundaries. These boundaries include the piston faces, side crevice volumes, and cylinder sleeves where a scale of 2 was assigned (0.5 mm) to capture the boundary layer interactions. Furthermore, FE was applied to track the flame front. The initial kernel or "small flame" is important and needs high resolution, a scale of 5 (0.0625 mm). As the flame propagates during this initial phase to a spherical radius of 5 mm, this initial propagation rate is important to the the subsequent propagation rates. As the flame radius increases to a "medium flame" (10 mm) and a "large flame" (15 mm), the scales for the fixed embeddings decrease to 4 and 3 (0.125 and 0.25 mm), as the cell count increases and managing high resolution. This fixed embedding was used for the slower flames (0%, 10%, and 20% decomposition), however, the 42.5% decomposition and methane cases exhibit much faster flames. Because of this, only the "medium flame" and "large flame" embeddings were used, set to scales of 5 and 4, respectively. The "medium flame" for these cases ranges from 22-24 ms and the "large flame" ranged from 24-30 ms. Visualization of the fixed embeddings are illustrated in Figure 4.4.

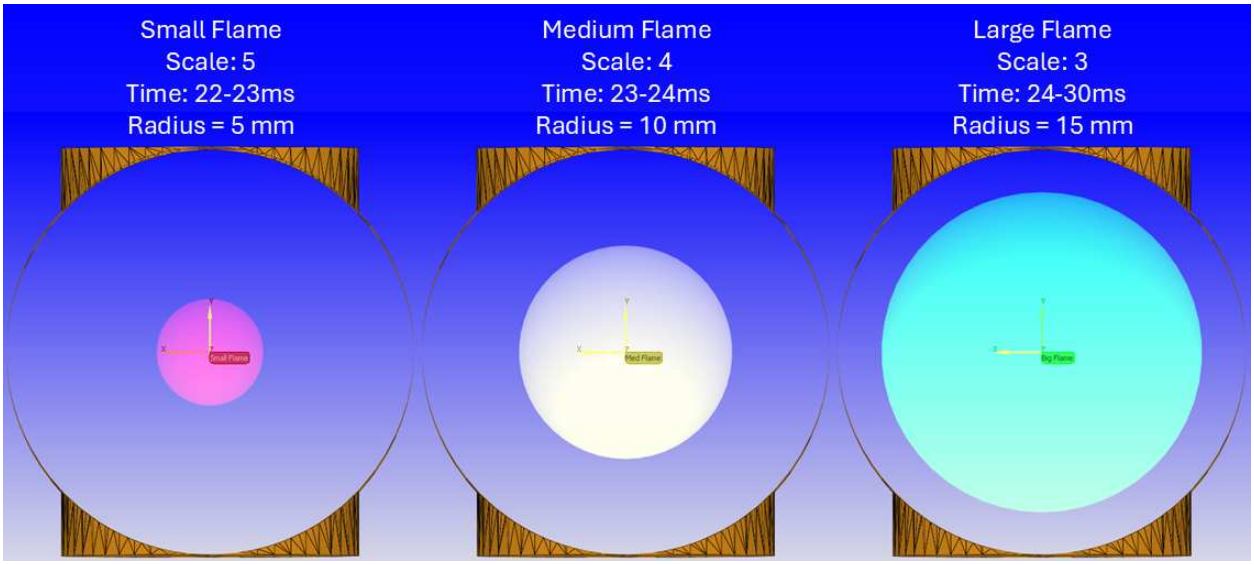

Figure 4.4: Visualization of fixed embedding regions used to refine the flame front in CFD simulations. The times, scales, and sizes shown are used for the 0%, 10%, and 20% decomposition cases. The 42.5% decomposition and methane cases used the "medium flame" and "large flame" at scales of 5 and 4.

Adaptive mesh refinement (AMR) was implemented to help the fixed embeddings refine the grid based on changes in the gas. AMR monitors the gradients of thermodynamic properties, velocity, and species profiles to refine the grid. In this study, the temperature and velocity were monitored. When the gradient reaches a defined sub-grid criterion (SGC), the cell is divided into smaller cells. For temperature, the SGC was set to 2.5 K ensuring the flame front is fully resolved regardless of the position. For velocity, the SGC was set to 0.1 m/s capturing vortex formation and the flow field induced in the piston crevices, window cavities, and the effects of offsets. These SGC values were selected to provide sufficient refinement for flow and thermodynamics without increasing the base grid size. By using both the AMR with the time-dependent FE, the model keeps high-fidelity where it is needed while keeping the remainder of the grid large for computational efficiency.

4.3.4 Preliminary Simulations for Spark Timing and Energy

To simulate the laser spark in CONVERGE CFD, the built-in energy source term was used. Previous simulations from Siddhesh Bhoite [82] found non-spherical flame morphologies from this source term. With subsequent refinement by Andrew Zdanowicz [60], a high-temperature region was introduced in the middle of the chamber volume to initiate ignition. In this study, the original built-in energy source term was optimized and showed circular flame morphology, similar to what was seen in the high-temperature region previously.

Initial simulations used the initial energy-source term parameters (from past models) where the spherical radius was 5 E-05 m, a deposition energy of 30 mJ, and timing of 24-24.25 mJ (3 ms post TDC). Analyzing these simulations revealed that by concentrating 30 mJ of energy into a small volume, the maximum temperature within the ignition kernel reached approximately 30,000 K, as shown in in Figure 4.5 b).

While these extreme temperatures may be apparent in a plasma-induced spark in experiments, this energy created non-uniform flame propagation, affecting the flame front and subsequent flame speed calculations. For reference, Figure 4.5a) presents the final spark compared to this initial

case. The difference in flame morphology is apparent, whereas the resulting heat release rates were shown to have less of an impact.

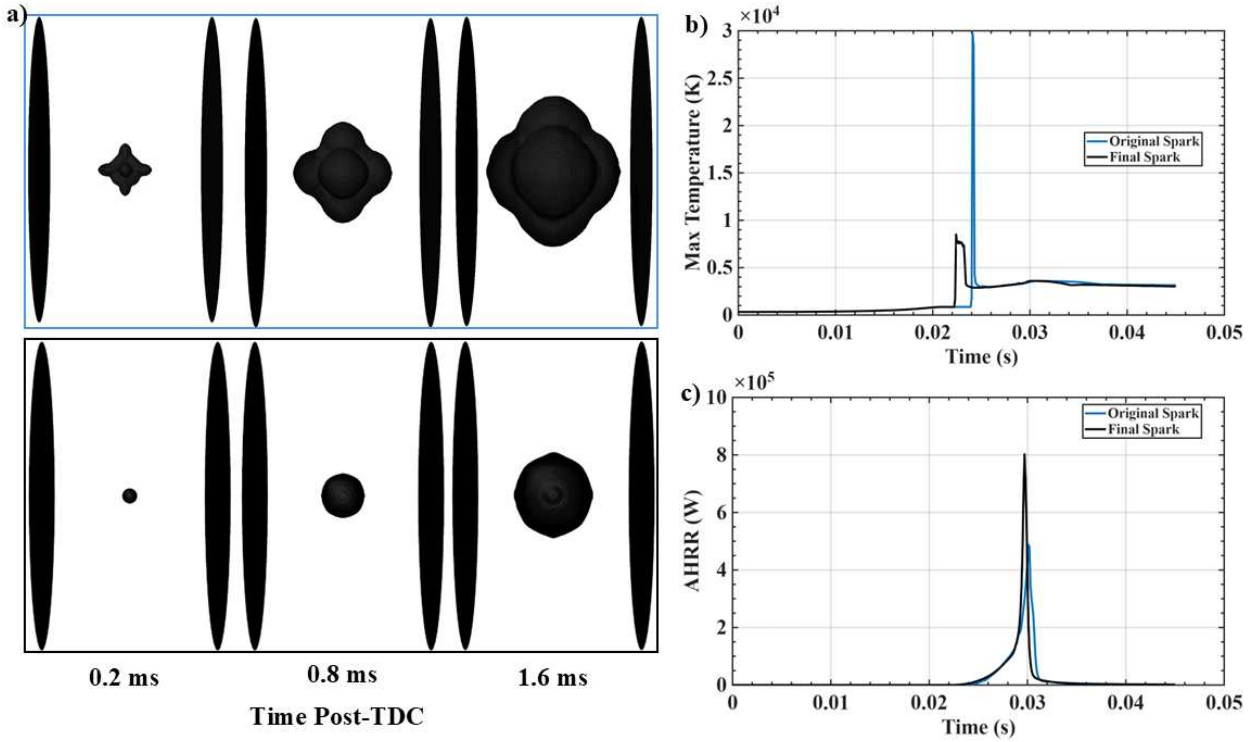

Figure 4.5: Original spark energy and size compared to the final used in the study. The original spark had a spherical radius of 5 E-05 m and energy of 30 mJ where the final has a 0.0625 m radius and energy of 5 mJ. a) presents the flame morphology for each case where the blue square represents the original spark and black is the final spark, b) presents the maximum temperature, and c) presents the apparent heat release rate. This example is for a 10% decomposition case at the highest temperature conditions.

To fix this, a parameter sweep was conducted to identify a ignition kernel that agrees with experimental measurements and is realistic. The parametric sweep focused on the spark timing, energy, and kernel radius. This was done using the 10% decomposition case at 840 K and 25 bar.

Figures 4.6a and 4.6b present the parametric sweep and the sensitivity they have on the pressure trace and maximum temperature. Group 1 evaluated kernel sizes and energy values while keeping the timing constant. It was found that lower energy values and smaller kernel radius produced the most accurate pressure traces. Group 2, fixed the kernel radius to 0.0625 m - similar to the 0.1 m radius in group 1 and a volume that is small enough to allow for ample time for modeling kernel growth - and varied the ignition energy and timing.

The sweep showed that a configuration of 5 mJ energy, 0.0625 m radius, and a timing window for 22.5-23.5 ms gave the closest agreement with the experimental pressure traces. While the kernel temperature reached 8000 K - still higher than the adiabatic flame temperature - this spike dissipates rapidly and does not affect the flame morphology as seen in Figure 4.5.

These optimized energy and timing match well with the experimental diagnostics. The 5 mJ total energy deposition is similar to the delivered energy seen in the experimental work of 2-3 mJ, calculated in Section 2.4.1. In addition, the ignition timing at 22.5 ms is consistent with the experimental firing, which triggers 1 ms post-TDC.

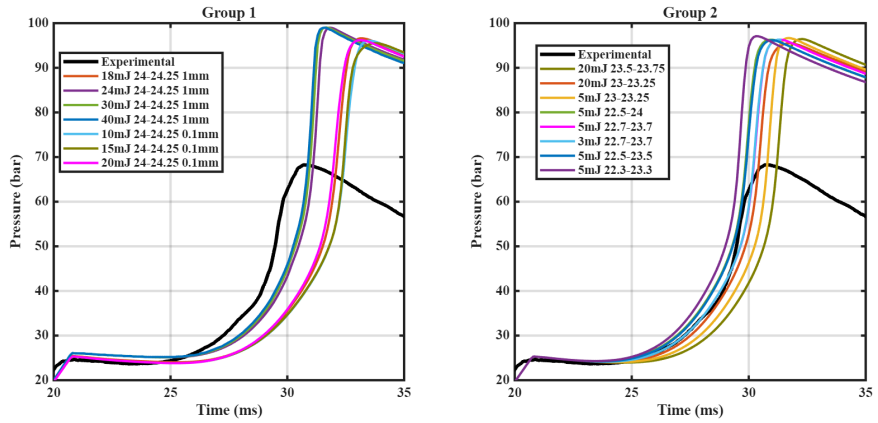

(a) Pressure traces

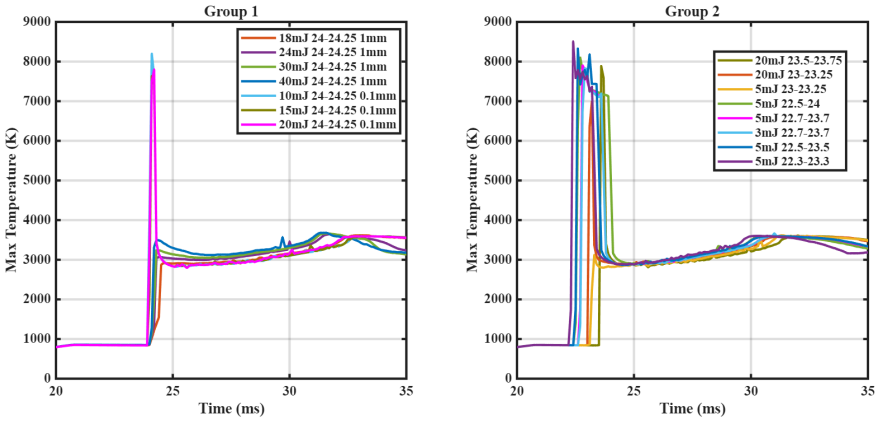

(b) Max temperature traces

Figure 4.6: Spark sweeping. Group 1 represents a fixed time-scaling of 24-24.25 ms and sweep of energy values and sizes. Group 2 represents a set size of 0.0625 mm and a range of timings. These simulations were conducted using the 10% decomposition mixture at the highest temperature condition.

By optimizing the ignition in CFD, the model now successfully avoids artifacts and the non-spherical flame morphology seen in previous simulations using the energy source term, providing a baseline for evaluation the ignition and flame characteristics of fuels in the RCM.

4.3.5 Crevice Burning and Flame Quenching

Initial simulations revealed an over-approximation of the end-of-combustion (EOC) pressure when compared to the experimental pressure traces, as seen in initial simulations and final simulations (Figure 4.6a, 4.9a). This suggested that the model was consuming more fuel mass than occurs in the RCM experiments. In the RCM, depending on the fuel, it is thought that the piston crevices act as a dead-volume, used to catch roll-up vortices generated during the compression stroke. It is also assumed that because of the small gap between the side of the piston and side of the chamber sleeve, wall-flame quenching extinguishes the flame front before propagating into the crevice and igniting the trapped mass in the crevice volumes. Upon post-processing original simulation data, it was apparent that the initial flame traveled into the piston crevices, as shown in Figure 4.8.

Within the CFD model, the entire region is treated as a combustion region. In order to fix this discrepancy and rely on flame-quenching assumptions, a boundary was inserted at the inlet of the piston crevice. The interface functions as a flow-through boundary, allowing fluid to travel between the combustion chamber and the crevice volume through compression and combustion. Using the "Combustion Regions" function, the regions within the piston crevice boundary had combustion disabled. This allows for the model to continue to model fluid flow and trapped mass within the crevices without allowing combustion inside, that is thought to increase the EOC pressure. By using these features, the model is able to simulate "flame quenching" at the boundaries of the piston. Figure 4.7 illustrates the geometry and how this process is implemented.

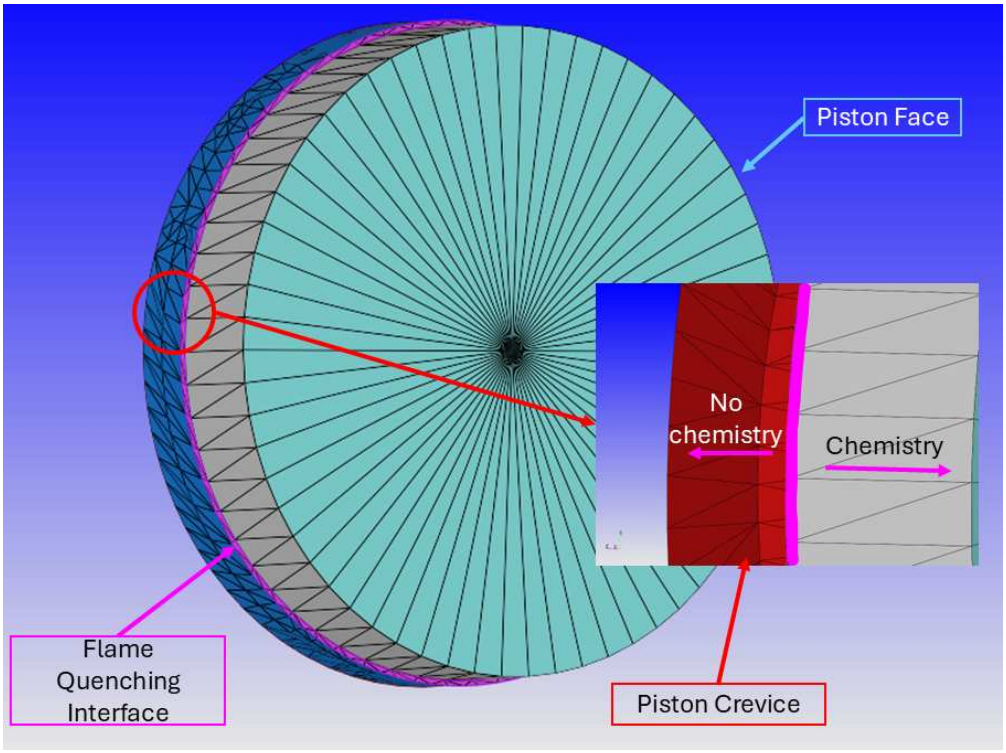

Figure 4.7: Geometry representation of the process used to simulate "quenched" flames in CFD simulations. This image represents the piston where the light blue boundary is the piston face, gray is the side of the piston, red is the piston crevice, blue is the piston-sleeve interaction, and pink is the flow-through interface between the reacting volume and the non-reaction volume.

Figure 4.8 provides an example comparison of the flame morphology between the original (crevice combustion) with the new flame quenching model using a temperature clip located in the middle of the combustion chamber. In the original case (left side), the temperature gradients show the flame front traveling into the crevice volumes. In the flame quenching model (right), the temperature gradients stop directly at the inlet into the creviced volume, correctly stopping the reaction zone from moving into the creviced volumes.

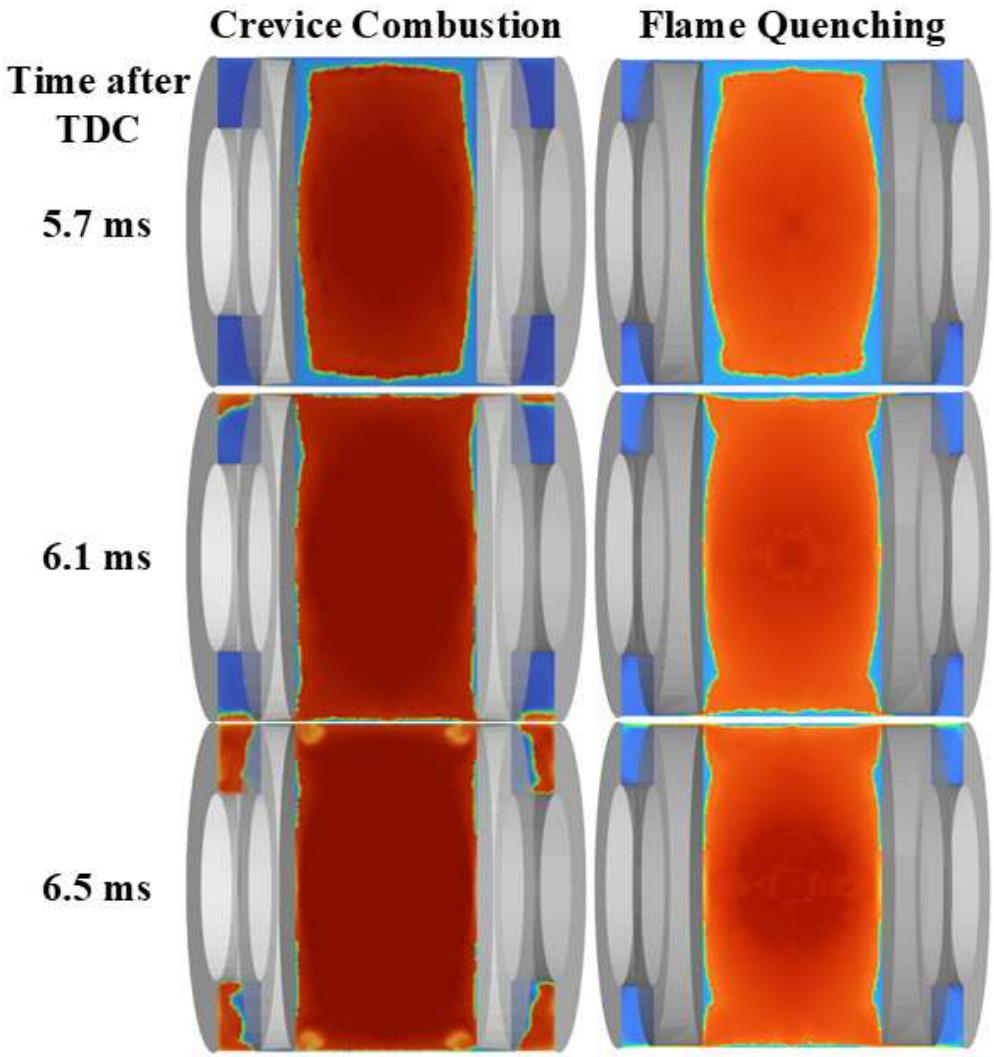

Figure 4.8: Visual comparison of the original simulations allowing for flame propagation into the piston crevice volumes to the flame quenching model. A temperature clip is located in the middle of the chamber where the left set of images represent the original model and the right represents the new model.

The effect of the flame quenching model on the thermodynamic properties is shown in Figure 4.9. By including the flame-quenching, there is a slight shift in combustion phasing to the left. However, by removing chemistry in the crevice volume, the model successfully predicts the EOC pressure, providing a more accurate model to the RCM.

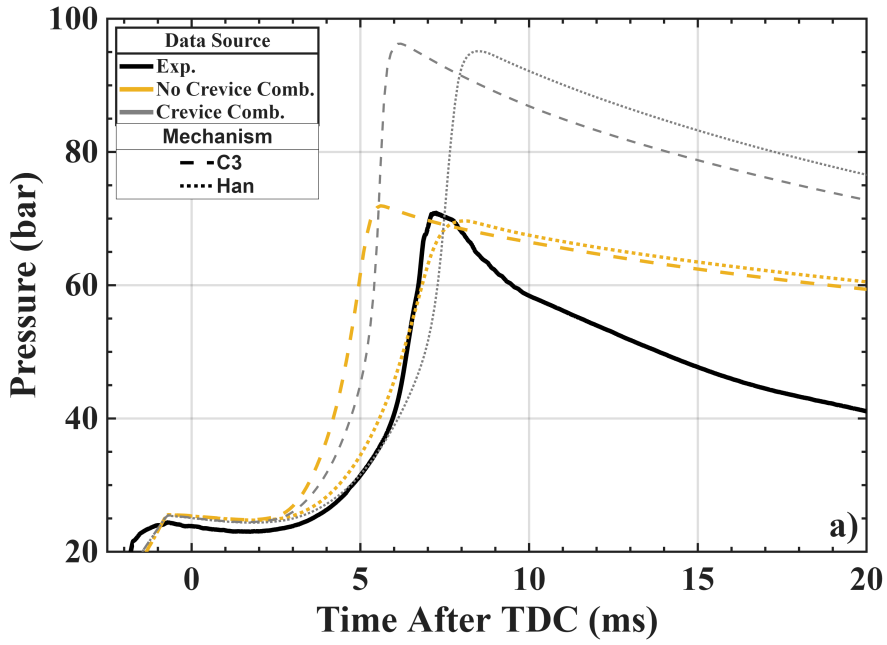

(a) Pressure trace

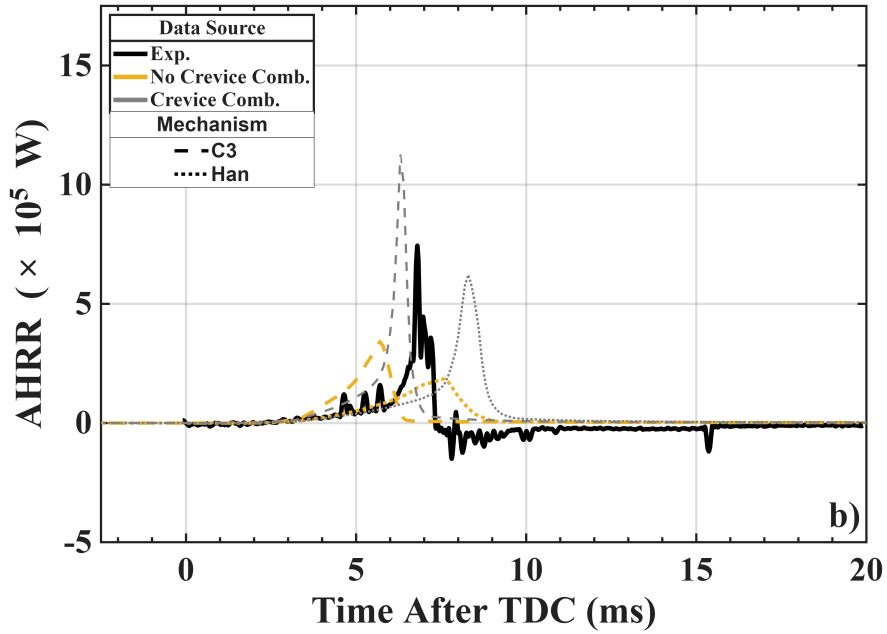

(b) Apparent heat release rate trace

Figure 4.9: Thermodynamic trace comparison of the original combustion model with the simulated flame-wall quenching model. Both the C3 and Han mechanisms are compared to an experimental trace, using the 20% decomposition case. a) represents the pressure effect and b) represents the heat release rate effect.

CHAPTER 5 – EXPERIMENTAL RESULTS

This chapter will cover the experimental findings from the rapid compression machine. Flame speed and diesel droplet ignition delay times were both measured at engine-relevant conditions. These results are the first of their kind and necessary datasets for refinement and tuning of chemical kinetic mechanisms for ammonia.

5.1 Flame Speed Results

This section presents the experimental flame speeds using the laser-ignited RCM across the decomposed ammonia fuel matrix, following the conditions outlined in Chapter 3. All experimental measurements are compared to 1-D Cantera simulations using the kinetic mechanisms outlined in Chapter 4. A summary of the testing matrix including the average temperatures and pressures, measured flame speeds, standard deviations, effective Lewis numbers (Le_{eff}), and flame thicknesses (δ_l) are included in Table 5.1.

The variance in the TDC thermodynamic states (pressure and temperature) are an intrinsic characteristic of the RCM and its operations. As tests are run, offsets and piston blowby lead to changes in the final compressed pressures. Because the TDC temperatures is calculated based on isentropic relations from the measured pressure, these variances propagate into the temperature calculation. Consequently, the standard deviations (StDev) provide confidence in the dataset and thermodynamic conditions.

Repeatability amongst all data points across the data set is important for the development of chemical kinetic mechanisms. To ensure of this, outliers within the data set were omitted. These points were excluded if the offsets were more than 6 ms offset (explained later in Section 5.1.2), if there were significant fluctuations in the laser ignition energy, high deviations in the compressed pressures and temperatures, and points where the MATLAB image-processing failed to capture the flame front correctly.

Table 5.1: Averaged experimental conditions and standard deviations for TDC temperatures and measured flame speeds. Effective lewis number (Le_{eff}) [70] and flame thickness (δ_l) were computed via Cantera using the NUIG mechanism. The flame thickness was calculated using the Full Width Half Maximum (FWHM) of the NH_2 radical concentration profile [72].

Mixture	P (bar)	Avg. T (K)	StDev T (K)	Avg. S_L (cm/s)	StDev S_L (cm/s)	Le_{eff}	δ_l (μm)
0%D	25	763.29	1.85	37.19	2.69	1.00	23.21
0%D	25	796.82	2.78	42.54	2.09	0.997	22.23
0%D	25	833.25	4.78	49.23	1.06	0.990	21.34
10%D	25	767.27	1.61	52.09	2.78	0.961	20.66
10%D	25	793.11	2.37	56.22	2.78	0.954	19.85
10%D	25	836.27	1.44	65.85	3.56	0.947	19.11
10%D	20	839.79	5.05	74.85	4.28	0.947	22.94
10%D	30	843.41	2.37	71.56	1.95	0.947	16.46
20%D	25	779.93	3.47	65.41	1.56	0.922	17.94
20%D	25	806.25	2.93	79.30	2.32	0.914	17.28
20%D	25	853.23	1.35	89.06	1.75	0.908	16.67
42.5%D	25	810.24	4.03	182.60	5.17	0.838	11.55
42.5%D	25	841.46	2.78	207.25	3.46	0.832	11.19

5.1.1 Decomposition Effects

Figure 5.1 presents the measured flame speeds of decomposed ammonia mixtures as a function of the decomposition percentage. As reflected in these measurements, ammonia decomposition significantly increases the flame speed, as the hydrogen percentage enhances both the mixture reactivity and adiabatic flame temperatures increasing the resulting propagation rate. This promoting effect of hydrogen (H_2) is stronger than the inhibiting influence of the addition nitrogen (N_2) diluent produced through the decomposition process.

Across the 760–840 K temperature range at 25 bar, the experimental flame speed increases by an average of 25.5$\pm$2.7% for every 10% step in decomposition percentage. This trend is consistent with previous low-pressure findings from Mei et al. [8], who reported a 41% increase for the 10%-20%D step.

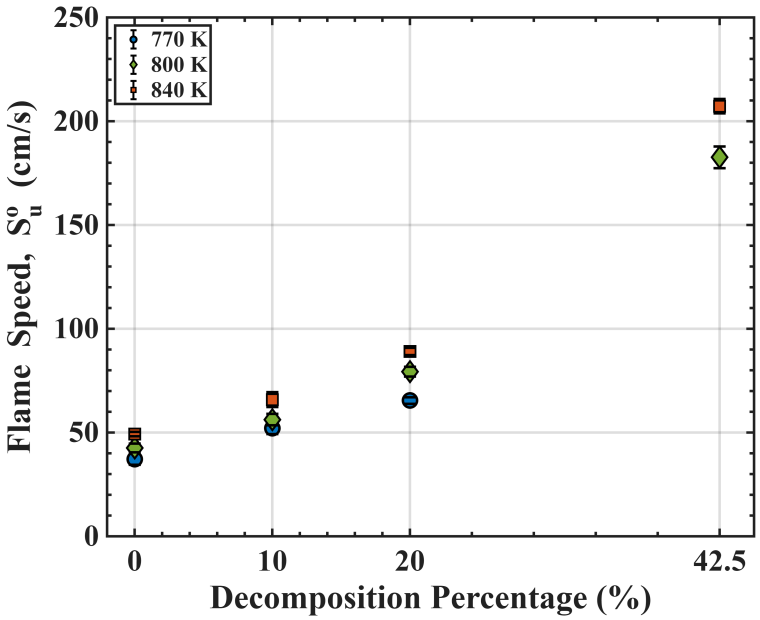

Figure 5.1: Decomposition percentage sweep for each temperature case at 25 bar.

Figure 5.2 presents all measured flame speed against the simulation results as a function of the temperature. All mechanisms listed in Section 4.1.1 were used to simulate the flames at the 25 bar. Increasing the temperature subsequently increases the flame speed which is expected of flames.

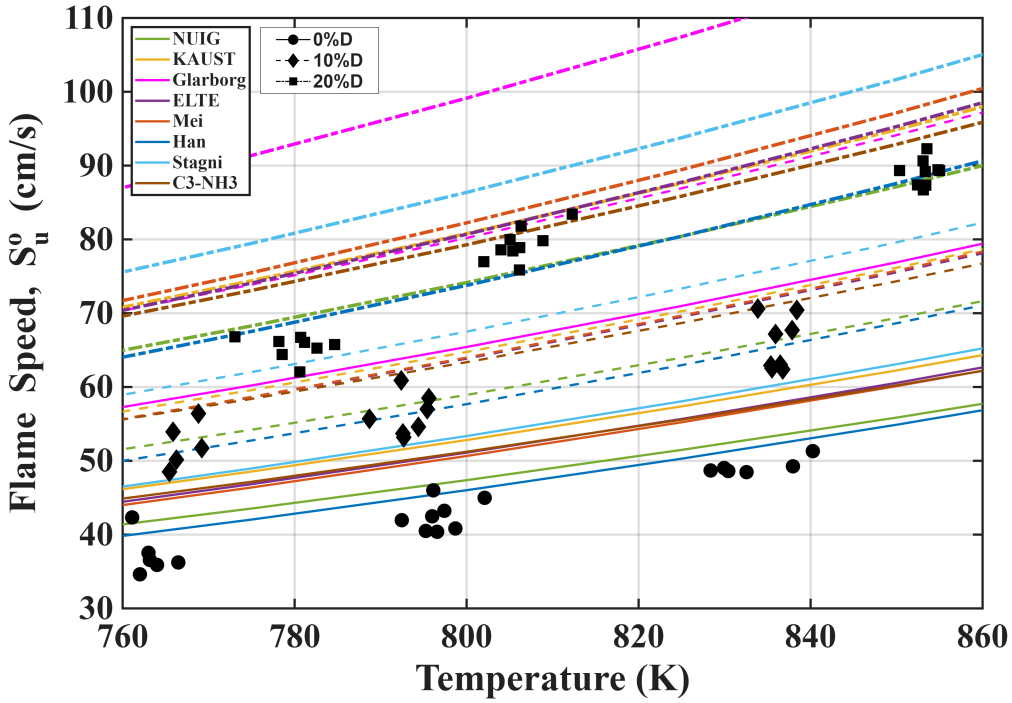

Figure 5.2: Temperature sweep of flame speeds of decomposed ammonia mixtures for 0%D, 10%D, and 20%D mixtures at 25 bar. Lines indicate 1-D simulation results with varying mechanisms as shown in Chapter 4.

When comparing simulated values to experimental values, the NUIG and Han mechanisms provide the best agreement with experimental values at the lower decomposition mixtures. As shown in Figure 5.2, these mechanisms fall within the grouping of the experimental data. However, all other mechanisms overpredict the flame speed, specifically Glarborg and Stagni. By evaluating the measurement error from the error relative to the experimental values (Table 5.2), this confirms the findings in Figure 5.2. Across the 0–20% decomposition, the NUIG and Han mechanisms maintain an overall error of -2.47% and -4.22%, respectively. Conversely, the Glarborg and Stagni mechanisms consistently produce the highest overpredictions, with both showing errors of -41.9% and -19.35%, respectively. The KAUST, Mei, ELTE, and C3 mechanisms produce relatively similar flame speeds and subsequent errors around -13% for these mixtures.

When including the 42.5% decomposition cases, the errors become more varied, as instead of most mechanisms overpredicting, all of them underpredict. Among these, the Han and NUIG mechanisms appeared to be the least accurate among these at average errors of 25.4% and 23.19%,while

Glarborg is the most accurate at an error of 6.93%. Since the trend is flipped at these increased decomposition ratios and mechanisms do not follow the same trends as seen at lower decompositions, it is likely that the mechanisms cannot correctly model hydrogen chemistry, which will be touched on in the flame morphology.

Table 5.2: Comparison of experimental S_L with numerical predictions. Values in parentheses represent the percent error from the experimental points.

T (K)	Exp.	NUIG	KAUST	Glarborg	ELTE	Mei	Han	Stagni	C3
0% Decomposition									
736.29	37.19	41.98 (-12.9)	46.78 (-25.8)	58.10 (-56.2)	45.14 (-21.4)	44.67 (-20.1)	40.47 (-8.8)	47.18 (-26.9)	45.50 (-22.3)
796.82	42.54	47.03 (-10.5)	52.40 (-23.2)	64.98 (-52.7)	50.76 (-19.3)	50.28 (-18.2)	45.71 (-7.4)	52.96 (-24.5)	50.86 (-19.6)
833.25	49.23	53.06 (-7.8)	59.12 (-20.1)	73.17 (-48.6)	57.49 (-16.8)	57.00 (-15.8)	52.00 (-5.6)	59.87 (-21.6)	57.25 (-16.3)
10% Decomposition									
767.27	52.09	53.00 (-1.8)	58.24 (-11.8)	72.31 (-38.8)	57.26 (-9.9)	57.33 (-10.1)	51.56 (1.0)	60.59 (-16.3)	57.12 (-9.7)
793.11	56.22	57.79 (-2.8)	63.49 (-12.9)	78.75 (-40.1)	62.63 (-11.4)	62.76 (-11.6)	56.55 (-0.6)	66.15 (-17.7)	62.18 (-10.6)
836.27	65.85	66.55 (-1.1)	73.07 (-11.0)	90.51 (-37.5)	72.45 (-10.0)	72.64 (-10.3)	65.78 (0.1)	76.33 (-15.9)	71.43 (-8.5)
20% Decomposition									
779.93	65.41	69.48 (-6.2)	75.74 (-15.8)	93.16 (-42.5)	75.52 (-15.5)	76.96 (-17.7)	68.90 (-5.3)	80.94 (-23.7)	74.39 (-13.7)
806.25	79.30	75.94 (4.2)	82.77 (-4.4)	101.69 (-28.2)	82.82 (-4.4)	84.39 (-6.4)	75.72 (4.4)	88.56 (-11.7)	81.19 (-2.4)
853.23	89.06	88.35 (0.8)	96.24 (-8.1)	118.01 (-32.5)	96.80 (-8.7)	98.66 (-10.8)	89.05 (0.0)	103.16 (-15.8)	94.16 (-5.7)
Average (0–20%)		-4.22%	-14.78%	-41.90%	-13.05%	-13.43%	-2.47%	-19.35%	-12.09%
42.5% Decomposition									
810.24	182.60	138.05 (24.4)	149.27 (18.3)	172.24 (5.7)	148.66 (18.6)	160.77 (12.0)	141.74 (22.4)	165.03 (9.6)	143.82 (21.2)
841.46	207.25	152.71 (26.3)	165.03 (20.4)	190.27 (8.2)	165.00 (20.4)	178.04 (14.1)	157.51 (24.0)	182.40 (12.0)	158.66 (23.4)
Averaged (All)		1.15%	-8.58%	-33.02%	-7.13%	-8.62%	2.20%	-13.86%	-5.83%

To understand where the divergence in the high decomposition cases is from limitations in the mechanisms or experimental uncertainty, the mean across all mechanisms was taken, then each error from that mean value was taken across the entire temperature sweep for each decomposition,

shown in Table 5.3. Among all mechanisms, NUIG is the only one that maintained a consistent error across all decomposition ratios, suggesting that this mechanism is stable. On the other hand, all other mechanisms show sensitivity to hydrogen addition, with calculated error increasing or decreasing from previous values as decomposition increased.

Table 5.3: Mean deviation of simulated flames from the averaged value of all mechanisms. Each value represents the average percentage error of each mechanism from the mean of all mechanisms at all temperature points.

Avg. Error	NUIG	KAUST	Glarborg	ELTE	Mei	Han	Stagni	C3
0%D	-9.31%	1.09%	25.21%	-2.21%	-3.08%	-11.94%	2.13%	-1.90%
10%D	-9.36%	-0.43%	23.34%	-1.83%	-1.65%	-11.32%	3.78%	-2.53%
20%D	-9.61%	-1.53%	20.85%	-1.67%	0.20%	-10.15%	5.28%	-3.37%
42.5%D	-9.40%	-2.01%	13.09%	-2.53%	5.41%	-7.31%	8.28%	-5.54%

This sensitivity shows that these mechanisms lack the understanding of high-hydrogen, engine-relevant conditions. While the NUIG mechanism is consistent among the other mechanisms, all other mechanisms - and possibly NUIG - lack the pathways needed to calculated these conditions. These calculated errors suggest that for the 42.5% decomposition case, the large deviation between the experimental and simulated cases is due to the mechanisms rather than the data.

Figure 5.3 presents flame morphologies of the 0%, 10%, 20%, and 42.5% decomposition cases at the highest temperature cases, all with offsets below 0.3 ms (25 bar and 840 K). An important aspect of these flames are the presence of lobes around the flame front. These are an artifact of the non-spherical initial energy deposition from the laser spark, as detailed in past studies from Dumitrache et al. [58, 85]. Most importantly, despite the shape and subsequent potential increase in flame speed, these lobes are shown to have a negligible effect on the flame speed, as explained later in Section 5.1.5.

Another feature seen on the flame front is the lobes at the bottom of the flame kernel. In the 0% and 10% decomposition mixtures (the slowest of all flames), this lobes is seen throughout the entire propagation time frame until the flame interacts with the piston walls. However, as the decomposition percentage increases to 20% and 42.5%, this lobe is quickly overtaken and

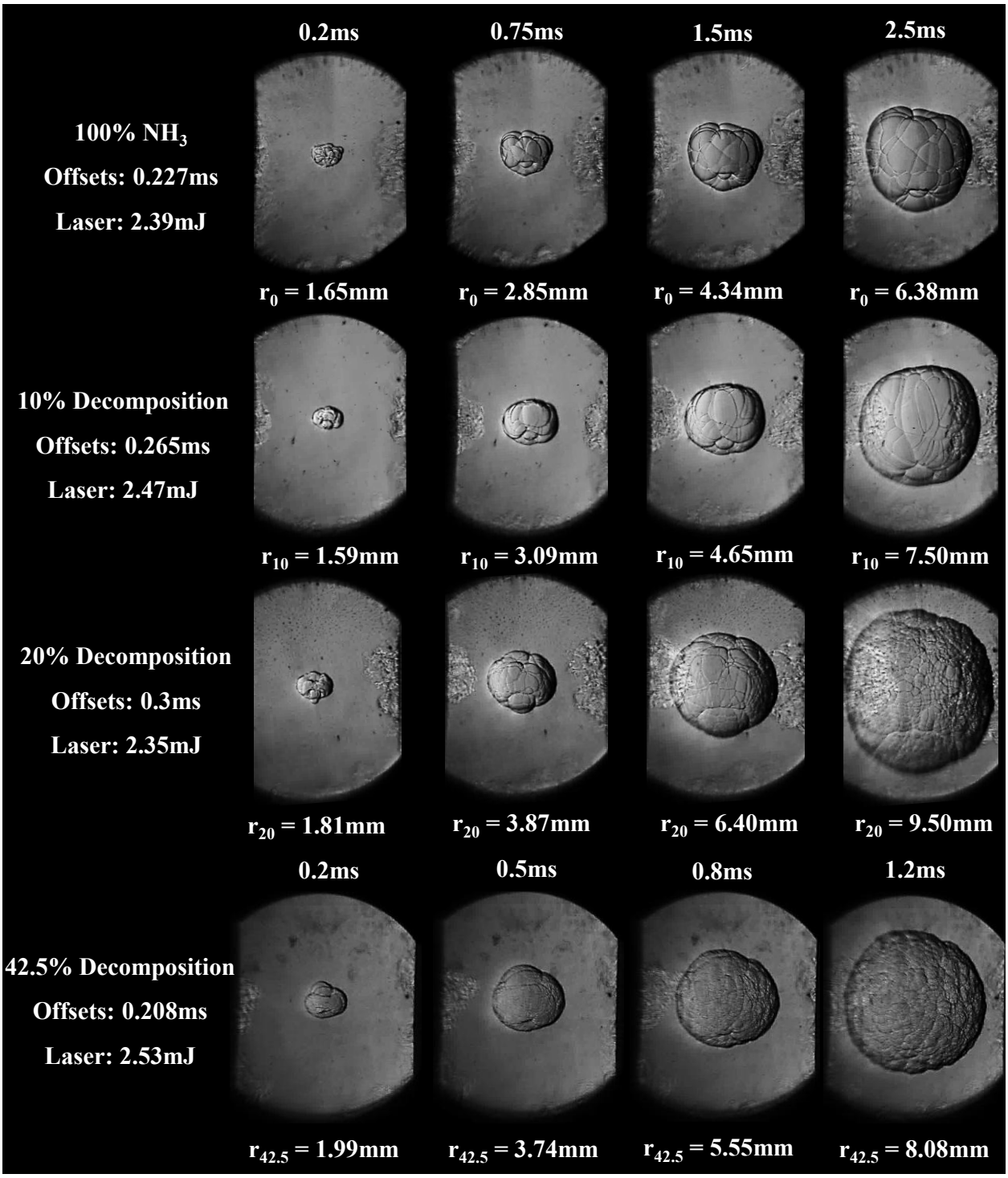

Figure 5.3: Flame morphology of decomposed ammonia mixtures. All flames shown have offsets < 0.3 ms, are at the highest temperature condition (840 K), and 25 bar.

consumed by the flame. This suggests that the higher reactivity of hydrogen smooths out the initial spark-induced lobes, showing that this lobed feature is less of a factor at high decomposition ratios.

Hydrogen's impact on the propagation rate is apparent directly in the flame morphology. Comparing the 0% and 20% decomposition cases at 2.5 ms, the 20% flame is approximately 3 mm larger in radius, corresponding to a ∼40 cm/s increase, as seen previously at these higher temperatures. When comparing the time rate, it takes roughly 2 ms for the 20% decomposition case to reach a radius of 8 mm, whereas the 42.5% decomposition case achieves this size in only 1.2 ms. This rapid expansion in the flame confirms that even moderate decomposition ratios greatly effects the flame front and subsequent flame speed as seen in the measured values.

With the introduction of hydrogen through decomposition, fine, cellular instabilities are seen along the flame front. These instabilities were first seen primarily in the 10% decomposition flame, with increasing cells in the flame with increasing decomposition, especially when compared to the 0% decomposition case. The 42.5% decomposition case has these instabilities across the entire flame front, unlike the other mixtures.

This transition in morphology from pure ammonia to decomposed mixtures (introduction of hydrogen) is consistent with behavior seen in literature where by reducing the effective Lewis number (Le_{eff}) an energy imbalance is seen [86]. Table 5.1 has calculated effective Lewis numbers, where the addition of hydrogen through decomposition reduces the Le_{eff} below unity, which is seen in pure ammonia. Lewis numbers below unit signify an imbalance in thermodynamic and mass diffusion, where mass diffusion is dominant. These instabilities increase the surface area of the flame, increasing the flame speed. This concept is explained previously in Section 3.8 and the effect of this regarding 1-D simulations in later explained in Section 5.1.3.

5.1.2 Piston Offset Effects

As detailed previously in Section 2.1.1, piston offsets are an inherent attribute of the RCM due to the nature of seal friction and the hydraulic pressure during the compression stroke. During experimental testing, it is possible for offsets to range from 0–12 ms. Due to the time it takes to complete an experiment, it would be optimal to use every test point, however, these offsets generate bulk-gas motion and turbulence inside of the chamber (further explained using CFD in Section 6.1). This will significantly affect the flame front, creating a disturbed, turbulent flame.

Because of this, it is important to set a threshold where a majority of data can still be used without effecting the final flame speed value.

To find this threshold, all flame speed measurements were plotted as a function of the piston offset, as shown in Figure 5.4. For offsets < 6 ms (left of the red dotted line), the measured flame speeds remain repeatable for a given mixture, indicating that the bulk-gas motion induced by the pistons is insufficient enough to affect the flame front. Beyond 6 ms, the measured flame speed increases non-linearly (relative to the mixture). To illustrate this sensitivity, an exponential trend line was fit to the 840 K, 25 bar, 20% decomposition case, where the bulk gas motion affects the flame front.

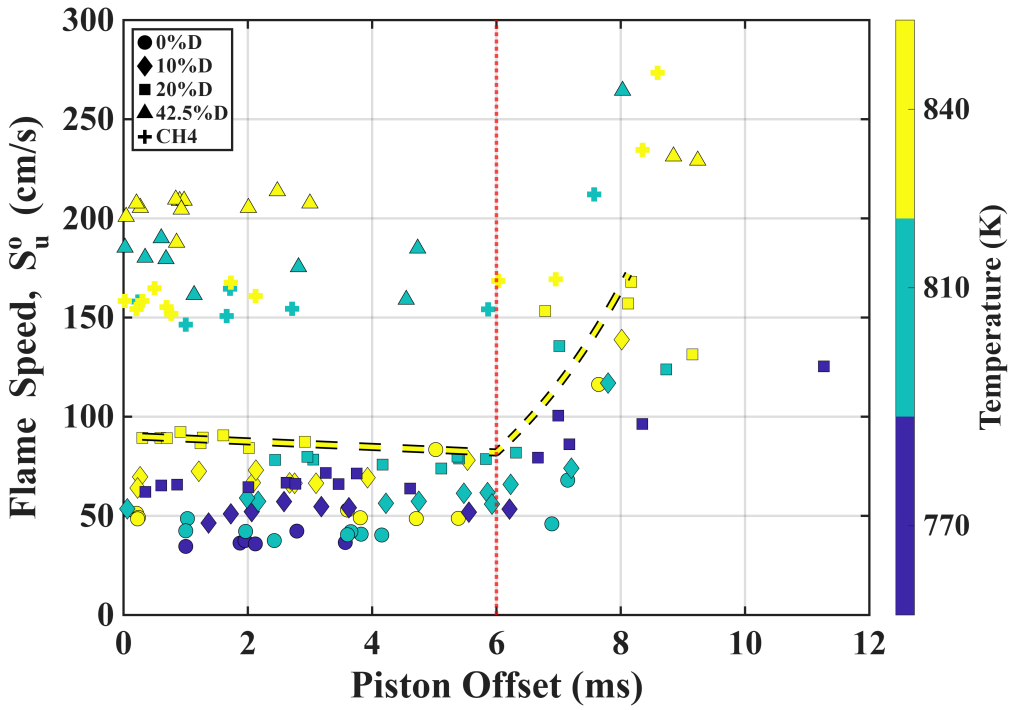

Figure 5.4: Measured flame speeds as a function of corresponding piston offset. The red dashed line signifies the 6 ms cutoff. The yellow exponential trend line highlights the repeatability maintained for offsets <6 ms ad the subsequent increase in flame speed. All flames are at pressures of 25 bar.

This non-linear increase in flame speed and induced bulk-gas flow is seen in schlieren imaging as well. Figure 5.5 presents a "turbulent affected" case at an offset of 8.73 ms. While the flame

kernel remains relatively circular (minus the laser-induced lobes) and similar to what is seen in standard flames less than 0.32 ms, the affects of turbulence becomes apparent as the flame grows.

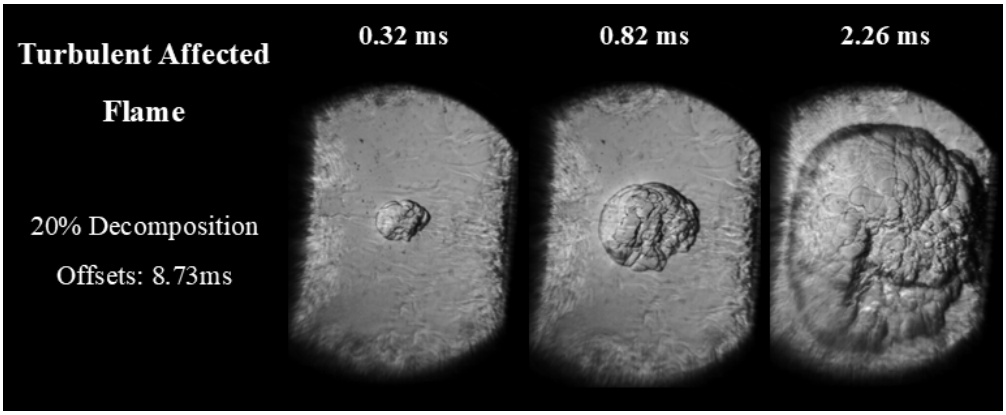

Figure 5.5: Example of a turbulent-inducted flame from high offsets. This shows the flame morphology of a flame at 840 K, 25 bar at 20%D at a 8.12 ms offset. The corrected flame measures at 157.07 cm/s.

Once the flame propagates to around half of the chamber, the bulk-flow is seen to affect the flame in the bottom right. In this case, the right piston came in first, with the left coming in 8.73 ms after. When the flame reaches the piston walls, the flame front is almost entirely taken up by the turbulence. The corrected flame speed for this point is 157.07 cm/s, almost 80 cm/s (2x) faster than the reported flame speeds. This flame morphology and measured values is consistent with all other turbulent effected cases. This turbulent is further quantified using 3-D simulations, including the velocity field in the chamber and is provided in Section 6.1.

By quantifying this threshold for piston offsets, this ensures a point at which only trials below a 6 ms piston offset should be included in the final dataset for kinetic validation. This threshold ensures that all reported flame speeds are free from the effect of bulk-gas flow and turbulence generated by piston offsets, maximizing the amount of experimental test points and repeatable flames without uncertainty.

5.1.3 42.5% Decomposition vs Methane

Identifying an ammonia decomposition ratio that yields combustion characteristics comparable to that of natural gas (methane, CH_4) is essential for retrofitting existing natural gas engines for

ammonia-derived fuels. While flame speeds present one critical combustion parameter within an internal combustion engine, other metrics like knock tendencies, emissions, and ignition need to be investigated. However, flame speeds serve as a fundamental kinetic baseline for assessing decomposition ratios.

Preliminary 1-D simulations using Cantera were conducted with the C3-NH_3 mechanism and C3-CH_4 to evaluate potential decomposition percentages similar in flame speed to stoichiometric methane. A temperature and decomposition sweep was conducted, where a decomposition percentage of 42.5% was identified to give similar flame speeds to that of methane. Subsequently, this mixture was chosen for testing. This is further outlined in Section 3.4.1.

Figure 5.6 compares the measured and simulated flame speeds for both the methane and decomposed ammonia mixtures at 25 bar. While the methane mixture agrees well with the representative C3-CH_4 mechanism, the ammonia kinetic mechanisms fail to capture the elevated flame speeds of the experimental 42.5% decomposition mixture. Notably, all eight mechanisms significantly underpredict the measured flame speeds, with the NUIG and Han mechanisms - which demonstrated the highest accuracy at lower decompositions - underpredict the flame speed by approximately 60 cm/s or $\sim$28%. It is important to note that all the mechanisms follow the same trends seen at lower decomposition percentages, with slight variation.

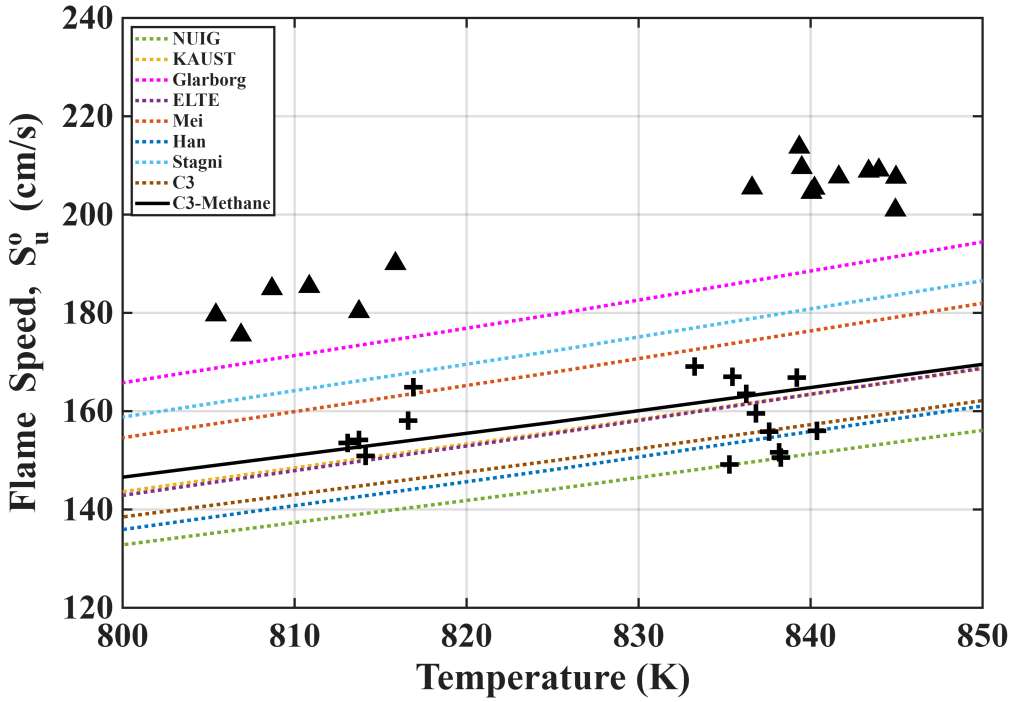

Figure 5.6: Comparison of 42.5%D against the baseline CH_4 mixture, both are at 25 bar and ϕ=1. Lines indicate 1-D simulation results with varying mechanisms as shown in Chapter 4.

The large discrepancy seen between 1-D simulations and the experimental data points likely arise from limitations in current chemical kinetic mechanisms at high-temperature/pressure kinetics in hydrogen-rich mixtures. As documented in Table 5.1, the effective Lewis number for the 42.5% decomposition case drops well below unity and the other points at a minimum of 0.832, promoting thermodiffusive instabilities. To quantify this, the flame acceleration values d^2r/dt^2 were derived from the second-order polynomial fits of the time-dependent flame radius during flame measurement.

As shown in Table 5.4 and Figure 5.7 it is seen that as the decomposition percentage increases from 0–42.5%, the subsequent acceleration increases. Pure methane and lower decomposition ratios exhibit a negative acceleration (deceleration), whereas the 42.5% is the only case to have a positive acceleration. This self-acceleration validates that the propagation rate is driven by cellular and Darrieus-Landau instabilities in the flame front, which is seen in the flame morphology. Darrieus-Landau (DL) instabilities are a hydrodynamic instability where the thermal expansion

or density jump in combustion induces hydrodynamic instabilities enhancing perturbations in the flame front [87]. This self-acceleration phenomenon is seen in work from Bradeley et al. and Huo et al. who studied the self-acceleration of hydrodyamically unstable laminar flames. [88, 89].

Table 5.4: Time dependent radius second polynomial curves as seen in Figure 5.7. Accelerations of the 25 bar, ∼840 K cases of each mixture were extracted from the flame radius (d^2R/dt^2) by applying a second-order polynomial fit to the radius vs time data ($R(t) = at^2 + bt + c$).

Mixture	a (at^2)	b (bt)	c	Acceleration (m/s^2)
0%D	-0.169	2.2891	1.2325	-0.338
10%D	-0.0909	2.8470	1.0306	-0.1818
20%D	-0.0772	3.6821	0.9057	-0.1544
42.5%D	0.3649	5.4999	0.7133	0.7298
CH_4	-0.3393	6.3816	0.9104	-0.6786

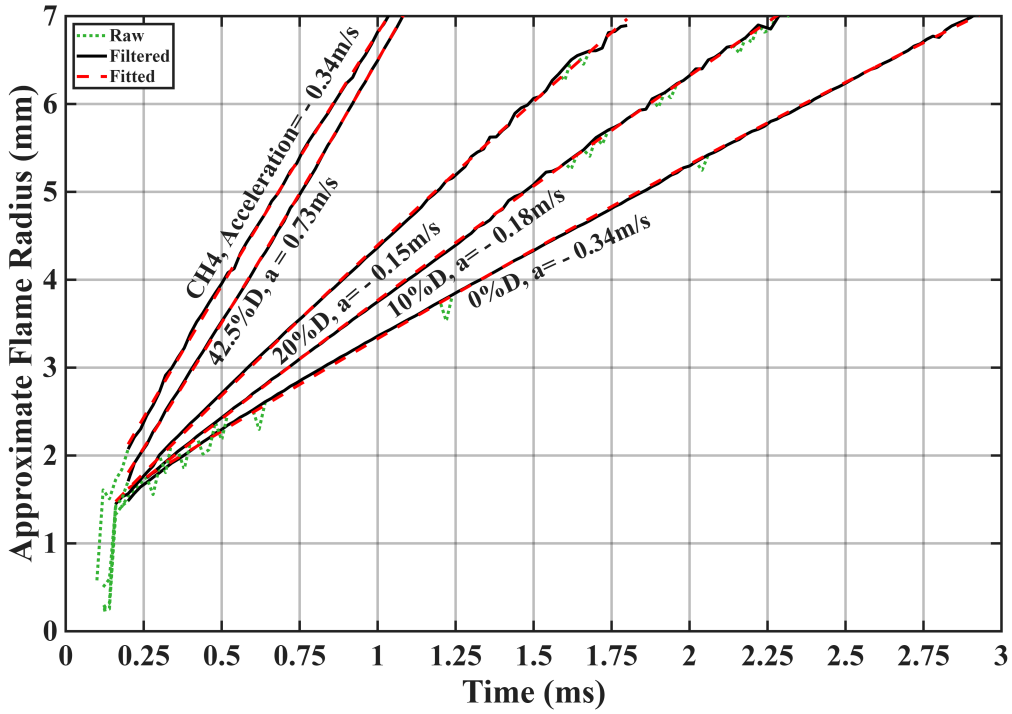

Figure 5.7: Measured flame radius as a function of time for each mixture at ∼840 K and 25 bar. Second-order polynomial fits from the flame measurement MATLAB code were used to calculate acceleration constants. Curves here represent flames that have offsets less than 0.2 ms.

Despite the under prediction from all mechanisms, the Glarborg mechanism is the most accurate at these high hydrogen concentrations when compared to the NUIG and Han mechanisms. The change between the Glarborg and other mechanisms follows the same trend seen in the lower decomposition cases. This flip, where all mechanisms all now under predict instead of overpredicting , combined with the increased cellular instabilities seen in the flame morphology (Figure 5.9) are likely due to the mechanisms. The discrepancies are due to these mechanisms limitation to capture the high-pressure/temperature kinetics in these hydrogen-rich mixtures, as well as challenges in representing the complex transport behavior of highly diffusive blends under these conditions.

To evaluate the kinetic discrepancies across all the mixtures, a sensitivity analysis was performed comparing the ten most sensitive reactions for Glarborg, NUIG, Han, and C3 at 850 K and 25 bar, as shown in Figure 5.8. Notably, the Han mechanism exhibits a higher sensitivity to the chain-terminating reaction $H + O_2 (^+M) \longleftrightarrow HO_2 (^+M)$ when compared to the C3 and NUIG models, underscoring the critical influence of third-body collision efficiencies at these elevated pressures. Furthermore, specific intermediate pathways - such as $HNO \longleftrightarrow H + NO$ and $N_2H_2 + M \longleftrightarrow H + NNH + M$ - are absent from the Han mechanism but included in the C3 and NUIG mechanisms, where their presence promotes flame propagation. Interestingly enough, the Glarborg mechanism is the only one to include reaction 8 ($H + NO (^+M) \longleftrightarrow HNO (^+M)$). This chain-terminating reaction actually inhibits the development of the flame, however, the Glarborg mechanism at this condition significantly has a significantly higher flame speed than that of the other mechanisms. The combination of these pathways for the Han model provides an explanation for the slower flame speeds predicted, especially to that of C3, particularly at lower decomposition ratios.

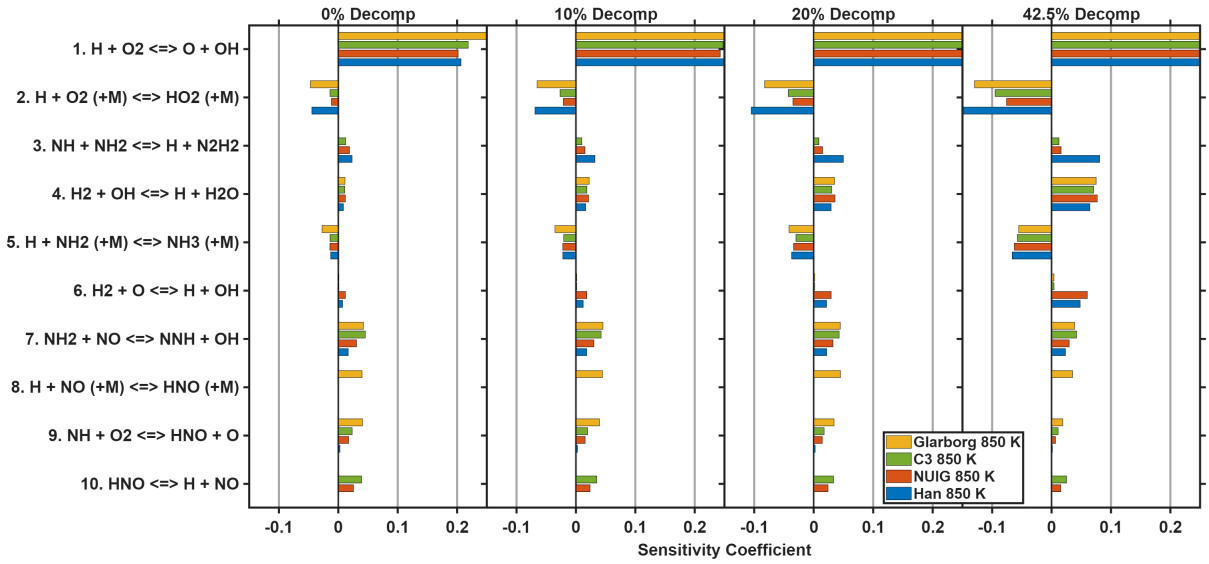

Figure 5.8: Sensitivity analysis for the Han, C3, NUIG, and Glarborg mechanisms at 25 bar and 850 K.

Figure 5.9 compares the flame morphology of the stoichiometric methane to the 42.5% decomposition case, at 25 bar and 840 K. The increased hydrogen content shows significantly more cellular instabilities than the methane, 10%, and 20% decomposition cases at the same temperatures and pressures. Both methane and 42.5% decomposition flames increase in radius at a similar rate at early times, however, the 42.5% decomposition case undergoes a rapid acceleration in propagation rate from 0.8 ms to 1.2 ms. Cellular instabilities also appear to rapidly grow with and multiply across the flame surface, allowing the ammonia mixture to propagate much faster than the baseline methane case at these later times.

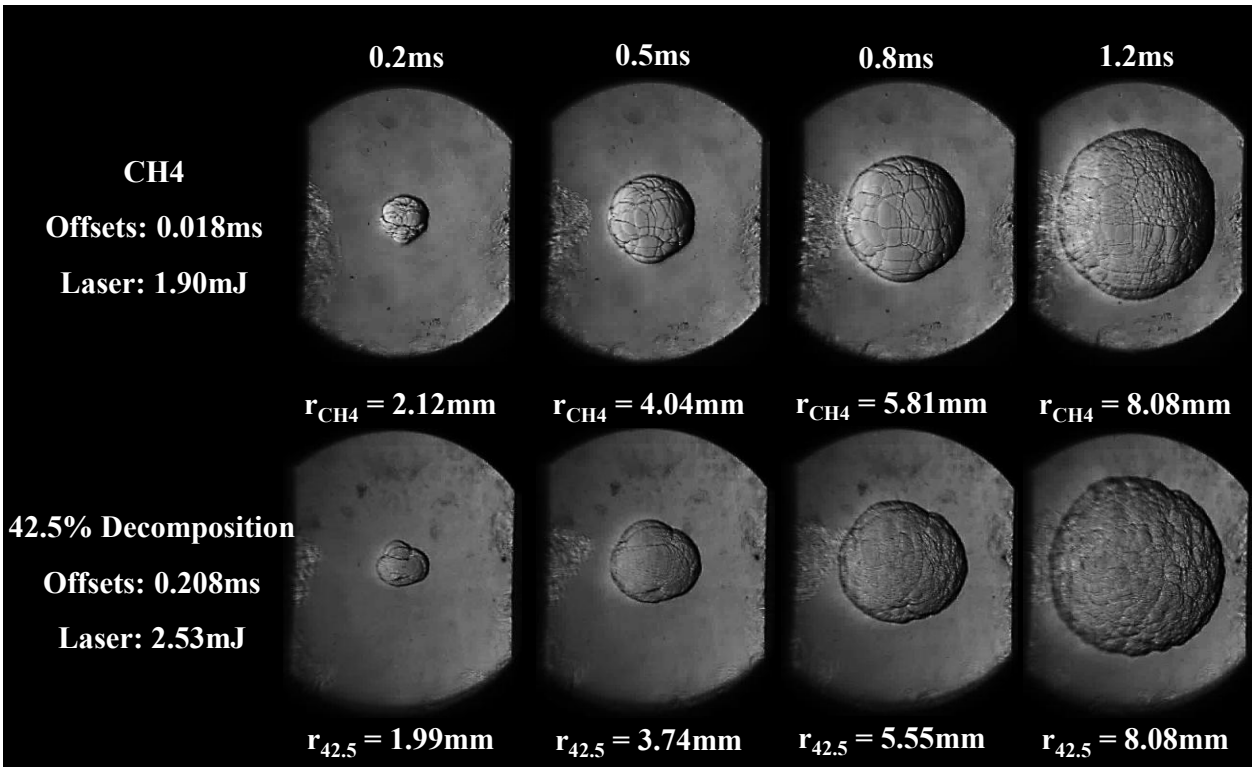

Figure 5.9: Comparison of the flame morphologies of the 42.5%D against the baseline CH_4 mixture both at 25 bar.

5.1.4 Pressure Effect

The influence of pressure on flame speed measurements is a commonly understood property. Typically, increasing pressure results in a decrease in the flame speed, as higher pressure reduce the concentration of key three-body chain-branching reactions.

As presented in Figure 5.10 the influence of pressure is highlighted for the 10% decomposition mixture at the highest temperature case ($\sim$840 K). The experimental data initially follows the expected theoretical trend - that as pressure increases, flame speed decreases - consistent with previous ammonia flame speeds [8, 32, 38]. However, the 30 bar case breaks this trend, showing an increase in flame speed.

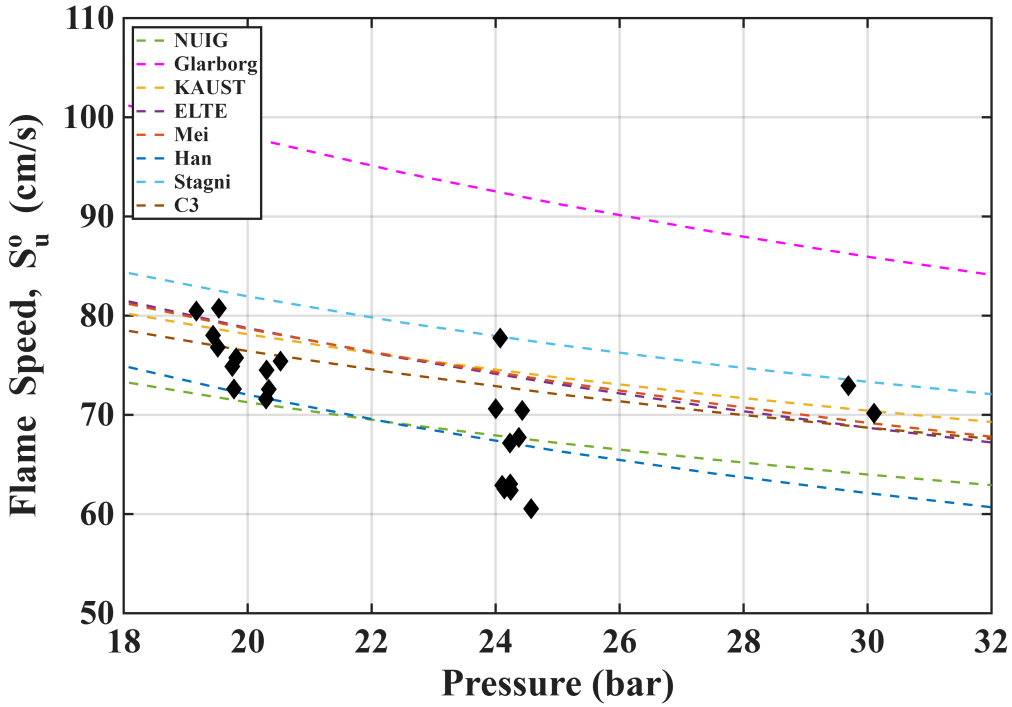

Figure 5.10: Pressure sweep of 10%D mixture all at ∼835 K. Lines indicate 1-D simulation results with varying mechanisms as shown in Chapter 4.

The non-theoretical increase in flame speed is likely attributed to the reduction of the flame thickness, as shown in Table 5.1. Moving from 20 to 25 to 30 bar the flame thicknesses are 22.94, 19.11, and 16.46 μm, respectively. Due to the decrease in flame thickness, this reduces the damping effect of the flame front against hydrodynamic perturbations across the flame front, allowing for more cellular instabilities and self-acceleration of the flame. Since these tests are conducted with the 10% decomposition mixture, the increased pressure promotes hydrogen diffusion at these higher pressures [90]. This makes the flame become more susceptible to cellular instabilities. As the flame becomes thinner at higher pressures, it transitions to a cellular morphology where the propagation rate is influenced by these instabilities.

Figure 5.11 shows the effects pressure has on the flame morphology for the 10% mixture at ∼840 K. At 30 bar, the flame front exhibits cellular instabilities, similar in appearance to what is seen for the 20% decomposition case (Figure 5.3). These instabilities, known to influence high pressure and thinner flames, increase the flames' total surface area, enhancing the overall burn rate

and results in the slightly higher measured flame speeds despite the higher pressure, as discussed earlier providing context to the trend seen in Figure 5.10.

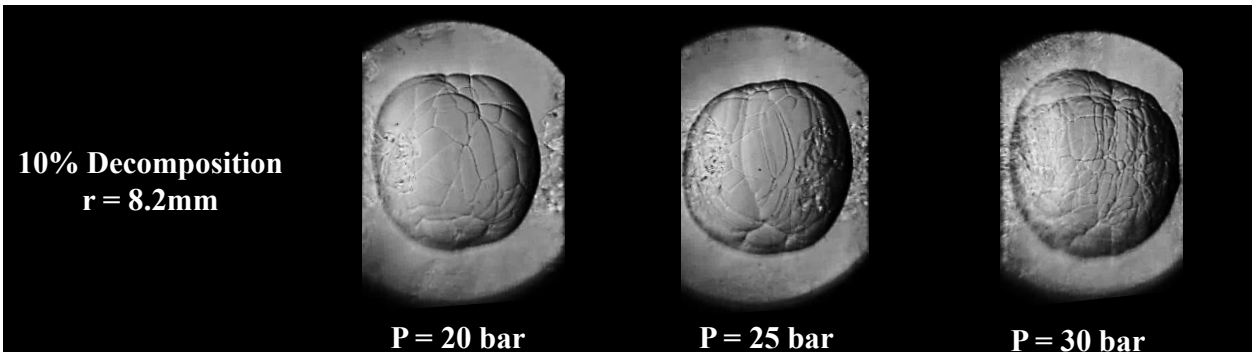

Figure 5.11: Pressure sweep of 10%D mixture all at ∼835 K. Lines indicate 1-D simulation results with varying mechanisms as shown in Chapter 4.

5.1.5 Perfect Flame Comparison

As previously discussed, with the current setup, a common problem and point of skepticism with RCM flames is the lobed morphology due to the non-spherical laser deposition and subsequent non-spherical kernel. Fellow colleagues in the combustion field often argue that the presence of these lobed within the kernel and flame artificially increase the flame surface area, leading to an overprediction of the flame speed, not representative of a true "laminar" flame.

To address this, the "normal" RCM flames were compared to a perfectly spherical flame, also measured in the RCM. Figure 5.12 compares this "perfect" laminar flame to the "normal" RCM flames, which contains the usual laser-induced lobes at the flame front. The "perfect" flame was unexpectedly done, likely due to a water film formed on the interior of the sapphire window. It was noticed that after multiple experiments, a thin film was deposited on the windows. In previous work in the RCM with heavy hydrocarbons, these thin films were seen on the windows after tests, likely due to soot formation. However, because there is no carbon, and water is a primary product of ammonia and hydrogen combustion, the only reason for this film is likely water. In this case, the water acted as a filter for the laser, essentially lowering the laser energy, resulting in a energy

deposition just barely above minimum ignition energy. As a result, this lowered the intensity of the plasma, resulting in a flame free of lobes.

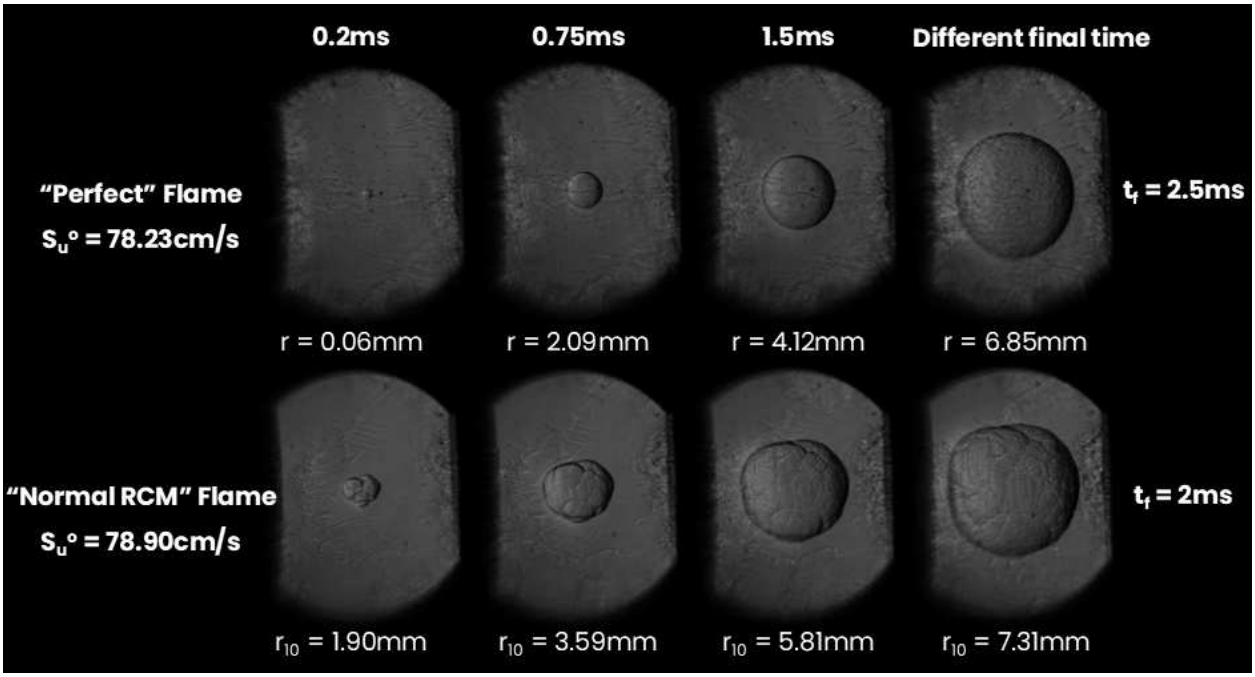

Figure 5.12: Flame propagation images of a "model" flame compared to a "normal" RCM flame containing instabilities and lobes from laser ignition.

Despite the visual differences in the flame surface and morphology, the measured flame speeds for both cases were nearly identical at ∼78.5 cm/s, which is significant, as it demonstrates that the lobes and wrinkles on the "normal" RCM flames do not significantly affect the final measured flame. Temporally, the initial flame kernel for the "perfect" flame is much smaller than its counterpart, however, the propagation rate is the same across the two cases.

This measurement provides justification and validates the use of the laser in this and previous studies. By demonstrating that the flame speed is independent of laser-generated lobes, the measured flame speeds here are equivalent to "laminar" flames at these conditions. This validates the mechanism validation as well, as the presented results are not due to laser-induced lobes and give insight onto chemical and transport properties of ammonia combustion.

5.2 Diesel Ignition Delay Times

To evaluate the ignition of ammonia-diesel dual-fuel combustion, as outlined in Sections 3.6 and 3.4.2, diesel droplet ignition delay time (IDT) experiments were conducted in the RCM at TDC thermodynamic condition of 880 K ad 20 bar. Five different mixtures were tested where three decomposition ratios (0%, 20%, and 40% at ϕ=0.5 assuming a 95%NH_3/5%Diesel energy percentage) and two pure hydrogen mixtures (ϕ=0.4, 0.5). 0-D ignition delay time simulations were also conducted in Cantera using the WUT [81], an ammonia/n-dodecance mechanism.

5.2.1 Ignition Delay Time Measurements

Figure 5.13 presents an example case of a 200 μm diesel droplet in a 20% decomposition mixture. The droplet is first injected into the chamber right before TDC, following an upward trajectory along the stagnation plane (a), b), c)). Upon TDC, the surrounding mixture reaches the high thermodynamic conditions (880 K, 20 bar), where the liquid droplet begins to vaporize, creating a vapor region around the liquid core of the droplet. Depending on the conditions and size of the droplet, the droplet usually falls due to gravity where diesel vapor is left behind, following the downward trajectory (d)). After a brief period of vaporization and mixing between the diesel and surrounding gas charge the mixture ignites at an assumed stoichiometric location, generating a flame (e)). Upon flame propagation, the flame follows the trajectory of the droplet because as the droplet falls, fuel-rich n-dodecane creates a mixture with the surrounding gas charge creating the lobed flame morphology (f)).

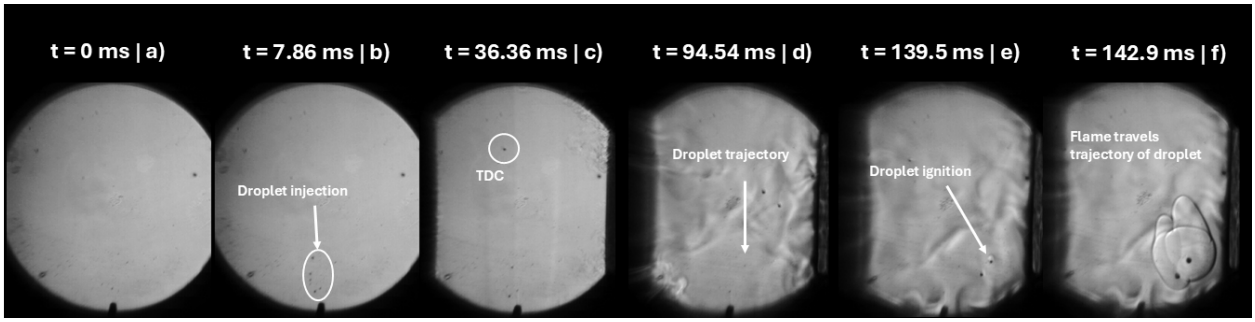

Figure 5.13: Process taken into measuring the droplet ignition delay time where a) represents the start of the video, b) shows the injection of the droplets, c) shows where the droplet may be at top-dead-center (where measurement begins), d) shows where the droplet trajectory between TDC and ignition, e) presents the droplet ignition point (end of measurement), and finally f) shows the flame morphology.

Comparing the IDTs of each premixed fuel presents several significant findings. It is believed that at higher oxygen concentrations in the premixed fuel the IDT becomes shorter, due to the interactions and initiation of combustion between the fuel and oxidizer. Before analyzing this data it is important to note that because of the current fidelity of the camera and the 1 pixel resolution, the droplets have a size range of $\sim \pm 40$ μm.

Figure 5.14 presents the measured ignition delay times as a function of the droplet diameter. The smaller droplets (< 100 μm) have the shortest IDTs, remaining below 20 ms. Here, the 40% decomposition case is the shortest, followed by 0% and 20% in order. Since 40% decomposition has the least amount of oxygen and most amount of hydrogen, the chemical kinetics is likely dominated by the diffusion of hydrogen out competing the reduction in oxygen (0% – 0.1843, 20% – 0.1799, 40% – 0.1756). Providing a hypothesis that due to the high mass diffusion rate of H_2, the H_2 may increase the reactivity of the mixture causing the mixture to ignite much faster than what is thought. With larger droplets (140–180μm), the trend inverts where 0% becomes shorter when compared to the other two. When becoming larger, the 0% mixture becomes the fastest, suggesting that at larger droplet sizes the ignition is dominated by the availability of oxygen in the surrounding mixture making the diffusion of hydrogen less important.

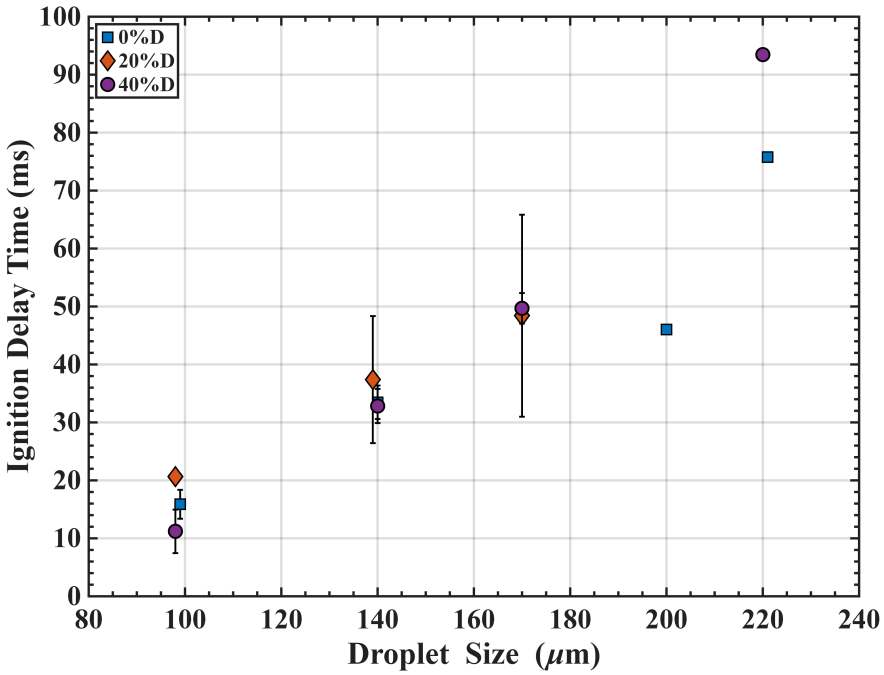

Figure 5.14: Droplet size sweep of ignition delay time measurements of ammonia-diesel droplets for 0%, 20%, and 40% at 20 bar and 880 K.

100% hydrogen cases were also measured and compared to the ammonia cases seen in Figure 5.15. Similarly to what is seen in the ammonia measurements and previous work with methane, as the droplet size increases, the IDT increases. In addition, the ϕ=0.4 case is faster than that of the 0.5 case, reinforcing the belief of the availability of oxygen. When directly comparing the decomposed ammonia mixtures to hydrogen, the IDTs remain relatively the same across the droplet size sweep, but are slightly slower. This indicates that the diffusion of hydrogen into the diesel vapor increases the reactivity and minimum ignition energy of the mixture.

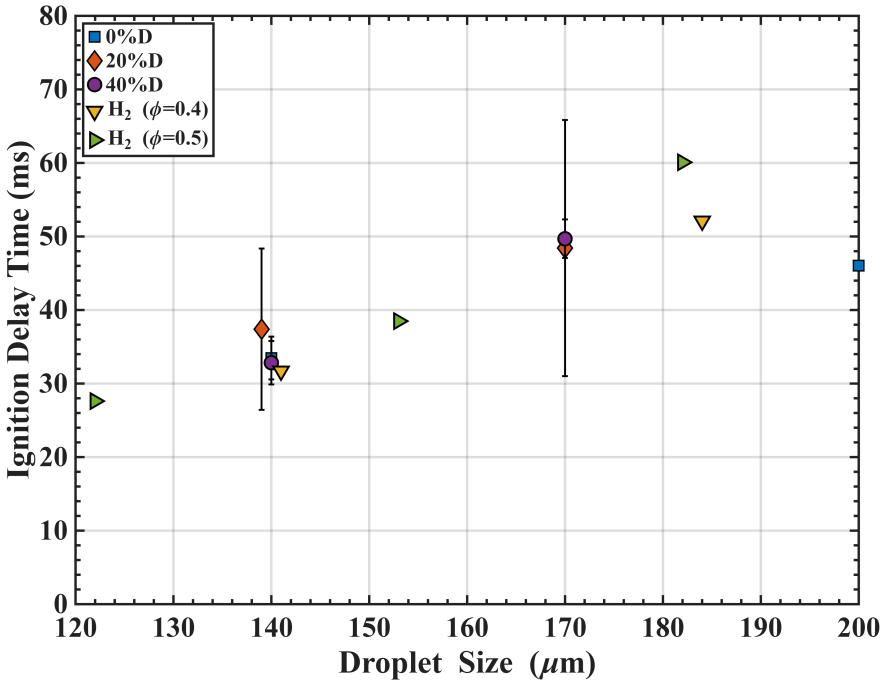

Figure 5.15: Droplet size sweep of ignition delay time measurements comparing hydrogen to decomposed ammonia mixtures.

To visualize and understand the kinetics behind ammonia decomposition on diesel ignition, the CounterFlowDiffusionFlame within Cantera was used to model the transport and chemical kinetics coupled with the IdealGasReactor to solve the ignition delay time. This setup is further explained in Section 4.2. To ensure high-fidelity among measurements, each mixture was measured at a 0.5 mm step. To save time on solving, only points with a sufficient amount of oxygen and subsequent equivalence ratio less than 10 were attempted to be solved for IDT.

Figure 5.16 presents the modeled diffusion and subsequent IDT measurements for each decomposed ammonia mixture. As the decomposition ratio increases, the equivalence ratio shifts. This is driven by the increased mole fraction of diffused hydrogen ad the subsequent reduction in oxygen. In addition, this shifts the ignition delay timing to the right as well. These do occur at increased equivalence ratios at approximately ϕ=6, showing that in these dual-fuel systems ignition is likely governed by the fuel rich conditions, not stoichiometric conditions.

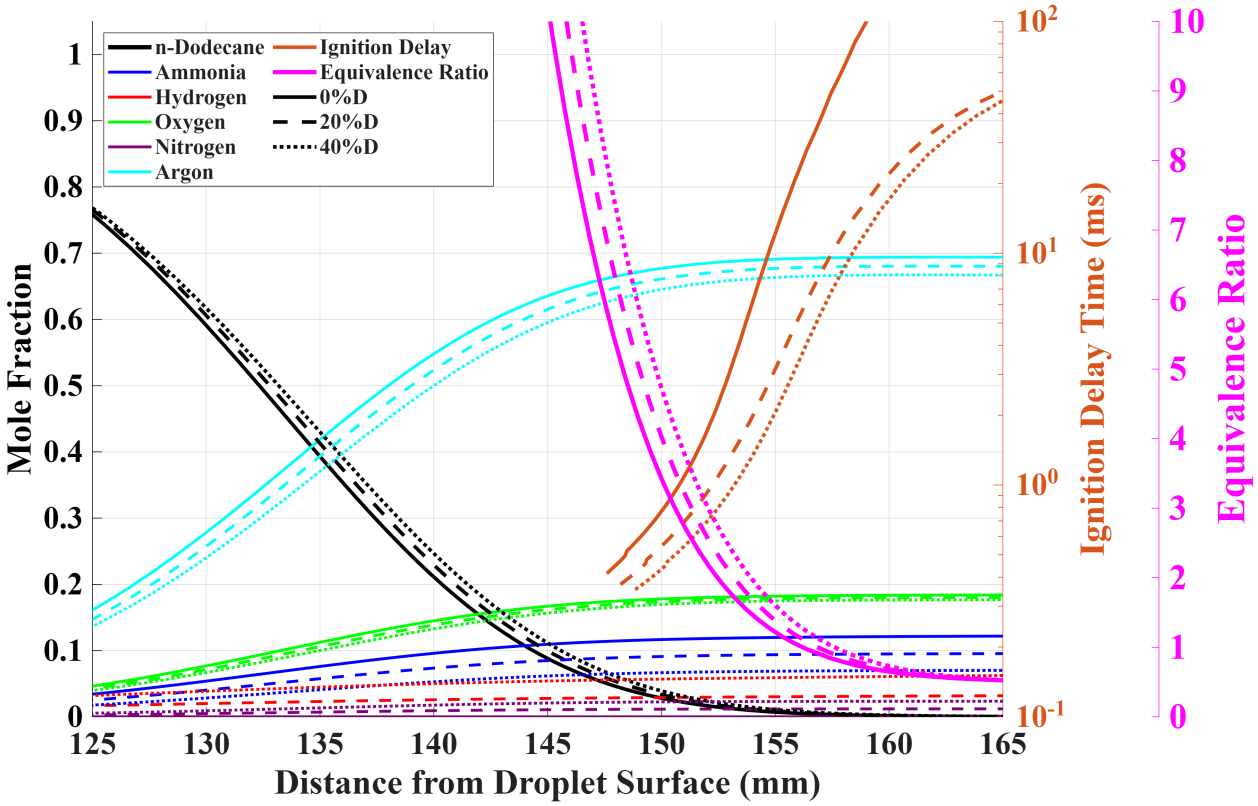

Figure 5.16: Modeled spatial profiles of diffusion of the premixed fuel mixture (decomposed ammonia at ϕ=0.5) into pure diesel $nC_{12}H_{26}$. This was modeled using a counter flow diffusion flame as explained in Section 4.2.

By normalizing the IDT and equivalence ratio about the 0% decomposition IDT, as shown in Figure 5.17, the spatial location of ignition of the 100 μm droplets was located on the graph. While the initial trends show a rightward shift in ignition location as the decomposition percentage increases, an inflection point is seen when looking at the 40% decomposition case. The ignition delay times for in order of spatial location are 0%, 40%, and 20% with IDTs of 15 ms, 10 ms, 20 ms, and equivalence ratios of ϕ=1.147, 0.706, 0.888.

This indicates that as the decomposition ratio increases beyond a certain threshold, the ignition location shifts towards the diesel-vapor region. These results show that ignition timing is likely a battle between the the presence of hydrogen and its minimum ignition energy (MIE) against the availability of oxygen in the mixture. This balance shows that the specific equivalence ratio and location of ignition is sensitive to the interaction between the diffusion of hydrogen and concentration of oxygen.

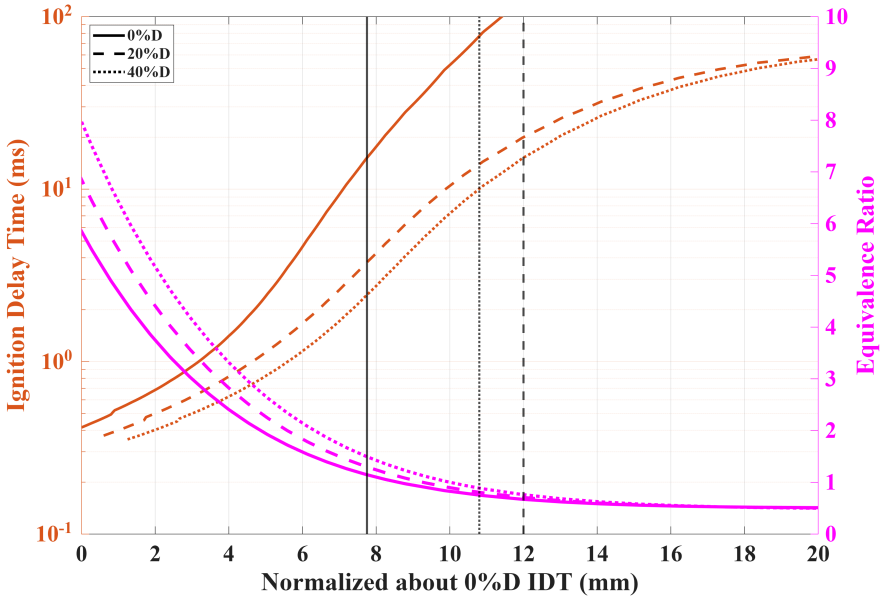

Figure 5.17: Normalization of the ignition delay time (IDT) and equivalence ratio about the 0% decomposition IDT from Figure 5.16. The black vertical lines represent the location at which the relevant IDT of each mixture at a 100 μm droplet ignites as seen in Figure 5.14. For each mixture, the relative IDT and equivalence ratio calculated are listed: (%D = 0%, 20%, 40% | IDT = 15, 20, 10 ms | ϕ=1.147, 0.706, 0.888).

This numerical study proves that the location of ignition and subsequent timing of ignition is coupled to the availability of oxidizer and hydrogen in the reactive environment. As the decomposition percentages increase, the diffusion of hydrogen determined earlier ignition, however, this is effect is determined by the local equivalence ratio and less oxygen concentration. This results in a leftward shift in the location of ignition towards the diesel.

5.2.2 Droplet Flame Morphology

Complementing the IDT measurements, the flame structure and morphology of diesel droplets were also reviewed. Unlike the laser-ignited flame speed morphologies seen in Section 5.1, these flames present unique flame developments due to the diesel droplet.

Figure 5.18 presents a 40% decomposition case throughout the entire droplet time frame within the RCM. Upon reaching TDC, the rapid pressure and temperature rise causes evaporation at the surface of the droplet, creating a diesel vapor surface needed for ignition and subsequent flame propagation. Unlike the laser-ignited flame kernels, these flames do not have lobed morpholo-

gies, presenting a smooth flame, similar to what is seen in the "model" flame in Section 5.1.5. Interestingly enough at the start of flame propagation, the flame exhibits a spherical and smooth morphology, however, approximately after 3 ms into propagation the surface of the flame contains cellular instabilities. This transition in the surface of the flame is characteristic of the high decomposed mixtures. The initial flame contains a large amount of liquid and vaporized diesel, constituting an effective Lewis number much greater than 1 (Le_{eff}>1) promoting a stable flame front. As the flame propagates into the hydrogen-rich premixed gaseous mixture, the effective Lewis number drops below 1 (Le_{eff}<1), which is more susceptible to cellular wrinkling (Section 5.1.1).

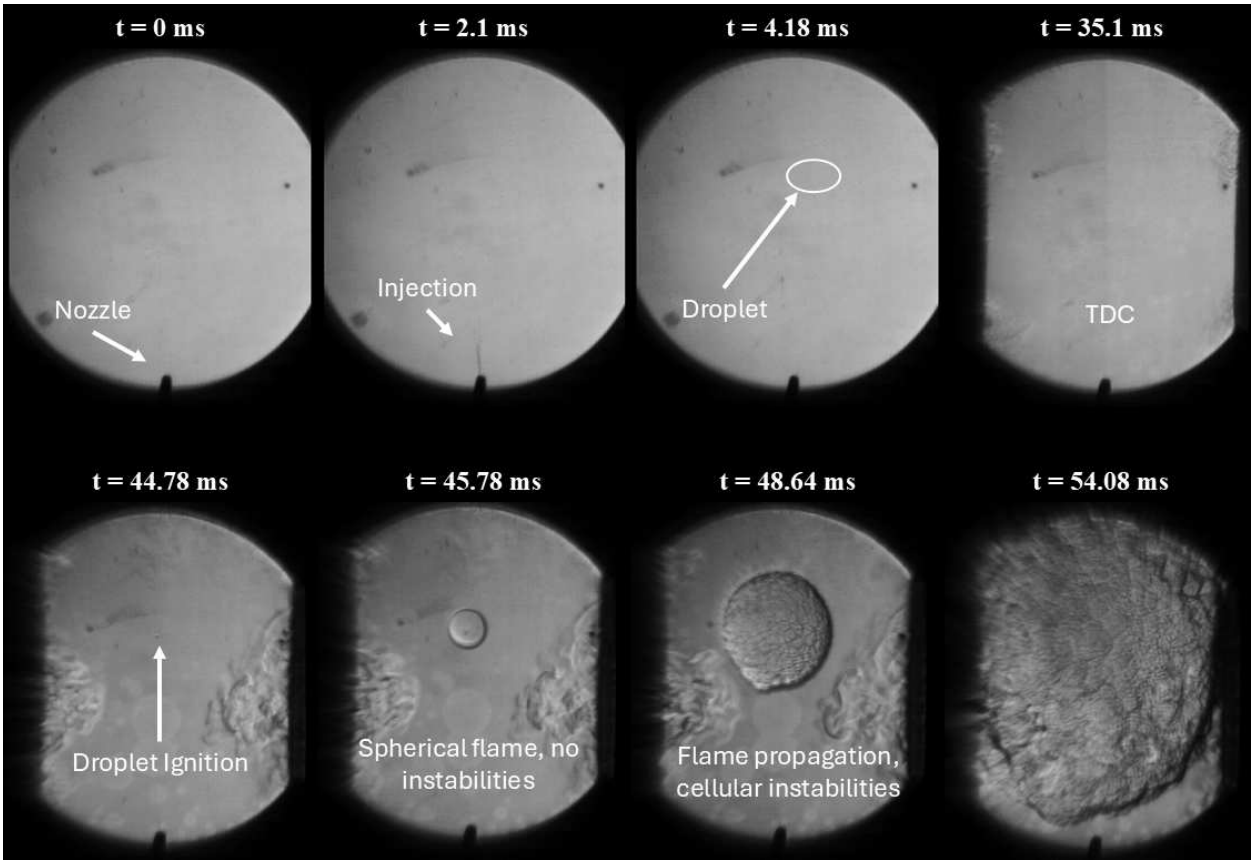

Figure 5.18: Flame propagation images of a "model" flame compared to a "normal" RCM flame containing instabilities and lobes from laser ignition.

To further show this phenomenon, Figure 5.19 compares the morphologies of the 0%, 20%, and 40% decomposition cases, all with a droplet size of 100 μm. The pure ammonia flame (0%) remains smooth and constant throughout the entire chamber, confirming in the absence of hydrogen, thermodiffusive instabilities are not an issue. The 20% decomposition case has a similar initial propagation than that of the 0% decomposition case as it travels down towards the bottom of the chamber. However, in the lower region of the flame, which interacts more with the premixed fuel, slight cellular instabilities are apparent. Between these flames, at 0% and 20% decomposition the flames follow the direction of where the droplet traveled, but that is not the case in the 40% case. This is likely due to the minimum ignition energy and flame speed of the fuel, as the flame becomes faster and more radicals are produced the flame does not follow the direction at which diesel once was.

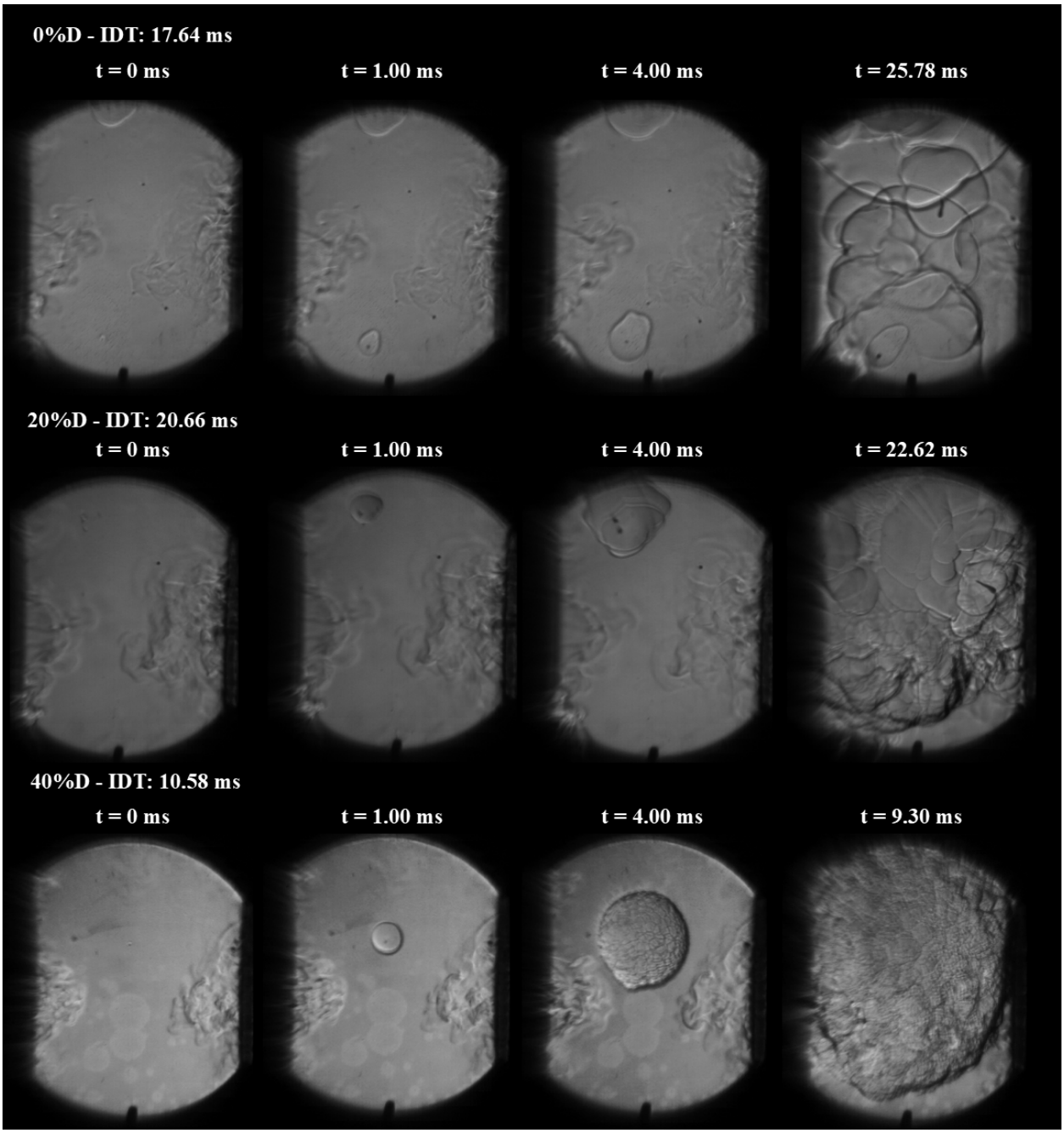

Figure 5.19: Droplet flame morphology images for 0%, 20%, and 40% decomposition, showing initial droplet ignition and subsequent flame propagation.

CHAPTER 6 – COMPUTATIONAL RESULTS

This chapter will cover three-dimensional computational fluid dynamics (CFD) results, focusing on reviewing the flow field, pressure, and apparent heat release rate (AHRR) for chemical kinetic validation. The rapid compression machine (RCM) serves as a critical benchmark for combustion modeling. Because of it simple geometry and well-defined boundary conditions and flow, it provides a way to asses mechanisms at these conditions, similar to engine simulations. If current CFD frameworks and mechanisms are incapable of predicting the pressure traces and combustion phasing seen in the RCMs controlled environment, they will likely not be able to predict internal combustion engines for production, as complex turbulent, geometry, and access to the engine prevent the use of ammonia-powered energy systems. CFD setup and preliminary simulations can be found in Section4.3.

6.1 Offset Effect on Bulk-Flow

As detailed previously in Sections 2.1.1 and 5.1.2, piston offsets are an unavoidable and uncontrollable event in the RCM, driven by friction in the seals and variability in the hydraulic pressure. While the RCM is equipped with creviced pistons, designed to suppress roll-up vortices, creating a quiescent environment is ideal. However, both experimental and CFD confirm that bulk-flow gas motion remains negligible below the 6 ms offset. As illustrated previously, measured flame speeds remain highly repeatable below the 6 ms offset cutoff, giving a maximum standard deviation of 5.17 cm/s. The exponential fit used in Figure 5.4 demonstrates this effect of bulk flow on the flame front.

To quantify this bulk flow - not achievable in experimental testing - the velocity flow field of the chamber was visualized in post-processing from CFD simulations to validate the quiescent flow assumption. Using the 20% decomposition case, combustion was turned off within the simulation to solely simulate the flow within the RCM, sweeping offsets. A velocity probe was placed in the geometric center of the chamber (0,0,0), monitoring the velocity magnitude at this point throughout

the entire simulation. Figure 6.1 shows an example of this. Within this framework, the magnitude of the velocity at TDC and time frame from the spark till the end of flame propagation of most mixtures was analyzed (0.2, 0.7, 1.5, and 2.5 ms post laser ignition).

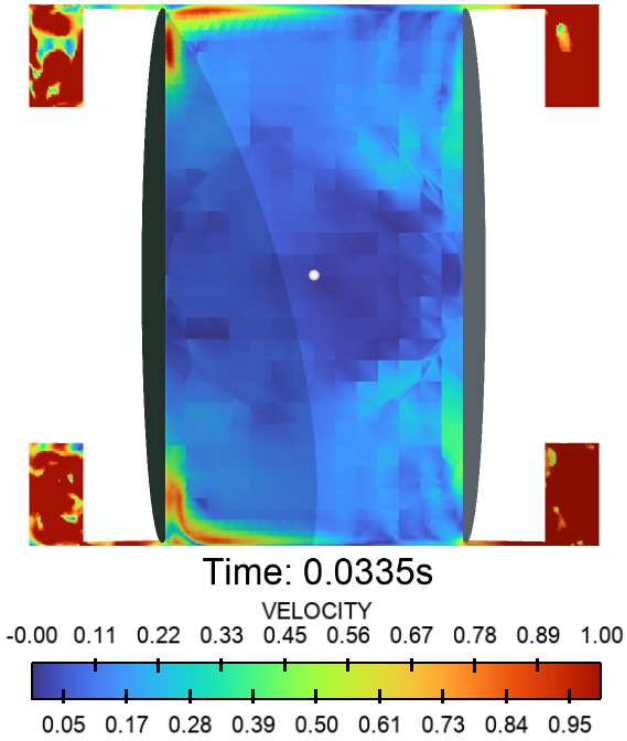

Figure 6.1: Example of post-processing where a velocity probe is inserted into the middle of chamber, measuring the velocity magnitude at that node. The velocity probe is represented by the white circle in the middle.

As shown in Figure 6.2, simulations within the 6 ms offset window had a maximum velocity of only 6 cm/s within this window. To contextualize this, the slowest flame seen in experiments (0%D, 760 K, 25 bar) is approximately 200 cm/s (not corrected for density). Interestingly enough, this maximum velocity is achieved by the 0 ms offset case, not at 3 or 6 ms. As a result, the bulk-flow induced at offsets less than 6 ms is roughly two orders of magnitude lower than the flame propagation rate, confirming that the central reaction zone is quiescent. The 9 ms offset case ranges from $\sim$12-17 cm/s which is still relatively low when compared to the experimental values. However, this just takes into account the velocity seen in the middle of the chamber, as there is likely vortex formation near the pistons where the flame propagates.

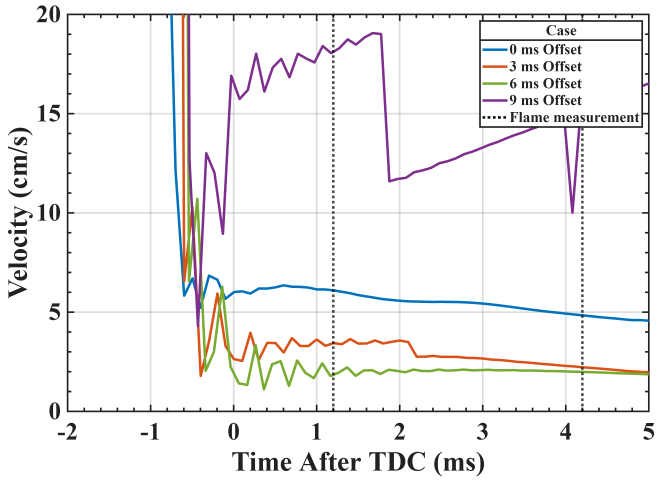

Figure 6.2: Plots of the variation of the velocity in the middle of the chamber. This is located directly in the middle of the chamber using a probe to measured the magnitude of the velocity at this point. The dotted lines represent the time frame at which the flame is measured experimentally.

Building on the experimental case shown in Section 2.1.1 (Figure 5.5), the flow field was visualized and investigated to understand the reason to the flames transitioning to a turbulent flame. As previously explained, high offsets induce a turbulent flame not at the chamber center, rather in the regions closer to the pistons.

To visualize this, Figure 6.3 illustrates the velocity field within the chamber at TDC, spark timing, and the subsequent flame measurement time frame. These results reveal "tumble" vortices originating at the left piston wall in the 9 ms offset case. Within this tumble, the velocity magnitudes range from ∼50–80 cm/s, which is significant as this velocity is approximated 25%–40% of the propagation rate of the slowest flame measured (200 cm/s). This provides a clear reason as to why the flame is overtaken by turbulence in these high offset cases.

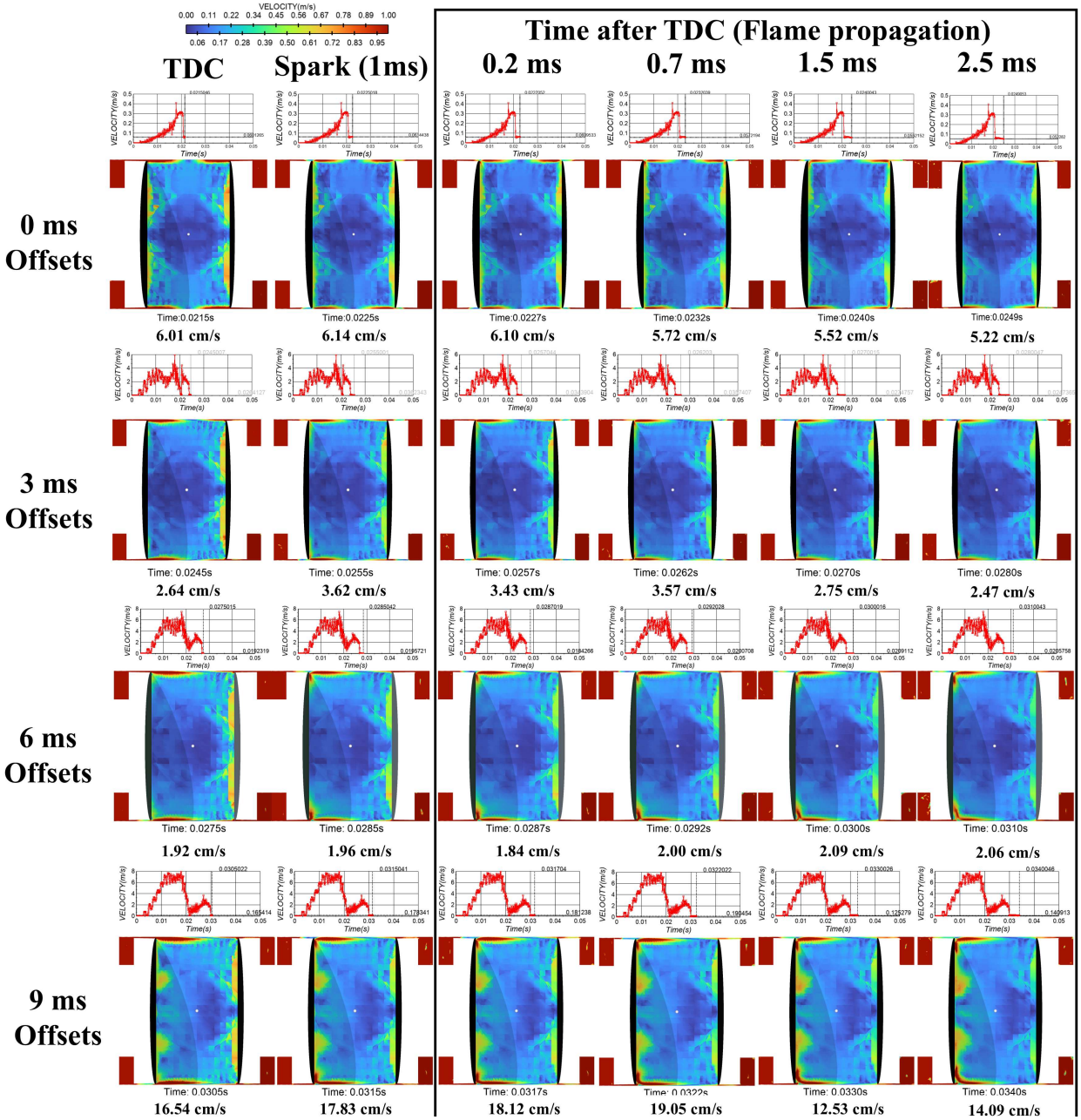

Figure 6.3: Velocity field within the combustion chamber, monitoring TDC, spark time, and subsequent flame measurement window. Plots above the flow field represent the velocity trace located at the white probe in the middle of the chamber.

In contrast, the other cases (< 6 ms) confirm that these tumbles do not form. While minor variations in the flow field are seen at the 3 ms and 6 ms cases, along the right side boundary, the central region of the chamber remains quiescent. These CFD simulations confirm that the turbulence and tumbles generated by offsets only affect the flame at offsets higher than 6 ms.

To further understand the effect of bulk flow on the flame, the flame morphology was evaluated at the 0 ms, 3 ms, and 6 ms offsets in a reacting case, unlike what is shown previously. Figure 6.4 presents the simulated flame morphology, visualized using the adiabatic flame temperature isosurface.

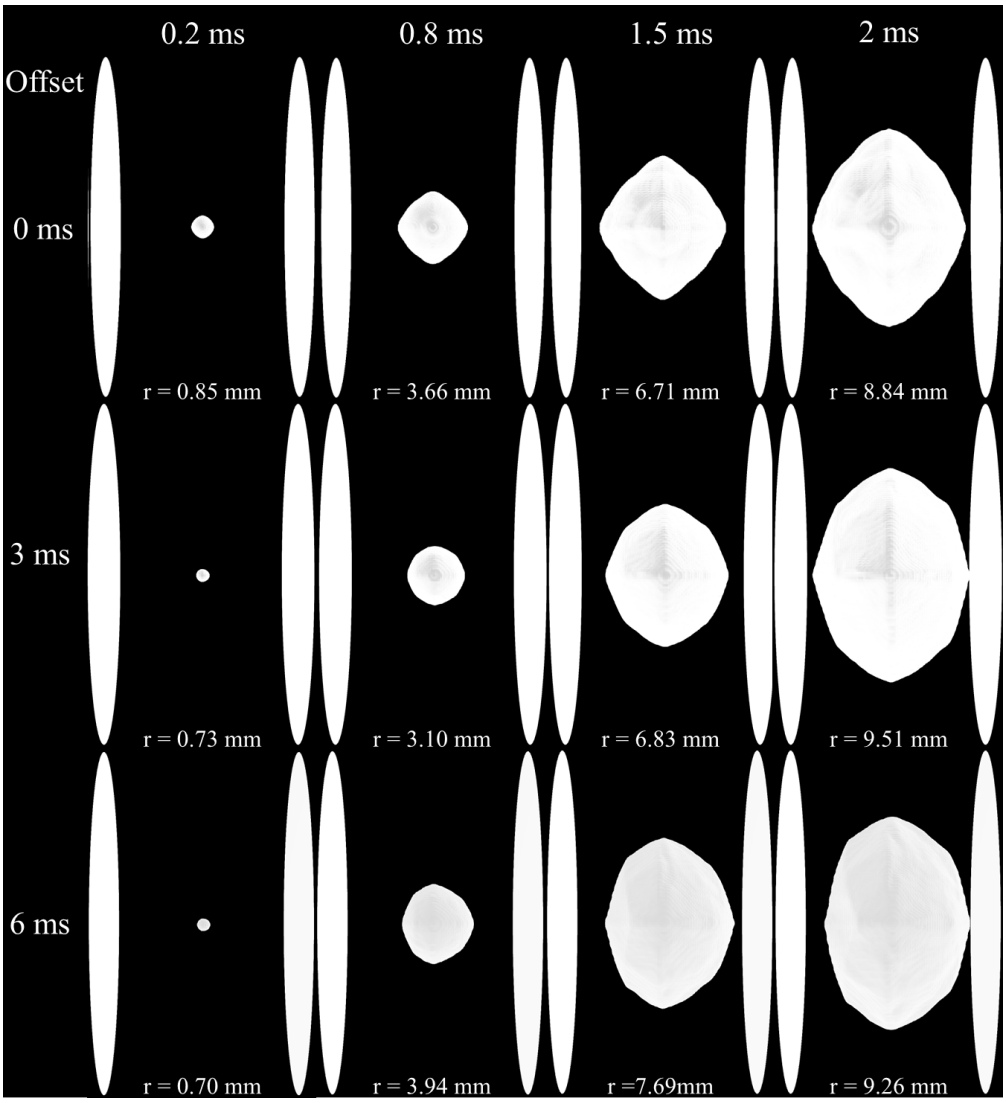

Figure 6.4: Flame morphology of each simulated offset at 0, 3, and 6 ms offsets fo 20% decomposition mixtures.

As the offsets increase, the flame slowly creeps towards the right piston. This motion is consistent with the non-reacting case seen previously, where as the tumble formed neat the left piston induces a flow field pushing the reaction zone or flame towards the opposite piston. Despite this

movement, the growth rate of the flame remains stable across the offsets. When measuring the radius of the flame kernel the radius remains relatively constant across the 0 ms to 6 ms offset range, with slight deviation seen at 1.5 ms and 2.0 ms. The change here is around 0.8 mm indicating a slight acceleration, however, it seem s the impact on the flame speed is negligible given this.

6.2 Offset Effect on Thermodynamic Conditions

A primary concern in RCM testing is whether the piston offsets affect the thermodynamic TDC states at the point of ignition. While it is expected that this delayed compression will lead to heat loss and non-ideal behaviors, the experimental data seen in Chapter 5 (Table 5.1) shows that the largest deviation in the temperature to be only 5.05 K across all valid test points.

To isolate whether this temperature variance as a function of offset makes a difference, the simulations maximum temperature within the chamber was taken. The 20% decomposition case at the highest experimental temperature point was test with a range of offsets (0 ms, 3 ms, 6 ms, and 9 ms) with no combustion, the same simulation as in Section 6.1.

As depicted in Figure 6.5, the simulated temperature differences at each TDC point between all cases has a maximum difference of $\sim$3 K, between the 0 ms and 6 ms offset case. This change is less than the maximum variance seen in the experimental dataset, confirming that the piston offset does not cause large deviation in the thermodynamic states at TDC.

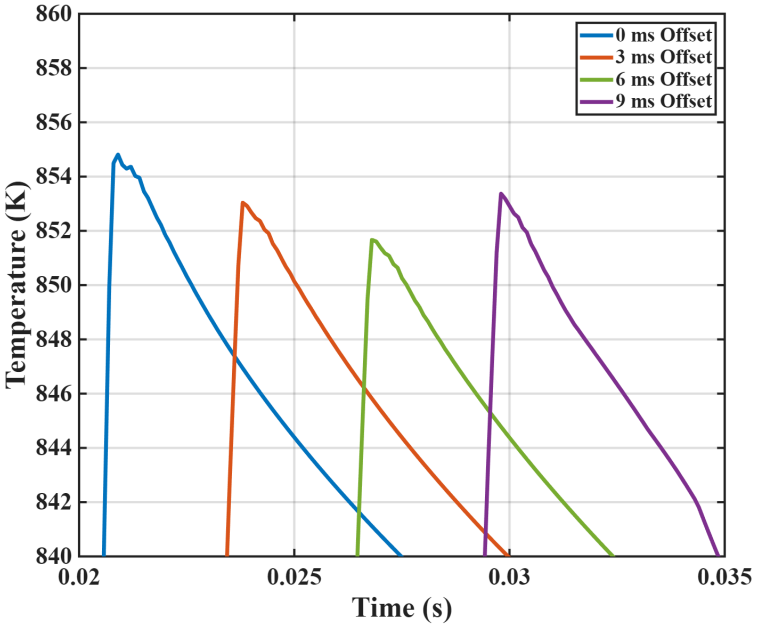

Figure 6.5: Temperature variation based on range of offsets using the 20% decomposition mixtures at $T_i = 60°C$. The temperature plotted is the maximum temperature seen in the chamber. The maximum at each point is where the simulation hits TDC.

This finding confirms the isentropic relation calculation remains correct for each experimental trace no matter the offset. Even with the slight deviation between the offsets, the adiabatic compression assumption holds even with high offsets.

6.3 Mechanism Effect

To evaluate the predictive capability of mechanisms, 3-D simulations were performed across all ammonia decomposition fractions (0–42.5%) and the baseline methane case, with thermodynamic states at the highest temperature conditions (∼840 K and 25 bar).

The C3 (34 species, 242 reactions), representing an industry-standard, CFD-optimized mechanism, and the Han mechanisms (32 species, 171 reactions), the most accurate mechanisms in 1-D simulations, specifically tuned for laminar flame speeds (Table 4.1). By comparing these mechanisms, a baseline is established for the current state of kinetic modeling, demonstrating how sensitive combustion predictions are to mechanism selection at these thermodynamic and hydrogen-rich conditions. Performance of each mechanism is largely based on the comparison of the experimen-

tal traces to the simulated traces for both pressure and apparent heat release rate (AHRR). All experimental traces were taken from cases with offsets less than 0.3 ms.

6.3.1 CFD Pressure

Figure 6.6 compares the experimental and simulated pressure traces. Both mechanisms accurately predict the compression stroke, capturing the pressure rise to TDC and the subsequent heat loss associated with the boundaries. The 0–20% decomposition percentages match the TDC pressure well, however, the methane and 42.5% cases slightly overpredict the TDC pressure, likely due to experimental error from gas blow-by or leaks within the chamber. As the decomposition percentage increases, a leftward shift of the pressure rise is observed for both mechanisms, with respect to the experimental trace. For example, with the C3 mechanism, moving from 0% to 10% the rapid pressure rise shifts to the left and continues as the decomposition is increased. The reason for this is likely due to the mechanisms capability to not correctly model hydrogen combustion, as hydrogen concentration is increased, the model has a more difficult time modeling the combustion phase causing divergence from the experimental traces.

In these simulations, the flame-quenching model was used, significantly improving the end-of-combustion (EOC) pressures in previous simulations as explained in Section 4.3.5. While experimental traces show a decline in EOC pressures with decreasing decomposition percentage - which is a result of the higher adiabatic flame temperature and higher energy release seen in hydrogen-rich mixtures - the simulated curves show a constant EOC across all mixtures (excluding CH_4 and 42.5%). While the mechanisms are not perfectly modeling this EOC, the integration of the flame-quenching model gives more accurate results.

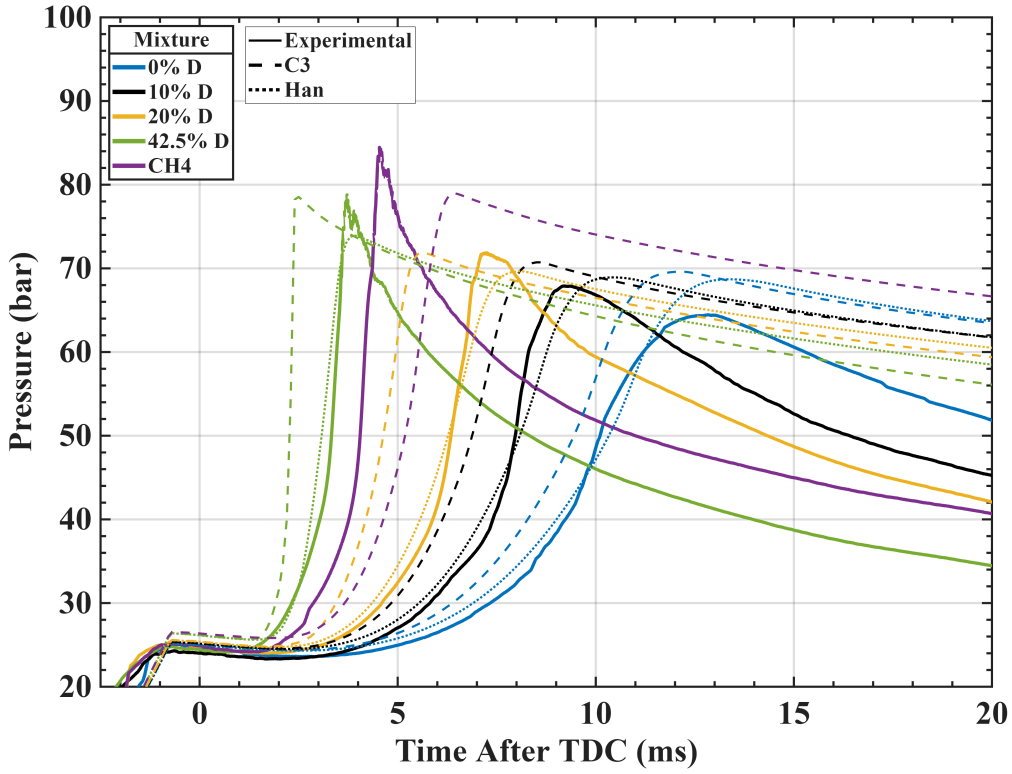

Figure 6.6: CFD pressure traces against experimental traces for all mixtures at ∼840 K and 25 bar, comparing the Han and C3 mechanisms.

Directly comparing the rapid pressure rise reveals significant trade-offs between the ignition phasing and the late-stage combustion kinetics. The Han mechanism consistently matches the initial pressure rise, aligning with the experimental pressure trace. However, as the flame propagates throughout the chamber and chemical energy is converted toward the peak heat release rate, the Han mechanism models a slower pressure rise than that seen experimentally. This is likely a result of the complex-flame wall interactions and the high-temperature/pressure chemistry dominating this end-of-combustion phase. In contrast, the C3 mechanism overpredicts the initial ignition phasing. For example, at 10% decomposition, C3 models the onset of rapid pressure rise ∼1 ms earlier than the Han mechanism. However, in the late-stage combustion combustion, C3 models the experimental pressure gradient better than Han. As the C3 and experimental traces are parallel, the high-temperature/pressure chemistry and transport properties are more robust than that of its counterpart.

6.3.2 CFD AHRR

The apparent heat release rates (AHRR) for the simulations are presented in Figure 6.7, compared against the experimental AHRR traces calculated using the derivation detailed in Section 3.7. Since the heat release rates are derived directly from the pressure gradient, the ignition phasing are the same as seen in Section 6.3.1.

Simulated heat release rates are generally lower than that of the experimental trace for both mechanisms (excluding C3-42.5%). All low decomposition cases exhibit a less aggressive rise and peak heat release rate than that of the experimental traces. Among the two mechanisms, the C3 mechanism produces the closest peak heat release rate than the Han mechanism, resulting in a faster pressure rise rate, parallel to the experimental pressure trace seen previously.

This under prediction in the heat release rate suggests that the numerical models and mechanisms struggle to fully capture the full energy release and chemical conversion during combustion. As previously explained, this difference between the two mechanisms is likely due to the mechanisms ability to model this late-stage combustion behavior and high-temperature/pressure kinetics and/or complex flame-wall interactions.

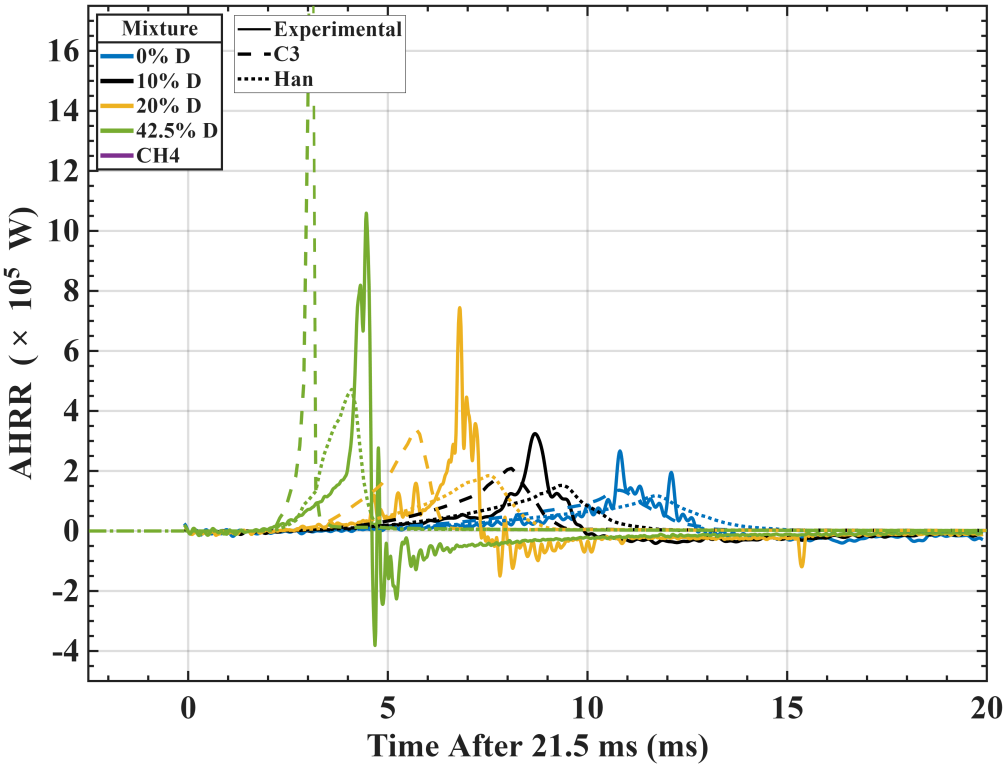

Figure 6.7: CFD apparent heat release (AHRR) traces against experimental traces for all mixtures at ∼840 K and 25 bar, comparing the Han and C3 mechanisms. 0 ms represents the time at TDC.

Another reason for the lower heat release rates is the potential end-gas autoignition triggered by reactants trapped within the piston crevices. Because of the addition of the flame-quenching model inhibiting combustion in the crevices, there is no combustion there. However, experimental peak pressures and increased AHRRs suggest that partial burning of the gas trapped in these regions is possible. Nevertheless, it is important to note that these deviations in the AHRR manifest significantly after the flame speed measurement window. Therefore, while there are discrepancies in the chemical kinetics, this does not invalidate the measured experimental flame speeds presented in Section 5.1.

A notable outlier in the simulations is the 42.5% decomposition C3 case, significantly overpredicting the maximum heat release rate. This is unique to the hydrogen-rich mixture and not seen in the lower decomposition mixtures. This suggests that while the C3 mechanism is more accurate at lower decomposition ratios, it lacks the correct chemistry for late-stage hydrogen-rich combustion.

6.4 Offset Effect

To evaluate the effects of offsets on the combustion in CFD, the 20% decomposition mixture at the highest temperature condition (∼840 K and 25 bar) was simulated ranging the offsets at 0, 3, and 6 ms. To simulate these offsets, the motion $.in$ file for the left piston was increased by 3 ms resulting in it coming 3 ms after the right piston.

Figure 6.8 illustrates the sensitivity of the 20% decomposition case to the given offsets. Because the spark-timing of each offset case is slightly different, this timing was normalized to where the laser is fired, 0 ms. The computed pressure traces from here are almost identical, demonstrating the the fundamental propagation time frame is insensitive to offsets in simulated cases. However, these are slightly phased to the left with respect to the experimental traces.

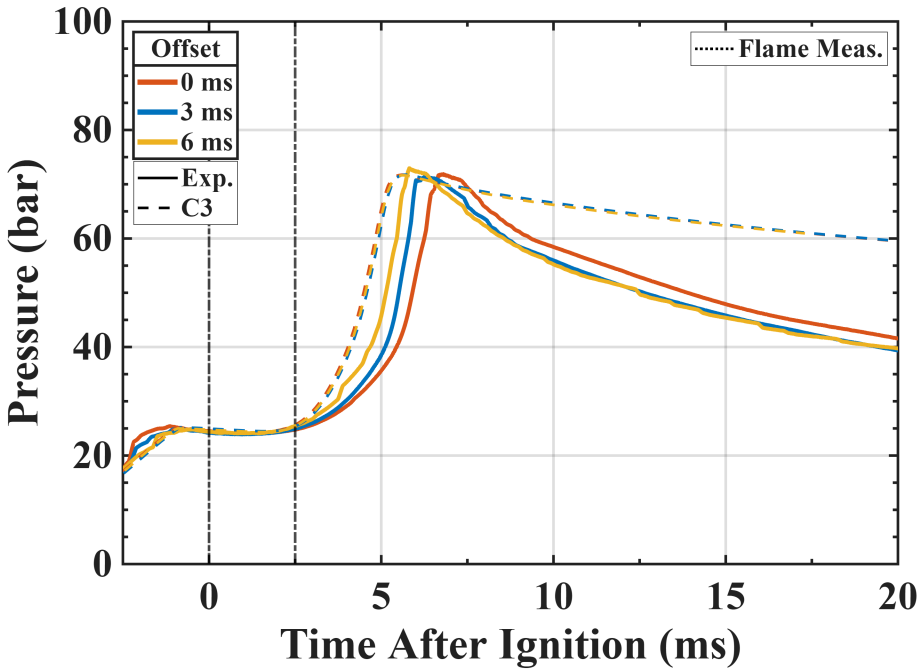

Figure 6.8: Offset pressure traces of CFD simulations compared to experimental traces using the C3 mechanism at 20%D and the highest temperature case. The dotted lines represent the location at which the flame is measured in experiments.

While the numerical simulations provide the same pressure traces, shifting is seen in the experimental pressure traces: as offsets decrease towards 0 ms, the onset of combustion shifts to the

right. This phenomenon is likely attributed to the bulk-gas motion generated as a result of the offsets as explained previously in Section 6.4. Because of the bulk-gas motion that is at the sides of the piston and chamber (seen in Figure 6.3), this induces more mixing and turbulence into the chamber, increasing the rate of conversion from chemical energy to thermal energy, promoting late-stage combustion. Regardless, the pressure traces in the flame measurement window remain the same, further proving that the offsets do not have an effect on the flame speeds and that the 6 ms cutoff is sufficient for accurate data.

6.5 CFD Flame Morphology and Measurement

To continue to validate the capability of the CFD model and mechanisms, the simulated flame propagation was visualized using a temperature isosurface of the adiabatic flame temperature. By using an updated version of the flame speed measurement code as described in Section 3.5 and implemented in Section 5.1, the flame speeds of the isosurface's were measured. To ensure consistency among measurements, the measurement time frame used in experiments was used in CFD, unless the flame was too fast (42.5% decomposition case).

Figure 6.9 shows a comparison of the flame morphologies between the 10% decomposition experimental case to the C3 and Han mechanisms. The simulated kernels are significantly smaller than that of the experimental flame and subsequently during the rest of the flame propagation. This is likely attributed to the ideal spherical radius used in the model, lacking the plasma physics, shock-wave generation, and lobed non-spherical flame development characteristic of the experimental flame.

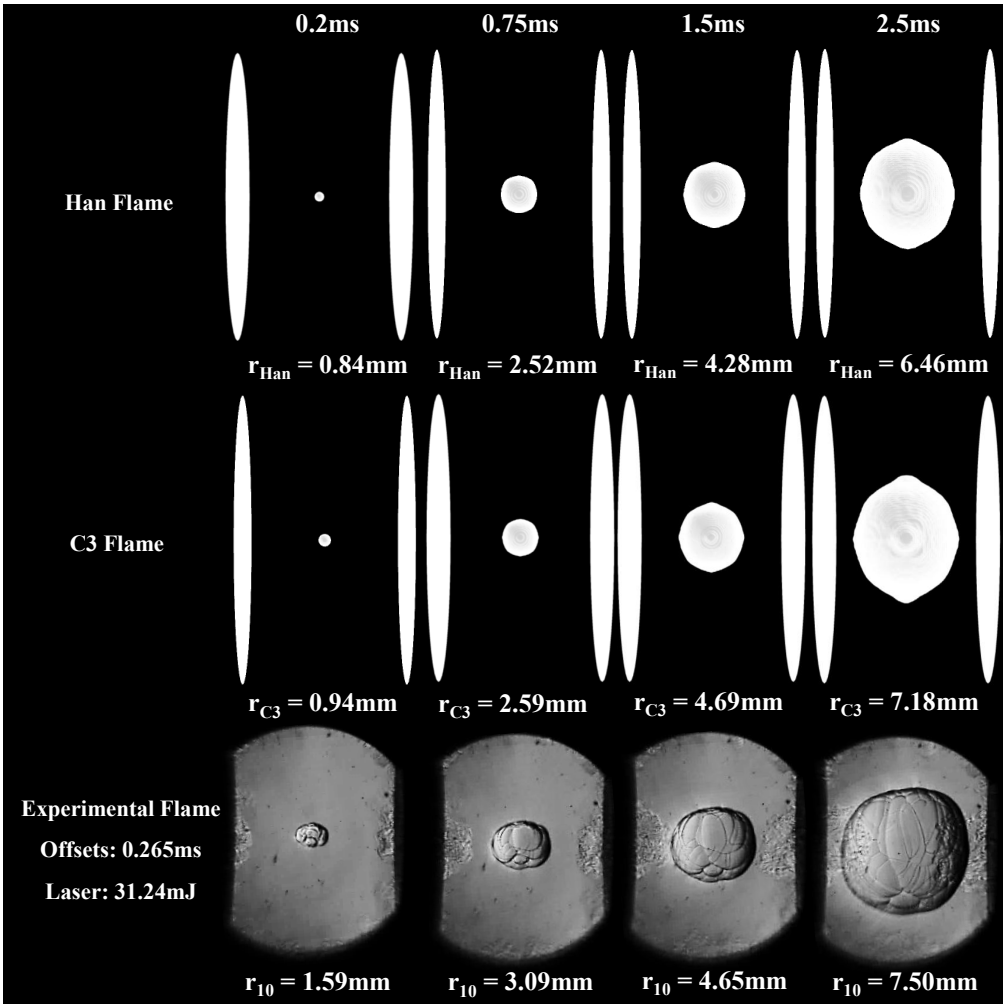

Figure 6.9: Flame morphologies of Han and C3 mechanisms compared to experimental case at 10% decomposition, 25 bar, and 840 K.

Nevertheless, similar flame development is between the two simulations until 1.5 ms. Beyond this time, the C3 flame mechanisms flame propagation increases, having larger radii. In addition, beyond this time, both simulated flames exhibit stretching parallel to the piston faces, likely induced by the volume constraints and piston walls in the 3-D mesh that are not seen in the experimental morphology.

Table 6.1 presents the measured CFD flame speeds across all mixtures. These values are reported alongside the experimental and 1-D flames in Cantera. For the 0% and 10% decomposition cases, both the Han and C3 mechanisms accurately measure and agree with the experimental

values. Between the two mechanisms, Han has better agreement with the experimental points at ∼2 cm/s and ∼6–13 cm/s for C3. However, at higher decomposition ratios (20%D), while the Han mechanism remains relatively close to experimental values (∼5 cm/s difference), the C3 mechanism significantly overpredicts the experimental case by around 30 cm/s. At 42.5% decomposition, both mechanisms heavily overpredict the measured flame speed. Here Han overpredicted by ∼90 cm/s where as C3 overpredicted by ∼250 cm/s. Given the geometry output of the CONVERGE simulations, only 7 frames were used to measure the flame speed, whereas experimental points had around 75 frames. The fidelity of these results may be greatly affected by the amount of frames used for measurement. This confirms that both mechanism, especially C3, fails to resolve the transport of hydrogen-rich ammonia combustion at these thermodynamic states.

Table 6.1: Comparison of experimental, 3-D CFD, and 1-D simulation flame speeds.

Mixture/Mechanism	Experimental	CFD	CONVERGE 1-D	Cantera 1-D
0%D – C3	51.32	57.85	59.45	58.51
0%D – Han	51.32	53.68	54.16	53.29
10%D – C3	67.71	80.30	75.54	72.27
10%D – Han	67.71	69.98	70.27	66.63
20%D – C3	89.33	121.54	97.67	90.36
20%D – Han	89.33	94.09	93.04	85.13
42.5%D – C3	206.69	459.23	184.38	157.93
42.5%D – Han	206.69	292.72	185.86	156.74
CH_4 – C3	158.92	123.69	-	164.73

It is expected that the calculated flame speeds between 1-D and 3-D simulations would yield relatively similar results, as seen in the 0% and 10% decomposition flames. However, as demonstrated in high decomposition ratios in Table 6.1, this is not the case. This discrepancy and overprediction is likely attributed to the transport models used in each solver. As explained previously in Chapter 4, CONVERGE uses the mixture-averaged transport model, providing an acceptable tradeoff between accuracy and computational cost and the multicomponent method was used in Cantera 1-D simulations.

As seen in Figure 6.10, these two solvers predict increasingly different results as decomposition percentage increases. In addition, the Chemkin software was added as a comparison case, as it is a commonly used software in industry and research [91].

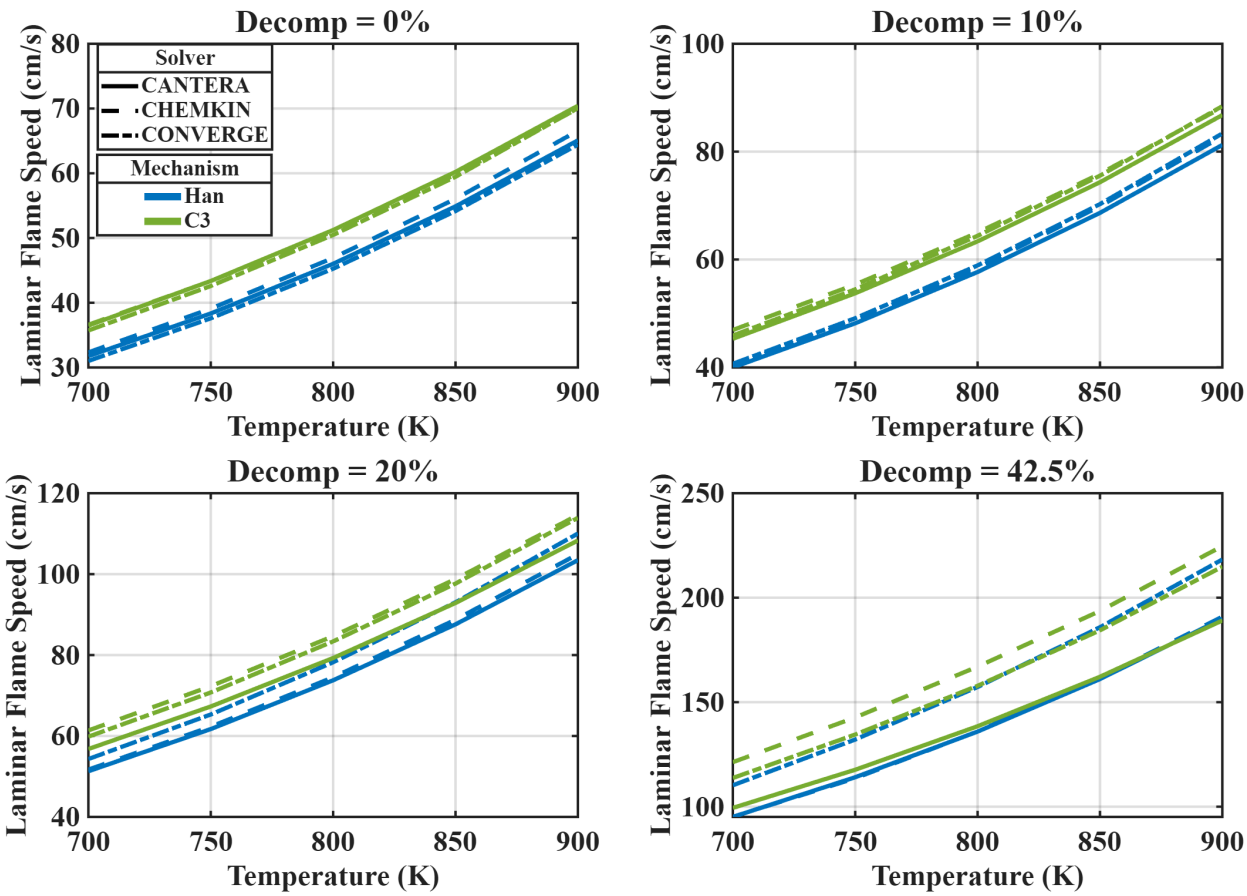

Figure 6.10: Comparison of commonly used 1-D solvers with different transport models. In these simulations Cantera uses the multicomponent model, CONVERGE uses mixture-averaged, and Chemkin [91] uses multicomponent as well. 0%, 10%, 20%, and 42.5% decomposition were all simulated across all software.

Both the 0% and 10% decomposition cases yield similar results across the temperature sweep. Reaching the 20% decomposition the solvers begin to diverge. Strictly comparing CONVERGE against Cantera, CONVERGE begins to diverge away from the Cantera measurements, especially with the C3 mechanism solving faster flames. Within this analysis, the only parameter changing is the software and its respective transport model. It highlights that the overprediction seen in CFD is a result of not only the mechanism, but is also due to the limitations in modeling mixture-averaged

transport in resolving highly-diffusive species present in these hydrogen-rich mixtures. To model this accurately, either multicomponent is needed in the CONVERGE framework, or higher-fidelity direct-numerical-simulations (DNS) is needed.

CHAPTER 7 – CONCLUSIONS AND FUTURE WORK

7.1 Flame Speed Conclusions

This study presents the first set of flame speed measurements of decomposed ammonia mixtures at 0%, 10%, 20%, and 42.5% decomposition ratios (with the 42.5% case identified as a mixture constituting flame speeds similar to that of methane) at engine-relevant temperature and pressure combinations (760–850 K and 20–30 bar). Experiments were conducted at an equivalence ratio of ϕ=1 and demonstrated a monotonic increase in flame speeds with temperature and decomposition percentages, with an average increase of 25.5$\pm$2.7% increase per 10% increment in decomposition percentage.

This novel data set was compared against eight chemical kinetic mechanisms. The NUIG and Han mechanisms provided the closest agreement with experimental data. At low decomposition percentages, most mechanisms overpredicted experimental measurements, whereas at the high 42.5% decomposition, the predictability flipped. While preliminary simulations suggested similar flame speeds for methane and 42.5% decomposition, the experimental values measured flame speeds up to 60 cm/s faster than the simulated values at the peak temperatures. These discrepancies in modeled and experimental values present a limitation in current chemical kinetic modeling, where the inability to capture the high temperature kinetics and transport of hydrogen-rich containing fuels and/or the role of thermodiffusive instabilities on promoting flame propagation

High-speed schlieren imaging confirmed that while laser-induced ignition lobes were present, measured flame speeds were unchanged when there were not lobes. Cellular instabilities were observed at increased %D and increased pressure, likely having a promoting effect on flame propagation. This promotion of the flame propagation by thermodiffusive instabilities suggest that the experimental flame speed measurements are enhanced by these cellular and hydrodynamic instabilities, which cannot be modeled in 1-D and 3-D CFD simulations.

Using 3-D CFD, the RCM was modeled across all decomposition mixtures at 25 bar and 840 K , revealing discrepancies in modeling predictions. Initial simulations significantly overpredicted end-of-combustion (EOC) pressures, a problem fixed by modeling flame-quenching at the piston interface. While the simulations accurately predicted the compression stroke and rise to TDC, combustion phasing varied with mechanism and decomposition percentage. The Han mechanism matched the initial pressure rise during combustion, whereas the C3 mechanism failed to predict the onset of combustion accurately but remained parallel to the experimental traces. The divergence of the measured flames and pressure traces in CFD at high decomposition percentages, likely due to the use of mixture-averaged transport and current mechanisms in modeling hydrogen-rich mixtures.

Despite the modeling challenges, these results suggest that lower levels of ammonia decomposition may enable similar engine performance seen in existing natural gas spark-ignited engines. At stoichiometric conditions, 42.5% decomposition exceeds the methane baseline, a 30–40%D is more suitable for retrofitting natural gas engines. While flame speeds present one critical combustion parameter within an internal combustion engine other metrics like knock tendencies, emissions, and ignition should be investigated.

These findings highlight that current mechanisms and common CFD strategies fail to capture key aspects of ammonia and hydrogen combustion chemistry and flame behavior at engine-relevant conditions. This unique data set provides critical high-pressure, high-temperature flame speed measurements that are essential for improving chemical kinetic mechanisms and CFD simulations. Such advances are necessary to support the development of next-generation engines and power systems capable of efficiently utilizing reformed ammonia as a viable carbon-free fuel.

7.2 Diesel Ignition Conclusions

Complementing the flame speed analysis, experimental testing of diesel dual-fuel ignition within a decomposed ammonia mixture was studied. Experiments were conducted using the RCM at conditions representative of a John Deere PowerTech engine (20 bar, 880 K, and ϕ=0.5) using a 150 μm nozzle for injection. By sweeping decomposition percentage (0%, 20% and 40%), along-

side a pure hydrogen comparison case, this work establishes a unique dataset for ignition delay time (IDT) and flame morphology of diesel droplets in decomposed ammonia blends.

Results revealed a dependency on the availability of hydrogen and oxygen within the premixed fuel mixture. While larger droplet sizes consistently lead to increased ignition delay time, similar to past diesel ignition projects inside of the RCM, the impact of ammonia decomposition is and the availability of oxygen and hydrogen affected the IDT. It was seen that hydrogen decreased IDT from diffusion and its minimum ignition energy, yet this was affected by less oxygen seen at 20% decomposition. This suggests that the ignition chemistry is governed by a balance between the hydrogen and its MIE and the oxygen available to being the reaction process. In addition, diffusion and IDT modeling of the vapor film were conducted using Cantera to evaluate this.

High-speed schlieren imaging presented different flame morphologies based upon the different decomposed ammonia mixtures. Initial flame kernels for all case were smooth and spherical, dominated by a Lewis number higher than unity, because of the vaporized diesel. As the flame front propagated outward into the premixed fuel, in high decomposition mixtures, the flame quickly transition to a lower Lewis number, generating cellular instabilities at the flame front. With increased decomposition and hydrogen, the flame followed a more spherical flame morphology, whereas at low decomposition, the flame followed the direction of where the droplet traveled, creating a non-spherical morphology.

These findings and dataset provide a critical benchmark for the validation of ammonia/hydrogen/diesel kinetic mechanisms. Future work can be completed using the CFD, evaluating the predictability of current CFD strategies to model dual-fuel combustion in the RCM and the John Deere engine. These findings are important for the transition of dual-fuel engines towards ammonia-based fuels by understanding the ignition and flame propagation characteristics in this engine environment.

7.3 Future Work

7.3.1 Fractal Analysis

A primary source of uncertainty in this study is the affect that laser-induced lobes and thermodiffusive instabilities have on the measured flame speed, especially at high pressures and hydrogen-rich mixtures. This is possible by quantifying the flame wrinkling and how it deviates from the ideal spherical flame. While the comparison between the "model" and normal" RCM flames in Section 5.1.5 suggests that the flame remains consistent no matter the laser-induced lobes, work is needed to quantity this phenomenon and wrinkling at the flame front.

To complete this, future work should focus on characterizing the flame front using fractal analysis, specifically fractal dimensions and Fourier analysis. By breaking the flame front into a grid, the characteristics scales of cellular wrinkling can be determined. This framework will follow work from Chen et al. [92], who used schlieren imaging to quantify and analyze the wrinkling of flame fronts with the introduction of hydrogen. This framework can be seen in Figure 7.1.

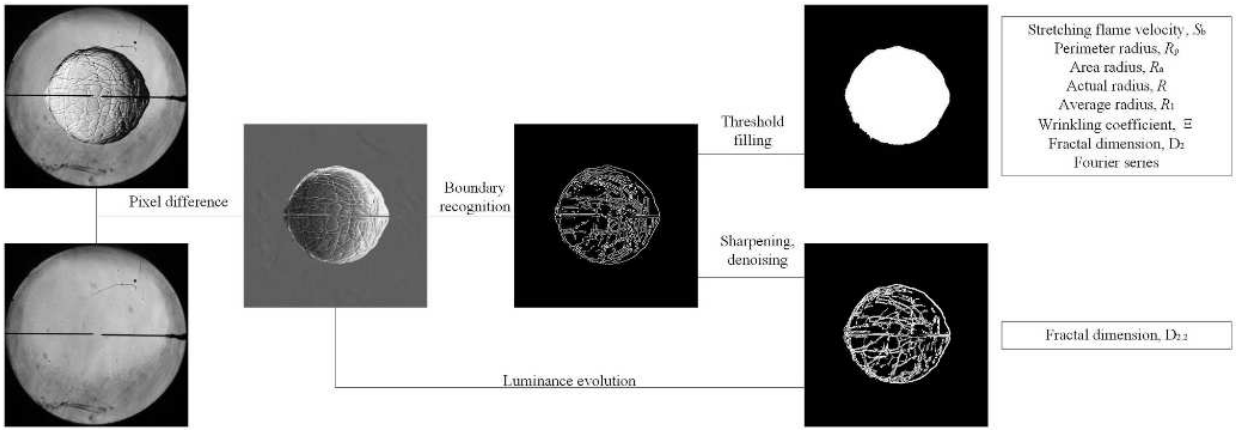

Figure 7.1: Fractal analysis and the image processing associated with flame feature extraction using MATLAB used by Chen et al. [92].

By designing a similar image-processing code to this for the current RCM will allow for the quantification of wrinkling ratios and fractal dimensions, addressing uncertainties in the flame

front, and creating relations for heavily wrinkled flames to calculate "true" laminar flames. This will also be more conducive to numerical modeling and tuning of chemical kinetic mechanisms.

7.3.2 Turbulent Flame Speed Characterization

While laminar flame speeds are necessary for chemical kinetic validation, these types of flames are not realistic and do not occur in combustion applications. In combustion engines, turbulence is one of the main drivers for the combustion process by generating flow, mixing, and dictating heat release and energy conversion. By characterizing turbulent flames, fundamental kinetic research and practical engine application can be bridged, allowing for flame speed measurements of different fuels under engine-relevant conditions.

Existing turbulent flame speed studies are primarily conducted using a constant volume combustion chamber and rely on electric motors with fans to induce turbulence into the chamber at atmospheric and near-atmospheric conditions [93–95]. However, characterization of these flames has not been conducted at engine-relevant conditions under a well-defined environment.

The dual-piston RCM is the perfect experimental device to bridge this gap in literature. With the most recent RCM chamber designed by Miguel Valles Castro [57], two opposing turbulent slot inserts can be used to generate a controlled flow. Initial tests with a 42.5% decomposed ammonia mixture have provided confirmation that this is possible, as shown in Figure 7.2 using laser ignition.

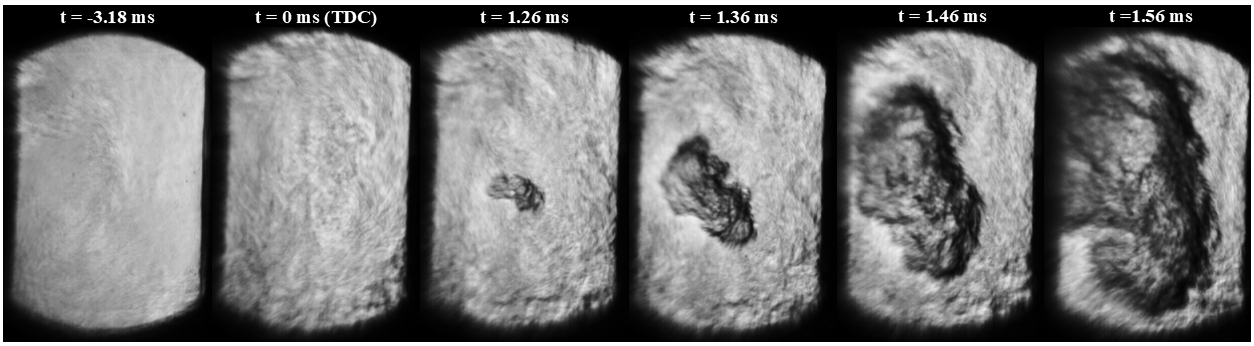

Figure 7.2: Example of a 42.5% decomposition turbulent flame in the RCM at 25 bar, 750 K using turbulent inserts.

Measuring turbulent flame speeds requires an approach to quantify both the burning velocity and the turbulent intensity (u') within the flame. There are two ways to do this in the RCM. The first of these is using particle-image-velocimetry (PIV) where a non-intrusive laser and laser sheet is used to illuminate tracer particles to measure the instantaneous velocity fields in the fluid flow. By seeding the mixture with tracer particles, the particle movement can be captured over short periods of time to compute the flow velocity. While this method is the most used and accurate, the integration of PIV into the RCM setup requires a new laser and new optical layout, where spatial challenges regarding optical access hinder this option. The second and more viable alternative is using the existing high-speed schlieren setup and the density gradients in the flame front to quantify this flow instead. As demonstrated by Wang et al [96] and Verso and Liberzon [97] have both designed methods to extract the instantaneous velocity measurements solely from the density gradients in high-speed schlieren imaging. This method would utilize the already existing optical setup.

The design and measurement of turbulent flame speeds in the RCM will allow validation and benchmark for CFD and current chemical kinetic mechanisms. By comparing the experimentally measured turbulent flame speeds against 3-D CFD simulations a broader understanding of turbulent flames in a well-defined and controlled environment will give insight onto the kinetics involved in engines.

BIBLIOGRAPHY

[1] IPCC . Global Warming of 1.5 ºC.

[2] United Nations. 1.5°C: what it means and why it matters.

[3] Department of Energy . Hydrogen Storage, 2015.

[4] Hydrogen Factsheet | Center for Sustainable Systems.

[5] US DOE . Physical Hydrogen Storage.

[6] Ola Osman, Sgouris Sgouridis, and Andrei Sleptchenko. Scaling the production of renewable ammonia: A techno-economic optimization applied in regions with high insolation. *Journal of Cleaner Production*, 271:121627, October 2020.

[7] Thorne and Derrick International . MIE Minimum Ignition Energy. *Heating and Process*.

[8] Bowen Mei, Jianguo Zhang, Xiaoxiang Shi, Zhongya Xi, and Yuyang Li. Enhancement of ammonia combustion with partial fuel cracking strategy: Laminar flame propagation and kinetic modeling investigation of NH3/H2/N2/air mixtures up to 10 atm. *Combustion and Flame*, 231:111472, September 2021.

[9] Jundie Chen, Xue Jiang, Xiaokang Qin, and Zuohua Huang. Effect of hydrogen blending on the high temperature auto-ignition of ammonia at elevated pressure. *Fuel*, 287:119563, March 2021.

[10] Muhammad Asif, Syeda Sidra Bibi, Sheraz Ahmed, Muhammad Irshad, Muhammad Shakir Hussain, Hassan Zeb, Muhammad Kashif Khan, and Jaehoon Kim. Recent advances in green hydrogen production, storage and commercial-scale use via catalytic ammonia cracking. *Chemical Engineering Journal*, 473:145381, October 2023.

[11] Galia Faingold, Rany Kabour, Si Shen, and Joseph K. Lefkowitz. Reforming of ammonia and ammonia-air mixtures in a homogenous plasma reactor: Parametric study of hydrogen yields. *International Journal of Hydrogen Energy*, 73:856–867, July 2024.

[12] Jinhoon Choe, Wenting Sun, Timothy Ombrello, and Campbell Carter. Plasma assisted ammonia combustion: Simultaneous NOx reduction and flame enhancement. *Combustion and Flame*, 228:430–432, June 2021.

[13] Dhruba J. Deka, Bhanupriya Boruah, Garam Lee, and Kenneth G. Rappé. Recent Advances in Ammonia Decomposition Technologies for Hydrogen Production. *Energy & Fuels*, 39(23):10802–10852, June 2025.

[14] Daanish S Tyrewala, Brian C Kaul, and Scott J Curran. Dual-Fuel Ammonia Equivalence Ratio Sweep Data.

[15] Daanish S Tyrewala, Brian C Kaul, Scott J Curran, and Derek A Splitter. Experimental Investigation of Air-Fuel Equivalence Ratio Effects on Advanced Dual-Fuel Ammonia/Diesel Combustion on a Single-Cylinder Medium-Duty Diesel Engine at High Load.

[16] Kislay Kishore, Caneon Kurien, and Mayank Mittal. Experimental and numerical analysis of engine characteristics of an ammonia-substituted dual-fuel CRDI diesel engine. *Fuel*, 366:131354, June 2024.

[17] Lucian Miron, Vlad-Alexandru Ungureanu, Radu Ionescu, and Radu Chiriac. An Assessment of Diesel Engine Performance Using a Dual-Fuel Diesel—Ammonia Injection. *Engineering Proceedings*, 121(1):10, 2026.

[18] Hongmei Li, Wenzheng Zhang, Yong Qian, Yuchen Hu, Yan Peng, Dehao Ju, Gang Liang, and Xingcai Lu. Combustion and emission characteristics of an ammonia diesel dual-fuel medium-speed marine engine under high-load conditions. *Fuel*, 406:137042, February 2026.

[19] Extensive testing of Wärtsilä's 4-stroke ammonia engine demonstrates GHG emission reductions by up to 90 percent.

[20] Experience Wärtsilä 25 Ammonia, 4-stroke engine for marine applications.

[21] Miguel Figueroa-Labastida, Lingzhi Zheng, Jesse W. Streicher, and Ronald K. Hanson. Ammonia/hydrogen laminar flame speed measurements at elevated temperatures. *International Journal of Hydrogen Energy*, 63:1137–1146, April 2024.

[22] Miguel Figueroa-Labastida, Lingzhi Zheng, Alison M. Ferris, Nicolas Obrecht, Cyrille Callu, and Ronald K. Hanson. Shock-tube laminar flame speed measurements of ammonia/airgon mixtures at temperatures up to 771K. *Combustion and Flame*, 260:113256, February 2024.

[23] Ryuhei Kanoshima, Akihiro Hayakawa, Takahiro Kudo, Ekenechukwu C. Okafor, Sophie Colson, Akinori Ichikawa, Taku Kudo, and Hideaki Kobayashi. Effects of initial mixture temperature and pressure on laminar burning velocity and Markstein length of ammonia/air premixed laminar flames. *Fuel*, 310:122149, February 2022.

[24] Ridong Zhang, Qihang Zhang, Yunliang Qi, Bin Yang, and Zhi Wang. Investigation on flame propagation and end-gas auto-ignition of ammonia/hydrogen in a full-field-visualized rapid compression machine. *Proceedings of the Combustion Institute*, 40(1):105455, January 2024.

[25] Adrian Nolte, Micha Renè Noé, and Karl Alexander Heufer. Laminar Burning Velocities at Engine-Relevant Conditions of Methane, Hydrogen, and Ammonia: A Rapid Compression Machine Study. *Energy & Fuels*, 38(16):15622–15629, August 2024.

[26] Shawnam, Pragya Berwal, Muskaan Singh, and Sudarshan Kumar. Laminar burning velocity measurements of NH3/H2+Air mixtures at elevated temperatures. *International Journal of Hydrogen Energy*, 71:143–154, June 2024.

[27] Xu Chen, Qingming Liu, Wenbin Zhao, Runzhi Li, Qi Zhang, and Zonglei Mou. Experimental and chemical kinetic study on the flame propagation characteristics of ammonia/hydrogen/air mixtures. *Fuel*, 334:126509, February 2023.

[28] Gabriel J. Gotama, Akihiro Hayakawa, Ekenechukwu C. Okafor, Ryuhei Kanoshima, Masao Hayashi, Taku Kudo, and Hideaki Kobayashi. Measurement of the laminar burning velocity

and kinetics study of the importance of the hydrogen recovery mechanism of ammonia/hydrogen/air premixed flames. *Combustion and Flame*, 236:111753, February 2022.

[29] Xinlu Han, Zhihua Wang, Yong He, Yanqun Zhu, and Kefa Cen. Experimental and kinetic modeling study of laminar burning velocities of NH3/syngas/air premixed flames. *Combustion and Flame*, 213:1–13, March 2020.

[30] Xinlu Han, Zhihua Wang, Yong He, Yanqun Zhu, Riyi Lin, and Alexander A. Konnov. Uniqueness and similarity in flame propagation of pre-dissociated NH3 + air and NH3 + H2 + air mixtures: An experimental and modelling study. *Fuel*, 327:125159, November 2022.

[31] Akihiro Hayakawa, Takashi Goto, Rentaro Mimoto, Yoshiyuki Arakawa, Taku Kudo, and Hideaki Kobayashi. Laminar burning velocity and Markstein length of ammonia/air premixed flames at various pressures. *Fuel*, 159:98–106, November 2015.

[32] Akinori Ichikawa, Akihiro Hayakawa, Yuichi Kitagawa, K. D. Kunkuma Amila Somarathne, Taku Kudo, and Hideaki Kobayashi. Laminar burning velocity and Markstein length of ammonia/hydrogen/air premixed flames at elevated pressures. *International Journal of Hydrogen Energy*, 40(30):9570–9578, August 2015.

[33] Bao-zhi Jin, Yong-Feng Deng, Guo-xiu Li, and Hong-meng Li. Experimental and numerical study of the laminar burning velocity of NH3/H2/air premixed flames at elevated pressure and temperature. *International Journal of Hydrogen Energy*, 47(85):36046–36057, October 2022.

[34] J. H. Lee, S. I. Lee, and O. C. Kwon. Effects of ammonia substitution on hydrogen/air flame propagation and emissions. *International Journal of Hydrogen Energy*, 35(20):11332–11341, October 2010.

[35] Charles Lhuillier, Pierre Brequigny, Nathalie Lamoureux, Francesco Contino, and Christine Mounaïm-Rousselle. Experimental investigation on laminar burning velocities of ammonia/hydrogen/air mixtures at elevated temperatures. *Fuel*, 263:116653, March 2020.

[36] Bo Liang, Wei Gao, Kai Zhang, and Yanchao Li. Ammonia-air combustion and explosion characteristics at elevated temperature and elevated pressure. *International Journal of Hydrogen Energy*, 48(53):20225–20237, June 2023.

[37] Pengcheng Ma, Haoxin Deng, Xiaoping Wen, Jun Song, Fahui Wang, and Guoyan Chen. Studies on properties of laminar premixed oxygen-enriched NH3/H2/O2/N2 flames at elevated temperature and pressure. *Journal of the Energy Institute*, 114:101645, June 2024.

[38] Bowen Mei, Siyuan Ma, Yan Zhang, Xiaoyuan Zhang, Wei Li, and Yuyang Li. Exploration on laminar flame propagation of ammonia and syngas mixtures up to 10 atm. *Combustion and Flame*, 220:368–377, October 2020.

[39] Shixing Wang, Zhihua Wang, Ayman M. Elbaz, Xinlu Han, Yong He, Mário Costa, Alexander A. Konnov, and William L. Roberts. Experimental study and kinetic analysis of the laminar burning velocity of NH3/syngas/air, NH3/CO/air and NH3/H2/air premixed flames at elevated pressures. *Combustion and Flame*, 221:270–287, November 2020.

[40] Zhaoting Wu, Jingwen Lv, Xiaoyun Liu, Wenzhu Wu, Shengquan Zhou, Beibei Yan, and Guanyi Chen. Adiabatic laminar burning velocities and NO generation paths of NH3/H2 premixed flames. *Journal of the Energy Institute*, 108:101225, June 2023.

[41] Ahmed Yasiry, Jinhua Wang, Longkai Zhang, Hongchao Dai, Ahmed A. A. Abdulraheem, Haroun A. K. Shahad, and Zuohua Huang. Experimental Study on the Effect of Hydrogen Addition on the Laminar Burning Velocity of Methane/Ammonia–Air Flames. *Applied Sciences*, 13(10):5853, January 2023.

[42] Ahmed Yasiry, Jinhua Wang, Longkai Zhang, Ahmed A. A. Abdulraheem, Xiao Cai, and Zuohua Huang. An experimental study on H2/NH3/CH4-air laminar propagating spherical

flames at elevated pressure and oxygen enrichment. *International Journal of Hydrogen Energy*, 58:28–39, March 2024.

[43] Geyuan Yin, Chaojun Wang, Meng Zhou, Yajie Zhou, Erjiang Hu, and Zuohua Huang. Experimental and kinetic study on laminar flame speeds of ammonia/syngas/air at a high temperature and elevated pressure. *Frontiers in Energy*, 16(2):263–276, April 2022.

[44] Shangkun Zhou, Wenjun Yang, Houzhang Tan, Qiwei An, Jinhua Wang, Hongchao Dai, Xiaoxiao Wang, Xuebin Wang, and Shuanghui Deng. Experimental and kinetic modeling study on NH3/syngas/air and NH3/bio-syngas/air premixed laminar flames at elevated temperature. *Combustion and Flame*, 233:111594, November 2021.

[45] Shangkun Zhou, Baochong Cui, Wenjun Yang, Houzhang Tan, Jinhua Wang, Hongchao Dai, Liangyu Li, Zia ur Rahman, Xiaoxiao Wang, Shuanghui Deng, and Xuebin Wang. An experimental and kinetic modeling study on NH3/air, NH3/H2/air, NH3/CO/air, and NH3/CH4/air premixed laminar flames at elevated temperature. *Combustion and Flame*, 248:112536, February 2023.

[46] S. Zitouni, P. Brequigny, and C. Mounam-Rousselle. Influence of hydrogen and methane addition in laminar ammonia premixed flame on burning velocity, Lewis number and Markstein length. *Combustion and Flame*, 253:112786, July 2023.

[47] Shuangshuang Zuo, Guoyan Chen, Anchao Zhang, Haoxin Deng, Xiaoping Wen, and Fahui Wang. Effect of diluent N2 addition on NH3/H2/air combustion characteristics. *Fuel*, 352:129106, November 2023.

[48] Seif Zitouni, Roman Glaznev, Heinz Pitsch, Joachim Beeckmann, Pierre Bréquigny, Christine Mounaïm-Rousselle, and Fabien Halter. Accounting for buoyancy and ignition influence in the experimental measurement of laminar flame speeds and Markstein lengths from spherical ammonia/air flames. *Proceedings of the Combustion Institute*, 41:105891, January 2025.

[49] Mohammadrasool Morovatiyan, Martia Shahsavan, Jonathan Aguilar, Mammadbaghir Baghirzade, and J. Hunter Mack. An Assessment of Hydrogen Addition to Methane Combustion with Argon as a Working Fluid in a Constant Volume Combustion Chamber. *Combustion Science and Technology*, 194(12):2395–2413, September 2022. _eprint: https://doi.org/10.1080/00102202.2020.1870454.

[50] Ekenechukwu Chijioke Okafor, Yuji Naito, Sophie Colson, Akinori Ichikawa, Taku Kudo, Akihiro Hayakawa, and Hideaki Kobayashi. Measurement and modelling of the laminar burning velocity of methane-ammonia-air flames at high pressures using a reduced reaction mechanism. *Combustion and Flame*, 204:162–175, June 2019.

[51] Xiaoyuan Zhang, Shamjad P. Moosakutty, Rajitha P. Rajan, Mourad Younes, and S. Mani Sarathy. Combustion chemistry of ammonia/hydrogen mixtures: Jet-stirred reactor measurements and comprehensive kinetic modeling. *Combustion and Flame*, 234:111653, December 2021.

[52] Chih-Jen Sung and Henry J. Curran. Using rapid compression machines for chemical kinetics studies. *Progress in Energy and Combustion Science*, 44:1–18, October 2014.

[53] S. Scott Goldsborough, Simone Hochgreb, Guillaume Vanhove, Margaret S. Wooldridge, Henry J. Curran, and Chih-Jen Sung. Advances in rapid compression machine studies of low- and intermediate-temperature autoignition phenomena. *Progress in Energy and Combustion Science*, 63:1–78, November 2017.

[54] Rubber Chemical Compatibility Charts for Nitrile, EPDM, Buna, NPR and Silicone.

[55] Ammonia Solution, Ammonia, Anhydrous | NIOSH | CDC, March 2024.

[56] Andrew Boissiere, Anthony Marchese, Azer Yalin, and Alan Van Orden. Effect of additives on laser ignition and compression ignition of methane and hydrocarbons in a rapid compression machine. 2016.

[57] Miguel Angel Valles Castro, Bret C. Windom, Daniel B. Olsen, Ciprian Dumitrache, and Jeremy Daily. Characterization of hydrogen combustion in internal combustion engines with low NOx emissions. 2026.

[58] Ciprian Dumitrache, Marc Baumgardner, Andrew Boissiere, Amir Maria, John Roucis, Anthony J. Marchese, and Azer Yalin. A study of laser induced ignition of methane–air mixtures inside a Rapid Compression Machine. *Proceedings of the Combustion Institute*, 36(3):3431–3439, 2017.

[59] Tran X. Phuoc. An experimental and numerical study of laser-induced spark in air. *Optics and Lasers in Engineering*, 43(2):113–129, February 2005.

[60] Andrew Zdanowicz. END-GAS AUTOIGNITION PROPENSITY AND FLAME PROPAGATION RATE MEASUREMENTS IN LASER-IGNITED RAPID COMPRESSION MACHINE EXPERIMENTS.

[61] Siddhesh Bharat Bhoite. IGNITION AND COMBUSTION OF LIQUID HYDROCARBON DROPLETS IN PREMIXED FUEL/AIR MIXTURES AT ELEVATED PRESSURES AND TEMPERATURES.

[62] Siddhesh Bhoite, Bret Windom, Jaswinder Singh, David Montgomery, and Anthony J. Marchese. A study of ignition and combustion of liquid hydrocarbon droplets in premixed fuel/air mixtures in a rapid compression machine. *Proceedings of the Combustion Institute*, 39(2):2533–2542, January 2023.

[63] Chris Morley. Gaseq.

[64] Yuxiang Zhu, Henry J. Curran, Sanket Girhe, Yuki Murakami, Heinz Pitsch, Kelly Senecal, Lijun Yang, and Chong-Wen Zhou. The combustion chemistry of ammonia and ammonia/hydrogen mixtures: A comprehensive chemical kinetic modeling study. *Combustion and Flame*, 260:113239, February 2024.

[65] Shijun Dong, Scott W. Wagnon, Luna Pratali Maffei, Goutham Kukkadapu, Andrea Nobili, Qian Mao, Matteo Pelucchi, Liming Cai, Kuiwen Zhang, Mandhapati Raju, Tanusree Chatterjee, William J. Pitz, Tiziano Faravelli, Heinz Pitsch, Peter Kelly Senecal, and Henry J. Curran. A new detailed kinetic model for surrogate fuels: C3MechV3.3. *Applications in Energy and Combustion Science*, 9:100043, March 2022.

[66] Andrew P. Kelley, John K. Bechtold, and Chung K. Law. Premixed flame propagation in a confining vessel with weak pressure rise. *Journal of Fluid Mechanics*, 691:26–51, January 2012.

[67] David G Goodwin, Harry K Moffat, Ingmar Schoegl, Raymond L Speth, and Bryan W Weber. Cantera: An Object-oriented Software Toolkit for Chemical Kinetics, Thermodynamics, and Transport Processes, December 2024.

[68] Caroline A. Schneider, Wayne S. Rasband, and Kevin W. Eliceiri. NIH Image to ImageJ: 25 years of image analysis. *Nature Methods*, 9(7):671–675, July 2012.

[69] Bonnie J. McBride, Michael J. Zehe, and Sanford Gordon. NASA Glenn Coefficients for Calculating Thermodynamic Properties of Individual Species. *NASA*, September 2002.

[70] R. Addabbo, J. K. Bechtold, and M. Matalon. Wrinkling of spherically expanding flames. *Proceedings of the Combustion Institute*, 29(2):1527–1535, January 2002.

[71] Antonio Attili, Rachele Lamioni, Lukas Berger, Konstantin Kleinheinz, Pasquale E. Lapenna, Heinz Pitsch, and Francesco Creta. The effect of pressure on the hydrodynamic stability limit of premixed flames. *Proceedings of the Combustion Institute*, 38(2):1973–1981, January 2021.

[72] Yousef M. Almarzooq, Matthew Hay, Maryam Khan-Ghauri, Olivier Mathieu, Waruna D. Kulatilaka, and Eric L. Petersen. The Effect of Mixture Variation and Initial Temperature on the NH2* Thickness of Spherically Propagating Laminar Ammonia Flames. *Journal of Engineering for Gas Turbines and Power*, 146(121006), August 2024.

[73] Stephen R. Turns and Daniel C. Haworth. *An Introduction to Combustion Concepts and Applications*. McGraw Hill, 4 edition, 2021.

[74] S. Girhe, A. Snackers, T. Lehmann, R. Langer, F. Loffredo, R. Glaznev, J. Beeckmann, and H. Pitsch. Ammonia and ammonia/hydrogen combustion: Comprehensive quantitative assessment of kinetic models and examination of critical parameters. *Combustion and Flame*, 267:113560, September 2024.

[75] András György Szanthoffer, Máté Papp, Tibor Nagy, and Tamás Turányi. Assessing the performance of recent detailed NH3 and NH3/H2 combustion mechanisms. *Combustion and Flame*, 287:114878, May 2026.

[76] Xiaoyuan Zhang, Kiran K. Yalamanchi, and S. Mani Sarathy. Combustion chemistry of ammonia/C1 fuels: A comprehensive kinetic modeling study. *Fuel*, 341:127676, June 2023.

[77] Paul Marshall and Peter Glarborg. Probing High-Temperature Amine Chemistry: Is the Reaction NH3 + NH2 N2H3 + H2 Important? *The Journal of Physical Chemistry A*, 127(11):2601–2607, March 2023.

[78] András Gy. Szanthoffer, Máté Papp, and Tamás Turányi. Identification of well-parameterised reaction steps in detailed combustion mechanisms – A case study of ammonia/air flames. *Fuel*, 380:132938, January 2025.

[79] Xinlu Han, Zhihua Wang, Bo Zhou, Yong He, Yanqun Zhu, and Kefa Cen. Effect of H2 and O2 enrichment on the laminar burning velocities of NH3+H2+N2+O2 flames: Experimental and kinetic study. *Applications in Energy and Combustion Science*, 15:100160, September 2023.

[80] Alessandro Stagni and Carlo Cavallotti. H-abstractions by O2, NO2, NH2, and HO2 from H2NO: Theoretical study and implications for ammonia low-temperature kinetics. *Proceedings of the Combustion Institute*, 39(1):633–641, January 2023.

[81] Shuang Xu, Gesheng Li, Mengni Zhou, Weiping Yu, Zunhua Zhang, Di Hou, and Fulin Yu. Experimental and kinetic studies of extinction limits of counterflow cool and hot diffusion flames of ammonia/*n*-dodecane. *Combustion and Flame*, 245:112316, November 2022.

[82] Siddhesh Bhoite. A COMPUTATIONAL STUDY OF AUTOIGNITION, SPARK IGNITION AND DUAL FUEL DROPLET IGNITION IN A RAPID COMPRESSION MACHINE.

[83] K Richards, P Senecal, and E Pomraning. CONVERGE 4*, Convergent Science, Madison, WI (2025).

[84] Ansys EnSight, 2025.

[85] Ciprian Dumitrache, Rachel VanOsdol, Christopher M. Limbach, and Azer P. Yalin. Control of Early Flame Kernel Growth by Multi-Wavelength Laser Pulses for Enhanced Ignition. *Scientific Reports*, 7(1):10239, August 2017.

[86] O. C. Kwon, G. Rozenchan, and C. K. Law. Cellular instabilities and self-acceleration of outwardly propagating spherical flames. *Proceedings of the Combustion Institute*, 29(2):1775–1783, January 2002.

[87] Moshe Matalon. The Darrieus–Landau instability of premixed flames. *Fluid Dynamics Research*, 50(5):051412, August 2018.

[88] D. Bradley, M. Lawes, Kexin Liu, S. Verhelst, and R. Woolley. Laminar burning velocities of lean hydrogen–air mixtures at pressures up to 1.0 MPa. *Combustion and Flame*, 149(1):162–172, April 2007.

[89] Jialong Huo, Abhishek Saha, Zhuyin Ren, and Chung K. Law. Self-acceleration and global pulsation in hydrodynamically unstable expanding laminar flames. *Combustion and Flame*, 194:419–425, August 2018.

[90] Martin Rieth, Andrea Gruber, and Jacqueline H. Chen. The effect of pressure on lean premixed hydrogen-air flames. *Combustion and Flame*, 250:112514, April 2023.

[91] R. J. Kee, F. M. Rupley, J. A. Miller, M. E. Coltrin, J. F. Grcar, E. Meeks, H. K. Moffar, A. E. Lutz, M. D. Smooke Dixon-Lewis, J. Warnatz, G. H. Evans, R. S. Larson, R. E. Mitchell, L. R. Petzold, W. C. Reynolds, M. Caracotsios, W. E. Stewart, P. Glarborg, C. Wang, and O. Adigun. CHEMKIN.

[92] Jiao Chen, Haoxin Deng, and Jun Zhao. Quantifying intrinsic flame instabilities of methane-equivalent ammonia/hydrogen/LPG blends using fractal dimension and fourier analysis. *International Journal of Hydrogen Energy*, 225:154551, April 2026.

[93] Swetaprovo Chaudhuri, Fujia Wu, Delin Zhu, and Chung K. Law. Flame Speed and Self-Similar Propagation of Expanding Turbulent Premixed Flames. *Physical Review Letters*, 108(4):044503, January 2012.

[94] P. Brequigny, F. Halter, and C. Mounaïm-Rousselle. Lewis number and Markstein length effects on turbulent expanding flames in a spherical vessel. *Experimental Thermal and Fluid Science*, 73:33–41, May 2016.

[95] Jian-Bin Cao, Nan-Nan Zhao, Guo-Xiu Li, Hong-Meng Li, Guo-Peng Zhang, and Jun Yang. Turbulent burning velocity of NH3/H2/air mixtures spherical flames: Effects of differential diffusion and turbulent stretch. *International Journal of Hydrogen Energy*, 59:525–534, March 2024.

[96] Q. Wang, Y. Wu, H. T. Cheng, X. H. Mei, and C. Y. Zhao. A schlieren motion estimation method for seedless velocimetry measurement. *Experimental Thermal and Fluid Science*, 109:109880, December 2019.

[97] Lilly Verso and Alex Liberzon. Background Oriented Schlieren in a Density Stratified Fluid. *Review of Scientific Instruments*, 86(10):103705, October 2015. arXiv:1506.08889 [physics.flu-dyn].

APPENDIX A – RCM OVERHAUL INSTRUCTION

A.1 Good Practice

- Group and bag bolts based off of which side and where they come from. Make sure to label.
- Have cheater bars ready as some hydraulic lines and tight bolts.
- Utilize pusher bolts to remove parts of the RCM.
- When reassembling be careful with precision fits, everything on the RCM basically contains a precision fit.
  - Use hydraulic oil to help lubricate to make reassembly a little easier.
- Corner off two areas of the lab, labeling them based off of what side of the RCM part are coming from. Make sure to lay parts on towels and do not lay sealing surfaces on the ground.
- Be careful not to scratch anything, a lot of these parts are machined surfaces. They are also very heavy and awkward to move and will hit the main frame of the RCM, make sure you have two people when taking big parts out.

A.2 Tools Required

1. Wrenches: 9/16”, 7/8”, 1-1/16”, 1-1/8”, 1-1/4”
   - May need some extra for smaller things
2. Adjustable Wrench
3. Hex Keys: 3/32”, 3/16”, 1/4”, 5/16”, 3/8”, 1/2”
4. Sockets: 15/16”
5. Torque Wrench
6. 2 Belt Wrench’s
7. 2 Ratchet Straps
8. Hydraulic Fluid Parts
   (a) 5 gallon bucket
   (b) Roasting pan
   (c) Large funnel
9. Mallet

A.3 Disassembly Procedure

This section will be done for both sides. Before beginning this make sure the gas manifold, schlieren, and tables are removed from the area around the RCM. Before removing the schlieren setup and moving the table make sure to make where the table is sitting and where the schlieren is with respect to the table and the RCM, this will help with putting the setup back together to what it originally was.

The left and right sides of the RCM are identical however, it is best to keep everything separate and re-assembled as they were originally. Everything will be described as if one side is being done, make sure to do each step to each side of the RCM within the same step.

1. Using the 1/4” hex key, remove the 8 bolts that hold the cooling collar (14) in place.

2. Remove the cooling collar, utilizing the pusher bolts located next to the bolt. Keep the plastic fluid bottle attached.

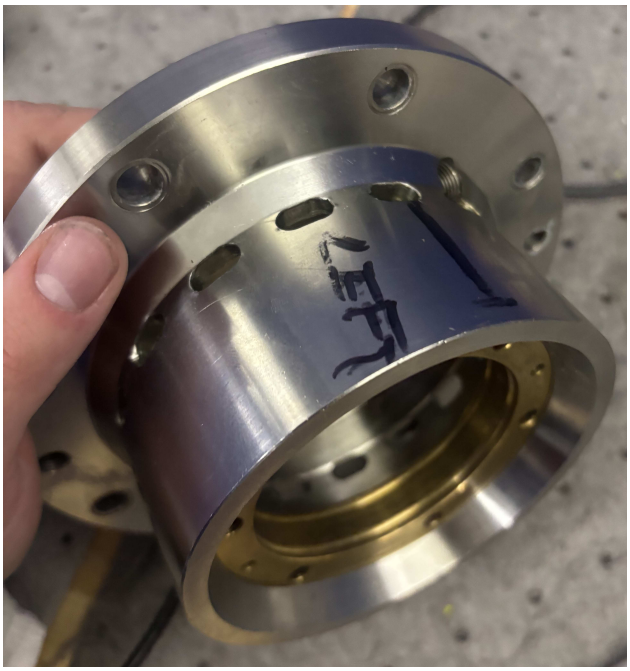

3. Place the roasting pan (or some type of vessel) underneath the drain port of the external oil chamber (7). Using the 1-1/16” wrench, remove the drain plug. Oil should immediately begin to drain. Allow all of the oil to drain, the black roasting pan will hold all of the oil held in the oil chamber. Dump this oil into the 5 gallon bucket.

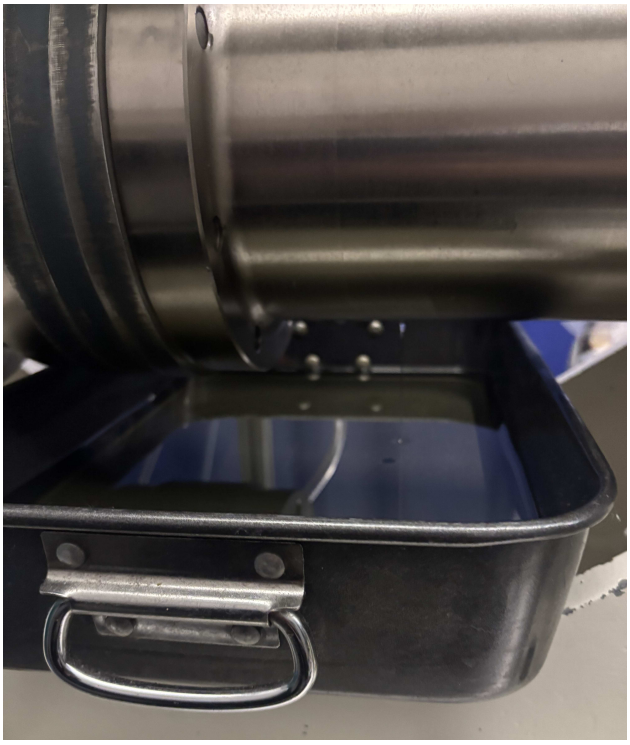

4. Once all of the oil is drained remove the pneumatic filling pipe, using the 7/8” and an adjustable wrench, that is attached to the bottom of the air chamber (4) outside of the RCM.
   (a) These nuts will be very tight, make sure to apply back pressure when turning these using an adjustable wrench on the elbow of the pipe.
   (b) This must be removed prior to removing the linear transducers as a vacuum may still be present within the air chamber, making it difficult to remove the transducers.

5. Remove the linear transducers by removing the 6 bolts with the 5/16” hex key. Use the push bolts to easily take the linear transducer out.

(a) Before removing the linear transducer, make sure to unplug the connection to the computer.

(b) When taking the linear transducers out make sure to be very careful, the metal component has some weight to it. Be careful with the magnetic rod; it should remain undamaged.

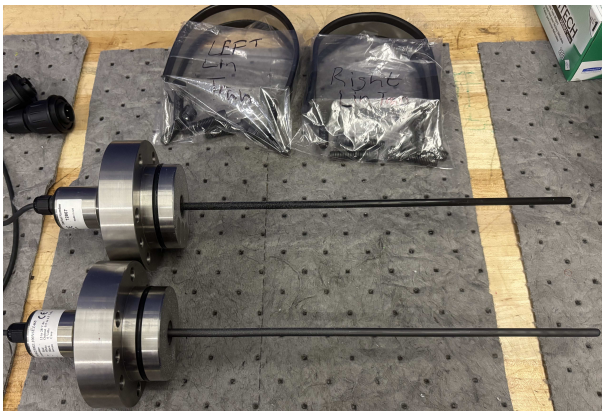

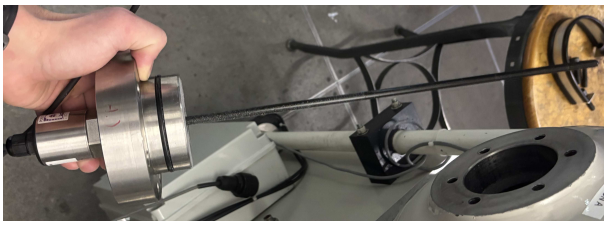

6. Using the 3/8” hex key, remove the 8 bolts surrounding the air chamber (4). Use the pusher bolts to help remove the air chamber. Be very careful removing this. It is very easy to strip the threads in the pusher bolts.

   (a) You can use a mallet to help push this out. Make sure to not hit anything else when using the mallet.

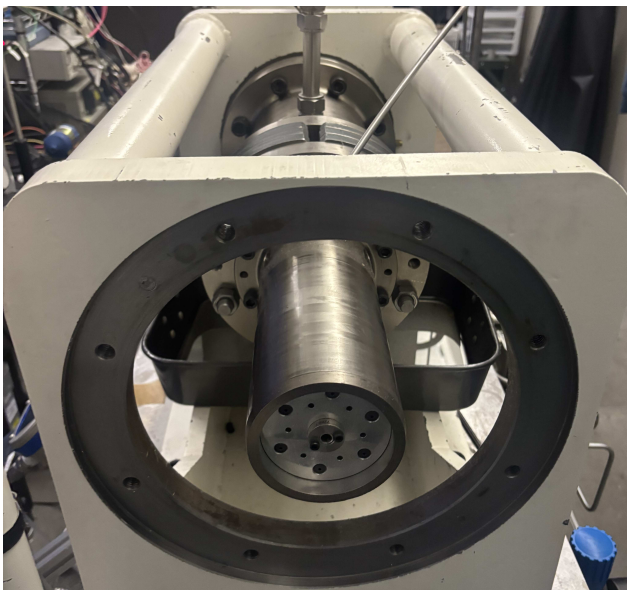

7. Once removing the air chambers, the drive cylinder and piston assembly should be exposed. To remove any remaining hydraulic in the system manually actuate the piston rods by pushing the back of the piston assembly (9) and the front multiple times.
   (a) These may be difficult to push so use the mallet and lightly tap to get the plungers to move then push.
   (b) Think of this as moving from BDC to TDC.

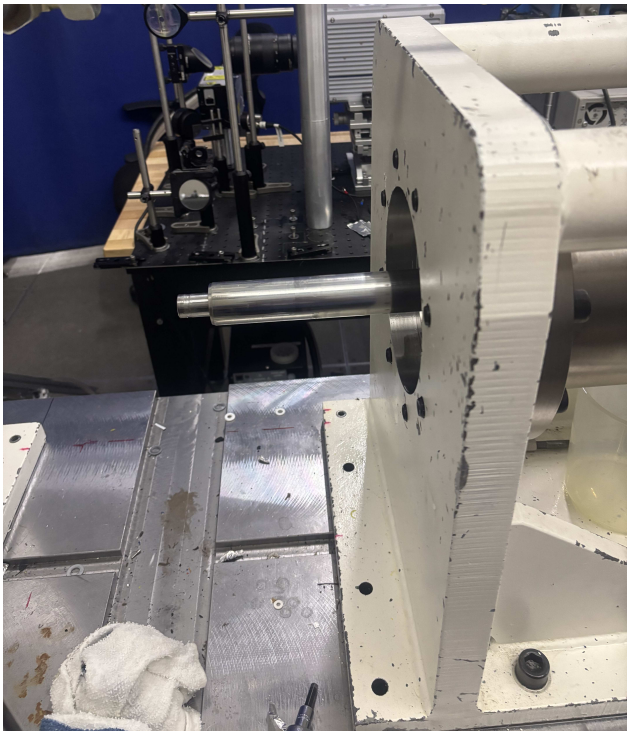

8. Push the piston assembly (9) TDC, then using the 5/16" hex key remove the 8 bolts that secure the drive cylinder (5) to the internal oil chamber (8). Remove the drive cylinder making sure to not damage the plunger (9).
   (a) When doing this make sure you are in the fully-compressed position. It will make it much easier to remove the drive cylinder.

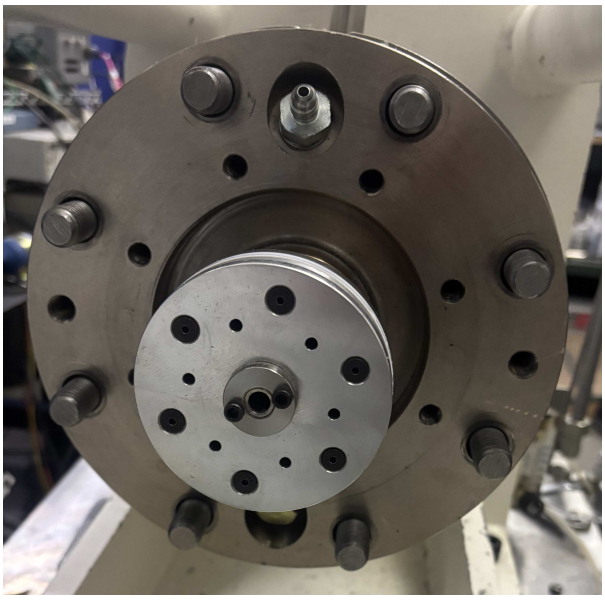

9. Using the 9/16” wrench, disconnect the secondary hydraulic line, located on the backside of the internal oil chamber.
10. Disconnect the line at the top of the plastic jug and remove the entire plastic jug with the secondary hydraulic lines still connected.
11. Using the 15/16” socket wrench, remove the 8 nuts that secure the internal oil chamber (8) to the external oil chamber (7).
12. Carefully take off the 3 compression spacers between the flanges of the oil chambers (7&8).

13. Remove the internal oil chamber (8) and drive plunger assembly (9) through the rear hole of the RCM frame.
14. Now with the internal oil chamber and drive plunger removed (8&9), the plunger can be removed from the oil chamber. The assembly is attached via threads in the center of the oil chamber. Use two strap wrenches to loosen the threads and unscrew the compression plunger (16) from the drive plunger (9).

15. Using the 1-1/4” and 1-1/8” wrench, disconnect the main hydraulic line from the external oil chamber and the T-fitting in the middle of the RCM.

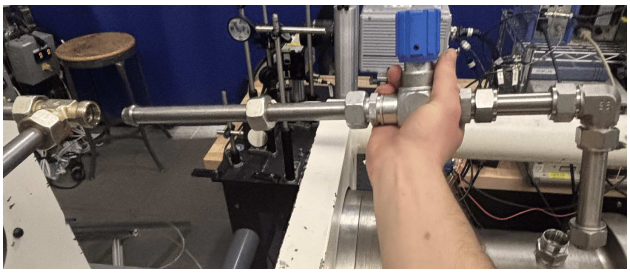

16. Using the bars on the main frame of the RCM, use two ratchet straps to cradle the external oil chamber.
17. Using the 1/2” hex key, remove the 8 bolts that attach the external oil chamber (7) and neck house sealing (6) to the main frame of the RCM.
18. Now slide the external oil chamber and neck house sealing across the frame to the back side of the main frame. Slowly pull it out of the back side of the frame.

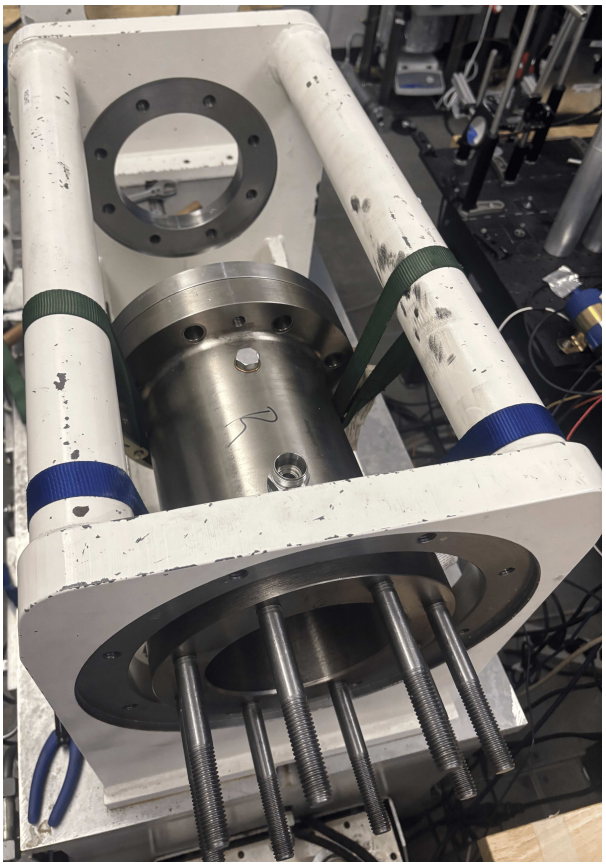

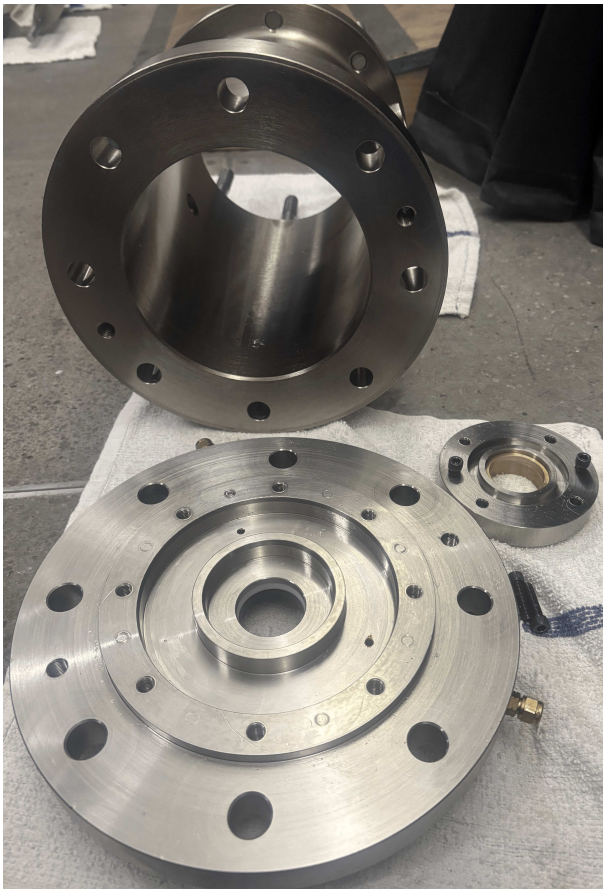

19. The neck house sealing can now be removed from the external oil chamber, where seals can be replaced.
20. Using a 3/16” hex key, remove the 4 bolts securing the neck seal retainer (17) to the neck house sealing, replacing the rear neck seal.
21. Once finished, follow the steps backwards to reassemble the RCM, do each side at the same time at every step. Good luck!